KATHOLIEKE UNIVERSITEIT
LEUVEN

FACULTEIT WETENSCHAPPEN
Departement Natuurkunde en Sterrenkunde
Instituut voor Kern- en Stralingsfysica

Spin, magnetic moment and charge radius of ^{51}K

door

Hanne HEYLEN

Promotor: prof. dr. G. Neyens
Begeleidster: J. Papuga

Proefschrift ingediend tot het
behalen van de graad van
Master in de Fysica

Academiejaar 2011-2012

Dankwoord

Nu de laatste woorden van deze master thesis zijn neergepend, is het de hoogste tijd om enkele mensen te bedanken.

Om te beginnen wil ik graag mijn promotor prof. Gerda Neyens bedanken. Bedankt voor het boeiende jaar waarin ik steeds bij u terecht kon voor kleine en grotere vragen. De open en enthousiaste manier van werken heeft er zeker toe bijgedragen dat het een aangenaam jaar is geworden.

I would like to thank Jasna, for helping me through the (little) problems I've encountered on a daily basis and for generally creating a nice atmosphere in the office. Although I would have preferred a warmer office, I think I was lucky with the "roommate" I've got. Mustafa, also you deserve a word of gratitude. In between your ten-thousand other things to do, you made the time for helping me when needed.
I also want to thank all the people who were present at the experiment, thanks for finding the time to answer my questions and for making it an interesting experience, especially Mark and Kim.

Zoals beloofd, vermeld ik (met veel plezier) Lieve in dit dankwoordje. De keuze van kop in plaats van munt (of was het omgekeerd?), heeft waarschijnlijk een grotere invloed gehad op hoe dit jaar eruit heeft gezien, dan enige andere factor.
Ook Wally verdient een pluim, om mijn thesis te doorploeteren en zo mee te helpen aan het eindresultaat dat nu voor u ligt.

Tenslotte wil ik de mensen bedanken waarbij ik thuis kon komen na een lange thesisdag/week. Mama en papa, bedankt voor de steun en de vrijheid die jullie mij altijd gegeven hebben.
Akke, Lot, Tinne en Toon, bedankt om altijd klaar te staan voor een babbel, een liedje/dansje, een "kuip" wijn of gewoon een gezellige avond.
En niet te vergeten, bedankt Christophe, je betekent meer voor mij dan je je kan inbeelden.

Samenvatting

Veel van wat vandaag geweten is over de structuur van kernen, is afkomstig van de 340 stabiele of langlevende isotopen die hier op aarde voorkomen. De eigenschappen van kernen met een ongewone proton-tot-neutron verhouding zijn echter veel minder goed gekend. Aangezien deze kernen vaak fascinerende kenmerken hebben en ze een belangrijke rol spelen in de kernreacties in het heelal, is een aanzienlijk deel van het hedendaags kernfysisch onderzoek gericht op deze zogenoemde exotische kernen. In deze master thesis worden de zeer neutronrijke kaliumisotopen ($Z = 19$) bestudeerd en in het bijzonder de eigenschappen van de grondtoestand van ^{51}K. Omdat kalium slechts 1 proton minder heeft dan het magische calcium, zijn de exotische kaliumisotopen zeer geschikt om de evolutie van de kernstructuur rond de $Z = 20$ schillensluiting te onderzoeken.

De kernspins, magnetische momenten en ladingstralen van de neutronrijke kaliumisotopen zijn bestudeerd via collineaire laser spectroscopie. Deze hoge-precisie techniek maakt gebruik van laser geïnduceerde overgangen tussen atomaire hyperfijn niveau's om de nucleaire eigenschappen te onderzoeken. De hyperfijn spectra van de radioactieve kaliumisotopen zijn opgemeten in twee experimenten aan de COLLAPS bundellijn gesitueerd in ISOLDE, CERN. Voor deze experimenten is een nieuw foton-detectie systeem ontwikkeld met als resultaat een verhoging van de detectie-efficiëntie met een factor tien.
In het eerste experiment uitgevoerd in 2010, konden naast de reeds bekende hyperfijn spectra van ^{38,39,42,44,46,47}K ook de ongekende spectra van $^{48-50}$K succesvol worden opgemeten. Een onzuiverheid in de ionenbundel op massa 51 verhinderde echter de meting van ^{51}K. De plaatsing van een bijkomende filter in de detectiezone kon dit probleem verhelpen zodat in 2011 voor het eerst de meting van het hyperfijn spectrum van ^{51}K kon worden gerealiseerd. Het zijn de experimentele data verkregen in dit laatste experiment die werden geanalyseerd in deze master thesis. Naast de magnetische momenten en ladingstralen van ^{39,42,47}K, was het voor de eerste keer ook mogelijk deze eigenschappen voor ^{51}K te bepalen.

Kalium heeft 19 protonen waardoor de eigenschappen van de K-isotopen met een even neutron getal worden bepaald door een gat in de proton (π) *sd*-schil. Van deze isotopen is geweten dat het energie-verschil tussen de grondtoestand met spin $I = 3/2$ en de geëxciteerde toestand met spin $I = 1/2$ afneemt wanneer het neutron (ν) $1f_{7/2}$ orbitaal gevuld wordt met neutronen ($20 < N \leq 28$). Gezien deze toestanden respectievelijk overeenkomen met een proton gat in $\pi d_{3/2}$ en proton gat in $\pi s_{1/2}$, kan de afname verklaard worden door een verschuiving van de één-deeltjes energieën van deze orbitalen. In ^{47}K ($N = 28$) leidt dit zelfs tot een inversie van de spin van de grondtoestand.
De verandering van de één-deeltjes energieën in functie van proton/neutron getal wordt algemeen waargenomen in regio's ver van β-stabiliteit en zorgt voor een evolutie van de schillenstructuur. Dit leidt tot interessante fenomenen zoals o.a. het verschijnen en verdwijnen van de standaard magische getallen. Voor een beter begrip van dit verschijnsel is het belangrijk een uitgebreide experimentele kennis te hebben van de kerneigenschappen over een uitgestrekt gebied van de kernkaart.

Tot op heden was er weinig bekend over de kaliumisotopen met meer dan 28 neutronen en het was dan ook de vraag of de inversie van de grondtoestand ook hier voortduurt. De neutronrijke kaliumisotopen zijn reeds in enkele experimenten onderzocht, maar tot nu toe konden nog geen definitieve spins worden toegewezen. Bovendien was er ook op theoretisch vlak nog veel onduidelijkheid. De situatie tot en met $N = 32$ is opgehelderd door onze recente experimenten. In 2010 was het mogelijk om de spin van grondtoestand van ^{49}K te bepalen als $I = 1/2$, overeenkomstig met een blijvende inversie van de spin. In deze thesis is dan aangetoond dat ^{51}K een gewone grondtoestand met spin $I = 3/2$ heeft. Voorts is het aan de hand van de magnetisch momenten ook mogelijk om de configuratie van de protonen en neutronen in hun schillen te onderzoeken. Hiervoor is het experimenteel gemeten magnetisch moment vergeleken met de waarde berekend in het schillenmodel met een SDPF-U interactie. De golffunctie die de grondtoestand van ^{49}K beschrijft, wordt niet zuiver bepaald door een gat in $\pi s_{1/2}$ maar er is sprake van een gemengde toestand. Anderzijds is de grondtoestand van ^{51}K ($\mu = 0.488(33)\mu_N$) zuiver met een golffunctie gedomineerd door een proton-gat in $\pi d_{3/2}$.

Een andere boeiende karakteristiek van de calcium regio is het verschijnen van een nieuw magisch neutron getal op $N = 32$. Met de observatie van een verhoogde $E(2_1^+)$ waarde en een reductie van de $B(E2)$ overgangswaarschijnlijkheid in ^{52}Ca$_{32}$ ($Z = 20$), ^{54}Ti$_{32}$ ($Z = 22$) en ^{56}Cr$_{32}$ ($Z = 20$), is deze nieuwe schillensluiting op $N = 32$ duidelijk experimenteel vastgesteld. Voorlopig zijn er echter nog geen gegevens omtrent het magisch karakter van $N = 32$ voor isotopen met minder dan 20 protonen. In de gemiddelde kwadratische ladingstralen over een keten van isotopen is een schillensluiting duidelijk zichtbaar. De ladingstralen vertonen een afvlakking of kleine vermindering net voor, en een sterke toename net na een magisch neutron getal. De gemiddelde kwadratische ladingstralen kunnen worden afgeleid van de isotopenverschuiving. Dus door deze isotopenverschuiving te meten voor de kaliumisotopen van $N = 19$ tot en met $N = 32$ is het mogelijk om de mogelijke schillensluiting op $N = 32$ te onderzoeken voor kernen met een onvolledige πsd-schil ($Z < 20$). Het opgemeten verschil in ladingstraal ($\delta\langle r^2\rangle^{47,51} = 0.60(19)$ fm^2) op $N = 32$ is echter niet nauwkeurig genoeg om af te leiden of er ook voor kalium een aanwijzing is voor een schillensluiting.

Om de onzekerheden op het gemeten magnetisch moment en verschil in ladingstraal van ^{51}K aanzienlijk te verkleinen is deze zomer een nieuwe kalium-experiment gepland in ISOLDE. In 2011 heeft o.a. het delen van de protonen bundel met enkele andere experimenten, geleid tot slecht geresolveerde hyperfijn spectra voor ^{51}K. Zonder dit proton-delen en met langere meettijden, zijn spectra met een betere kwaliteit een haalbare kaart.

Aan de hand van collineaire laser spectroscopie was het mogelijk om voor het eerst het hyperfijn spectrum van ^{51}K op te meten. De spin, het magnetisch moment en de gemiddelde kwadratische ladingstraal konden worden bepaald, maar de precisie van de verkregen resultaten is nog laag. Deze eigenschappen zijn zeer geschikt om de kernstructuur te onderzoeken en zijn gebruikt om de evolutie van de één-deeltjes energieën in het calcium gebied te onderzoeken.

Contents

Dankwoord i

Samenvatting ii

Table of Contents v

I Introduction 1

II Motivation and physics case 4

1 Changing shell structure in exotic nuclei 5

2 The neutron-rich potassium isotopes 7

3 The magic character of $N = 32$ 9

III Nuclear ground-state properties and hyperfine structure 11

1 The nuclear mean square charge radius and isotope shift 11

1.1 Isotope shift 12

2 Nuclear moments 14

2.1 Magnetic dipole moment 14

2.2 Electric quadrupole moment 16

3 Hyperfine structure and coupling constants 17

3.1 The magnetic dipole interaction 18

3.2 The electric quadrupole interaction 19

4 Collinear laser spectroscopy 20

IV The experiment 23

1 Collinear laser spectroscopy at ISOLDE 24

1.1 The ISOLDE facility . . . 24
1.2 The COLLAPS beamline . . . 25
1.3 The ISCOOL acceleration voltage . . . 26
1.4 The light detection system . . . 27
2 Data collection . . . 27
3 Analysis . . . 28
3.1 Fitting procedure . . . 28
3.2 Weighted mean and errors . . . 30
3.3 Selection of hyperfine spectra . . . 30
3.4 ISCOOL correction voltage . . . 32
3.5 The influence of fixing fit parameters . . . 33
3.6 Asymmetric line profile in ^{50}K spectra . . . 37
3.7 Analysis of the spectra of ^{51}K . . . 38

V Results and discussion **47**
1 The hyperfine coupling constants and magnetic moments . . . 47
2 The isotope shifts and changes in charge radii . . . 49
3 Magnetic moments in the shell model framework . . . 50
3.1 The magnetic moment of ^{49}K . . . 52
3.2 The magnetic moment of ^{51}K . . . 54
4 Mean square charge radii and magic numbers . . . 54

VI Conclusion **58**

Appendix A Hyperfine spectra **61**

Appendix B *A*-parameters **64**

Appendix C The mixed ground-state of ^{49}K **66**

Bibliography **68**

Chapter I

Introduction

Around 340 isotopes occur naturally on earth, 255 stable isotopes and another 85 radioactive ones. It is however predicted that more than 6000 different types of nuclei are particle-bound (shown in fig. I.1) and can be found in astrophysical processes throughout the universe. Although about 2500 of them can be produced in present-day experimental facilities, for only ∼500 nuclei the basis properties such as mass or shape are studied so far. Especially the nuclei far from stability, the so-called exotic nuclei, are poorly known. These nuclei exhibit a wide variety of fascinating properties and are the subject of much of the nuclear physics research currently performed.
In this master thesis the ground-state properties of the neutron-rich potassium ($Z = 19$) isotopes are studied. In particular, the spin, magnetic moment and mean square charge radius of ^{51}K are investigated.

The nucleus is a complex system which consists of protons and neutrons bound together by the strong interaction. Its description as a quantum mechanical many-body problem cannot be solved exactly but several nuclear models exist, each with their own weaknesses and strengths in predicting properties along the table of nuclides. The refinement and extension of these models to regions far from stability goes hand-in-hand with the progress in experimental physics. Comparison between the measured properties and the theoretical calculations allows a test of the predictive power of the models and provides clues for potential improvements. For a better understanding of the nuclear structure, it is therefore indispensable to measure a wide range of properties over a large region of the chart of nuclides. For example, the nuclear moments and charge radii are excellent observables because they give direct information on the configuration and binding of the nucleons.
During the first experimental studies of the nuclear structure in the 1930-40's, nuclei with a specific number of nucleons ($N, Z = 2, 8, 20, 28, 50, 82, 126$) were observed to be exceptionally stable. These "magic" nucleon numbers remained unexplained until 1949, when Maria Goeppert-Mayer and Hans Jenssen proposed the nuclear shell model. This Nobel prize-winning model was a triumph for nuclear structure research. In the simple model, each nucleon moves in a mean potential generated by all other nucleons. This results in single-particle orbits arranged into shells and large energy gaps between the shells give rise to the observed magic numbers. Nuclei in the vicinity of magic proton and neutron numbers can then be described by an inert core of closed shells combined with a few interacting valence nucleons. This introduces a huge

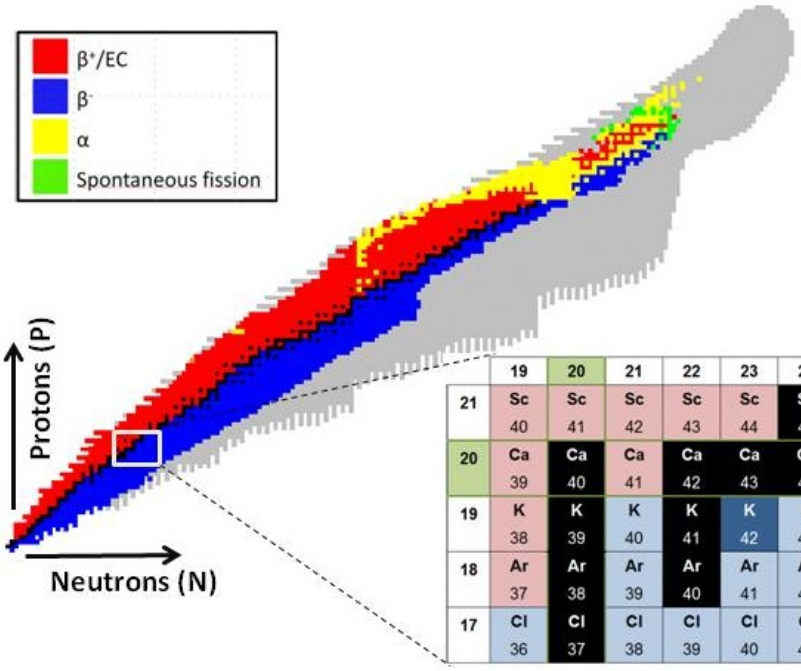

	19	20	21	22	23	24	25	26	27	28	29	30	31	32	33	34
21	Sc 40	Sc 41	Sc 42	Sc 43	Sc 44	Sc 45	Sc 46	Sc 47	Sc 48	Sc 49	Sc 50	Sc 51	Sc 52	Sc 53	Sc 54	Sc 55
20	Ca 39	Ca 40	Ca 41	Ca 42	Ca 43	Ca 44	Ca 45	Ca 46	Ca 47	Ca 48	Ca 49	Ca 50	Ca 51	Ca 52	Ca 53	Ca 54
19	K 38	K 39	K 40	K 41	K 42	K 43	K 44	K 45	K 46	K 47	K 48	K 49	K 50	K 51	K 52	K 53
18	Ar 37	Ar 38	Ar 39	Ar 40	Ar 41	Ar 42	Ar 43	Ar 44	Ar 45	Ar 46	Ar 47	Ar 48	Ar 49	Ar 50	Ar 51	Ar 52
17	Cl 36	Cl 37	Cl 38	Cl 39	Cl 40	Cl 41	Cl 42	Cl 43	Cl 44	Cl 45	Cl 46	Cl 47	Cl 48	Cl 49	Cl 50	Cl 51

FIG. I.1: The chart of nuclides. Each square represents one isotope, colored according to the dominant decay mode. The stable isotopes are shown in black. The grey area indicates the isotopes which are predicted to exist but which cannot be produced experimentally at present. The potassium region is enlarged in the right part of the figure. The magic proton and neutron numbers are marked by a green box. The neutron-rich K-isotopes studied in the experimental campaign are shown in a slightly darker shade.

simplification and enables a successful prediction of several empirical observed features of the nucleus.

For decades, the exploration of the nuclear structure was limited to nuclei near the valley of stability and it was assumed that the magic numbers were valid over the entire nuclear chart. In the last 30 years however, the study of exotic nuclei has revealed that classic shell gaps disappear while new magic numbers appear in regions far from stability. This modification of the shell gaps as a function of proton and neutron numbers has attracted much attention both theoretically and experimentally and is still being investigated today.
The potassium isotopes ($Z = 19$) with one proton less than the magic calcium isotopes, offer a nice testing ground to study this evolution of shell structure during the filling of the neutron shells. It has been observed that the energy splitting between the $3/2^+$ ground-state and the $1/2^+$ excited state decreases with an increasing number of neutrons, eventually resulting in an inversion of the ground-state spin at $N = 28$. This behavior is explained by a change in shell structure due to the attractive proton-neutron interaction. With little experimental data beyond $N = 28$, it is unclear how the nuclear structure evolves when more neutrons are added. Furthermore, experimental evidence for $Z > 20$ suggests the appearance of a new magic number at $N = 32$. For $Z < 20$ barely anything is known about the magic behavior of this subshell.
The lack of empirical information on the potassium isotopes with more than 28 neutrons triggered an experimental campaign at ISOLDE, CERN in 2010. In the experiment, the magnetic moments and charge radii of ^{48,49,50}K (N = 29-31) could successfully be determined via collinear

laser spectroscopy. This technique enables high-resolution measurements of the nuclear observables using optical transitions between the atomic levels. However, laser spectroscopy on ^{51}K ($N = 32$) was hindered by a beam contamination at mass 51. Therefore, the measurement was repeated in 2011 with an improved experimental set-up. The results obtained in the 2011 run are the subject of this master thesis.

Outline

In the first chapter, the reader is introduced to the general framework of this thesis. In chapter two, it is illustrated why it is interesting to measure the ground-state properties of the neutron-rich potassium isotopes. The physics case of the K-isotopes is presented and the experimental evidence on the $N = 32$ magic number is discussed. In the third chapter, magnetic moments and mean square charge radii are introduced as a tool to study the structure of the nucleus. In the same chapter, it is described how these observables can be measured via high-resolution laser spectroscopy. The focus in chapter four is on the analysis of the data obtained in the potassium experiment of 2011. This entails a description of the experimental set-up at ISOLDE, the fitting procedure and a detailed explanation on how useful information is extracted from the raw data. In the last chapter, an overview of the final results is given and it is discussed what can be learned about the physics case presented in the motivation of this work. As a conclusion, the work is summarized and an outlook for the future is provided.

Chapter II

Motivation and physics case

The potassium region in the nuclear chart is shown in fig. I.1. The K-isotopes have one proton less than the magic $Z = 20$ calcium nuclei, leaving a hole in the proton (π) sd shell. With neutron numbers ranging from $N = 20$ to $N = 32$, the potassium isotopes are studied in the vicinity of two magic numbers, at $N = 20$ and at $N = 28$. Furthermore, the magic character of the $N = 32$ subshell gap is still an active research topic. The configuration of the protons and neutrons can be seen in fig. II.1. The valence neutrons in between ^{40}K and ^{47}K are placed in the $\nu 1f_{7/2}$ level, whereas for $N > 28$ the $\nu 2p_{3/2}$ level is gradually filled. The exact energy

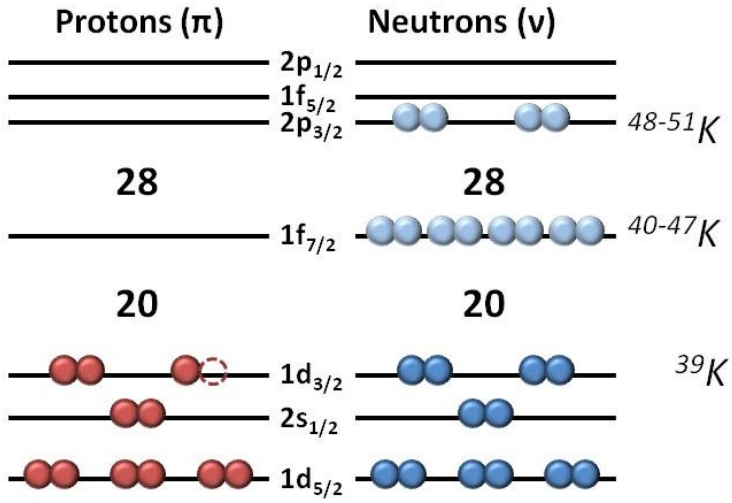

FIG. II.1: The configuration of the proton and neutron shells for the neutron-rich K isotopes. With increasing neutron number, the $\nu 1f_{7/2}$ and $\nu 2p_{3/2}$ neutron levels are subsequently filled. The order of the proton $\pi 2s_{1/2}$ and $\pi 1d_{3/2}$ orbitals is inverted for ^{47}K ($N = 28$), resulting in a hole in the $\pi 2s_{1/2}$ proton-orbit instead of a hole in the $\pi 1d_{3/2}$ orbit.

difference between the orbits in fig. II.1 depends on the interaction between the protons and the neutrons and changes as a function of the number of neutrons. This modification of the single-particle energies might even result in an inversion of the proton $2s_{1/2}$ and $1d_{3/2}$ orbits for $N = 28$, considering that in ^{47}K the ground state spin is found to be $I = 1/2$ [27]. Then the question arises which mechanism is responsible for this evolving shell structure. This is

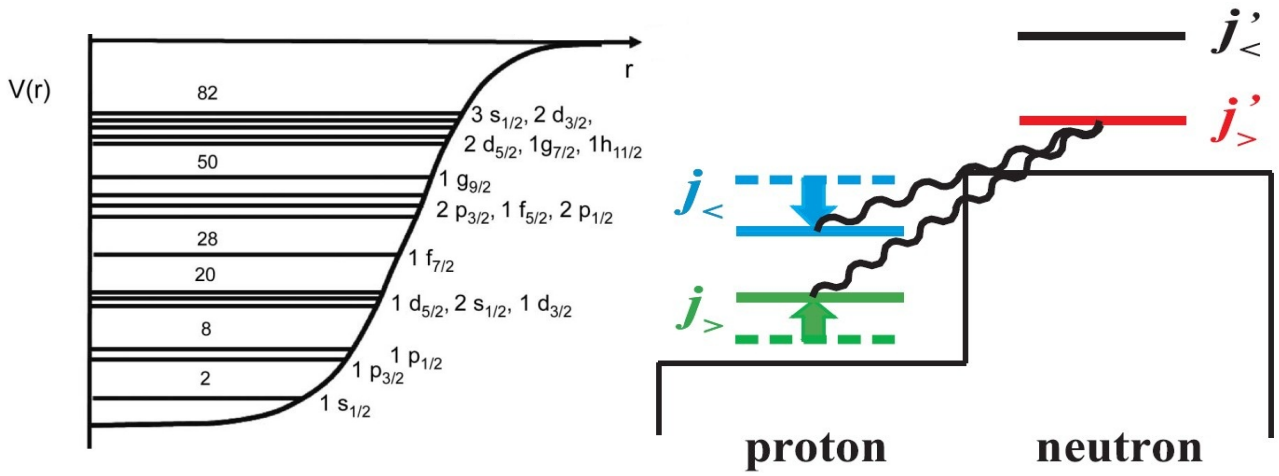

(a) (b)

FIG. II.2: (a) The nuclear mean field depicted by a Woods-Saxon potential. The typical shell structure due to the grouping of the single-particle orbits is shown. The figure is taken from [9]. (b) Schematic illustration of the tensor part of the monopole interaction. Taken from [11].

discussed in the next section. Afterwards, an overview is given of what is already known on the neutron-rich potassium isotopes. The last part is focussed on the experimental data which exists for the magicity of the $N = 32$ shell closure. The entire discussion clarifies why the exotic potassium isotopes are worth investigating.

1 Changing shell structure in exotic nuclei

The evolution of the shell structure for nuclei far from stability is clearly established with notable examples such as the appearance of the $N = 16$ magic number in the O isotopes [1], the island of inversion in the Mg region [2–4] and the weakening of the $N = 28$ shell closure [5–7]. The reason why the effective single-particle orbits are modified keeps attracting a lot of theoretical and experimental interest to this day. Following section provides only a short introduction to this interesting matter, a more extensive discussion can for be found in e.g. the review paper of Sorlin and Porquet [8].

The atomic nucleus consists of protons and neutrons which interact with each other via the strong force. There exist many theoretical models which try to explain this complex system, of which the nuclear shell model is one of the most successful ones. The concept underlying this formalism, is that nucleons move independently in a central potential generated by all other nucleons. The single-particle motion in this potential can be solved, resulting in energy eigenstates which are called single-particle orbits. These orbits are characterized by the radial quantum number n, the orbital momentum l and the total angular momentum j. The eigenstates are grouped in shells with large energy gaps between them, giving rise to the familiar shell structure shown in fig. II.2a.
This simple picture is already adequate in describing many nuclear properties, especially for

nuclei with one particle or hole outside a closed core[1]. The structure in nuclei further from shell closures however, is affected by interactions between nucleons outside closed shells and by interactions between the core and valence nucleons (core polarization). To account for the former effect, the naive model has to be extended with a residual interaction between the valence nucleons. This interaction is an effective one since the bare nucleon-nucleon interaction is altered in the presence of the nuclear medium. Due to the residual interaction, the single-particle energies (SPE) are modified resulting in effective single-particle energies (ESPE).

The effective interaction between two nucleons j and j' depends generally on several properties such as the radial overlap, the orbital angular momentum, the relative spin orientation and isospin (π-π, ν-ν or π-ν). It can be expanded in monopole, quadrupole and higher order multipole terms. The monopole part then corresponds to the average energy as a result of adding two interacting nucleons to the nucleus [8]. It is the main component which has to be considered in the study of the changing single-particle orbits.
Similar as for the bare nucleon-nucleon interaction, the monopole term can be decomposed in a central, spin-orbit and tensor part. The tensor component depends on the spin and the isospin operators. The isospin operator favors charge exchange processes which leads to a stronger interaction between protons and neutrons than between like nucleons. Analogously does the spin operator couple the spin-orbit partners $j_> = l + 1/2$ and $j_< = l - 1/2$ more strongly than $j_<$-$j_<$ or $j_>$-$j_>$ [10]. The attractive interaction between proton-neutron spin-flip partners results in a lowering of the proton $j_<$ orbit when adding neutrons to the $j_>$ orbit and vice versa, as schematically illustrated in fig. II.2b. On the other hand, the interaction between same-spin partners is repulsive which gives rise to an increase in orbit energy. It has been shown that these effects are more pronounced for $l_j \approx l_{j'}$ and for wavefunctions which have a large radial overlap.
As discussed by Otsuka and coworkers [10–12], it is the effect of the tensor interaction on the effective single-particle energies which governs the evolution of the shell structure. As example, the proton ESPEs in the proton *sd* shell as a function of the number of neutrons in the $\nu 1f_{7/2}$ orbital is shown in fig. II.3. The energy levels clearly shift when more neutrons are added. The decrease in energy splitting between $\pi 1d_{3/2}$ and $\pi 2s_{1/2}$ is in agreement with the attractive interaction between the protons in $\pi 1d_{3/2}$ and the neutrons in $\nu 1f_{7/2}$.

To perform realistic calculations for medium-to-heavy mass systems, two different approaches exist.
In the mean field framework [13, 14] the nuclear mean potential is determined self-consistently. The model is based on effective energy functionals of which the main features are motivated from ab initio theory. Since a purely theoretical approach does not yield sufficiently accurate predictions, the actual free parameters in the model have to be determined from extensive fits to nuclear structure data.
An alternative is presented by large scale shell model calculations [15, 16]. In this approach an appropriate core of closed shells has to be chosen combined with a configuration space in which the valence nucleons can interact via an effective interaction. The effective interaction which is used has to be adapted to the chosen valence space and is usually determined (partially) phenomologically. When more detailed experimental information becomes available on the

[1] A closed core consists of completely filled shells, i.e. a magic proton and neutron number. The core is relatively inert due to the Pauli principle which inhibits scattering to already filled states. Therefore, the interaction with the valence nucleons is limited.

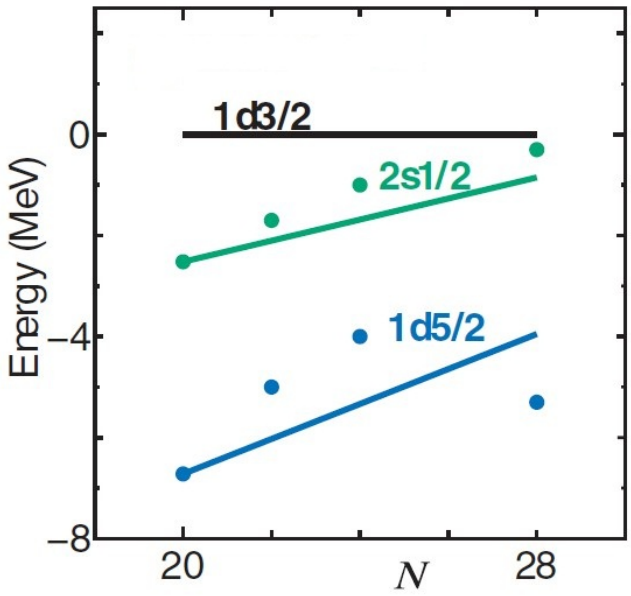

FIG. II.3: Evolution of the proton effective single-particle energies as a function of the neutron number. The ESPEs from $2s_{1/2}$ and $1d_{5/2}$ are shown relative to the $1d_{3/2}$ level. The circles represent the experimental data and the full line represents theoretical calculations performed with the SDPF-M shell model interaction. Picture taken from [11].

region of interest, the effective interaction can be improved and upgrades of the same interaction appear. For instance, the SPDF-NR [17] and SPDF-U [18] are two different upgrades of the *sp-df* [19] residual interaction which comprises the *sd* shell for the protons and the *sd* and *pf* shell for the neutrons.
It is clear that in order to make reliable predictions from theory, it is crucial to have a good and wide knowledge of the nuclear properties.

2 The neutron-rich potassium isotopes

With one hole in the proton $1d_{3/2}$ orbital, the even-neutron K-isotopes are expected to have a $3/2^+$ ground-state with a first excited $1/2^+$ state. This excited state corresponds to an excitation of a proton from the $\pi s_{1/2}$ orbital to the $\pi d_{3/2}$ orbital. It is experimentally observed that the energy difference between those $1/2^+$ and $3/2^+$ states decreases when the neutron $\nu f_{7/2}$ shell is filled, as is illustrated in fig. II.4. From more than 2.5 MeV difference for ^{39}K ($N = 20$), eventually a negative energy difference is obtained at ^{47}K ($N = 28$). This observation is based on a measured inversion of the ground-state spin using a laser spectroscopy technique [20].
One proton-pickup reactions on calcium isotopes [21,22] have shown that the ground-states of ^{39,41,43}K and the first excited ($3/2^+$) state of ^{47}K are pure $\pi d_{3/2}$ states. On the other hand, the ground-state of ^{47}K is shown to have a strong single-particle $\pi s_{1/2}$ nature. This is confirmed by the measured magnetic moments [20]. The changing spin is then described by an inversion of the proton orbitals. This inversion is related to the attractive $\pi d_{3/2}$-$\nu f_{7/2}$ proton-neutron interaction between spin-flip partners which is clearly visible in fig. II.3. The attraction causes a greater binding of the $\pi d_{3/2}$ effective single-particle level when the number of neutrons is

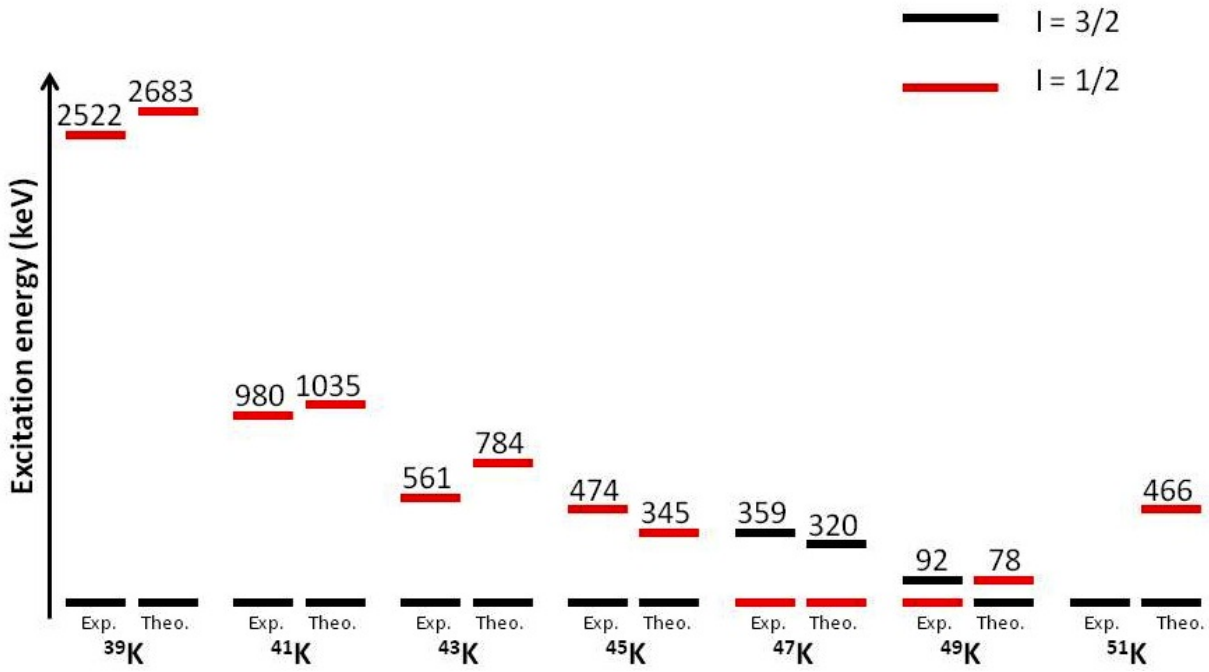

FIG. II.4: The energy levels of the $1/2^+$ and $3/2^+$ state compared to the ground-state energy. The left values are the experimental values while the right values are the values found in the shell-model calculations [17]. Up to ^{47}K, the experimental energies are taken from [23–27]. Notice the inversion of the ground-state spin at ^{47,49}K ($N = 28$ and 30). The experimental spin-assigments for ^{49}K and ^{51}K are found in the potassium experiment in 2010 [28] and in this work.

increased, resulting near-degenerate $\pi s_{1/2}$ and $\pi d_{3/2}$ levels at $N = 28$. Beyond this neutron number the neutrons are filling the $\nu p_{3/2}$ orbital and therefore the further evolution of the proton single-particle levels is determined by the relative strength of $\pi\left(d_{3/2}/s_{1/2}\right)$-$\nu p_{3/2}$ interaction. Theoretically, shell-model calculations using the SDPF-U interaction of Nowacki [17] give a very good reproduction of the experimentally found energy-splitting of the $3/2^+$ state and $1/2^+$ state for $N \leq 28$ (see fig. II.4). For $^{49}K_{30}$ and $^{51}K_{32}$ these calculations predict that the orbitals return to their normal order, leading to a $3/2^+$ ground-state spin for both isotopes. Likewise, mean-field calculations using HFB with a Skyrme interaction [29] suggest a repulsive proton-neutron interaction beyond $N = 28$ leading to the same conclusion. Until the experimental campaign on the potassium isotopes in 2010, not much experimental data was available to check these predictions.

Experimentally, ^{49}K was studied via the β-decay from potassium to calcium [30]. Based on the beta strength function of the decay, the ground-state spin and parity was tentatively assigned to be $3/2^+$. However, a more recent experiment using deep-inelastic heavy-ion reactions [31] proposed a $1/2^+$ ground-state with the first excited $3/2^+$ state at 92 keV. In the light of the disagreement, the β decay data were reconsidered leading to the conclusion that a $1/2^+$ ground-state spin assignment is equally likely as a $3/2^+$ ground-state spin [31]. A potential $I = 1/2^+$ assignment for ground-state of ^{49}K disagrees with the most recent shell-model calculations [17]. The somewhat older SPDF-NR interaction [18], on the other hand predicts a $1/2^+$ ground-state spin in agreement with the findings in the deep-inelastic heavy-ion reactions.
These contradicting results, both experimentally and theoretically, motivated a further study of

the ^{49}K ground-state spin. Because the magnetic moment gives a direct and model-independent way to determine the corresponding nuclear configuration and because the moments of a 1/2 and 3/2 state are significantly different, it was decided to probe the spin via magnetic moment measurements. Additionally, by using the collinear laser spectroscopy for this purpose, the ground-state spin can be measured directly in some cases.

In 2006, the β-decay of ^{51}K to ^{51}Ca was investigated using beta-delayed gammas and neutrons [32]. Only two levels in ^{51}Ca are fed in the beta-decay, the ground-state ($I = 3/2^-$) and an excited state at 3460 keV, preliminarily assigned to have a $7/2^-$ spin. The branching ratios and ft-values observed in the experiment then suggest a first-forbidden transitions from a $I = 3/2^+$ ground-state in ^{51}K to the ground- and excited state in calcium. A recent experiment on ^{51}Ca [33] confirmed the $7/2^-$ spin of the excited state at 3460 keV. Accordingly, the observed transition from the ground-state of potassium to this excited state excludes the possibility of a $I = 1/2^+$ ground-state in ^{51}K. Measurement of the magnetic moment can confirm or refute this proposed $3/2^+$ ground-state spin.

3 The magic character of $N = 32$

The magicity of proton and neutron numbers is manifested by discontinuities in several nuclear observables, e.g. a sudden increase in energy of the first excited 2^+ state, a raised neutron separation energy, a decrease in charge radius, an increase of the magnetic moment towards the Schmidt value and so on. The first experimental indication for a new subshell closure at $N = 32$ came from the calcium isotopes [34]. The relatively high excitation energy $E(2_1^+)$ of ^{52}Ca compared to the neighboring isotopes pointed towards increased stability. Systematic investigation of the excitation energies for titanium ($Z = 22$) [35] and chromium ($Z = 24$) [36] revealed a peaked $E(2_1^+)$ value for the $N = 32$ isotones as well. Additionally, a low $B(E2; 0^+ \rightarrow 2^+)$ transition probability for ^{54}Ti$_{32}$ [37] and ^{56}Cr$_{32}$ [38] was observed. Both a high $E(2_1^+)$ and a low $B(E2)$ are a sign of reduced quadrupole collectivity which is expected in the case of a magic number. All these observations, shown in fig. II.5, are therefore consistent with a subshell closure at $N = 32$ in neutron-rich nuclei above ^{48}Ca.

A sizable energy gap at $N = 32$ can be explained by a significant $\nu 2p_{1/2}$-$\nu 2p_{3/2}$ spin-orbit splitting combined with a reduced $\pi 1f_{7/2}$-$\nu 1f_{5/2}$ proton-neutron monopole interaction as protons are removed from the $1\pi f_{7/2}$ orbit. This orbit is completely filled in the nickel isotopes ($Z = 28$) and gets emptied when going to Ca ($Z = 20$). For a not completely filled orbit, the attractive $\pi 1f_{7/2}$-$\nu 1f_{5/2}$ interaction is reduced, resulting in a migration of the $\nu 1f_{5/2}$ state towards higher energies. Hereby the energy difference between the $\nu 1f_{5/2}$ orbit and $\nu 2p_{3/2}$ orbit is increased, causing an energy gap at $N = 32$. The migration of the $\nu 1f_{5/2}$ state is experimentally confirmed in β-decay studies of the $N = 33$ isotones in Sc, Ti and V [39].

Shell-model calculations with the GXPF1 interaction [40] optimized for the description of the pf-shell nuclei, are able to reproduce the systematics of the $N = 32$ shell closure in this region. Furthermore, these calculations also predict another subshell closure at $N = 34$ in Ca and Ti. However, no large shell gap can be inferred from the observables in Ti. This discrepancy motivated the improvement of GXPF1 to GXPF1A, of which the predictions agree better with

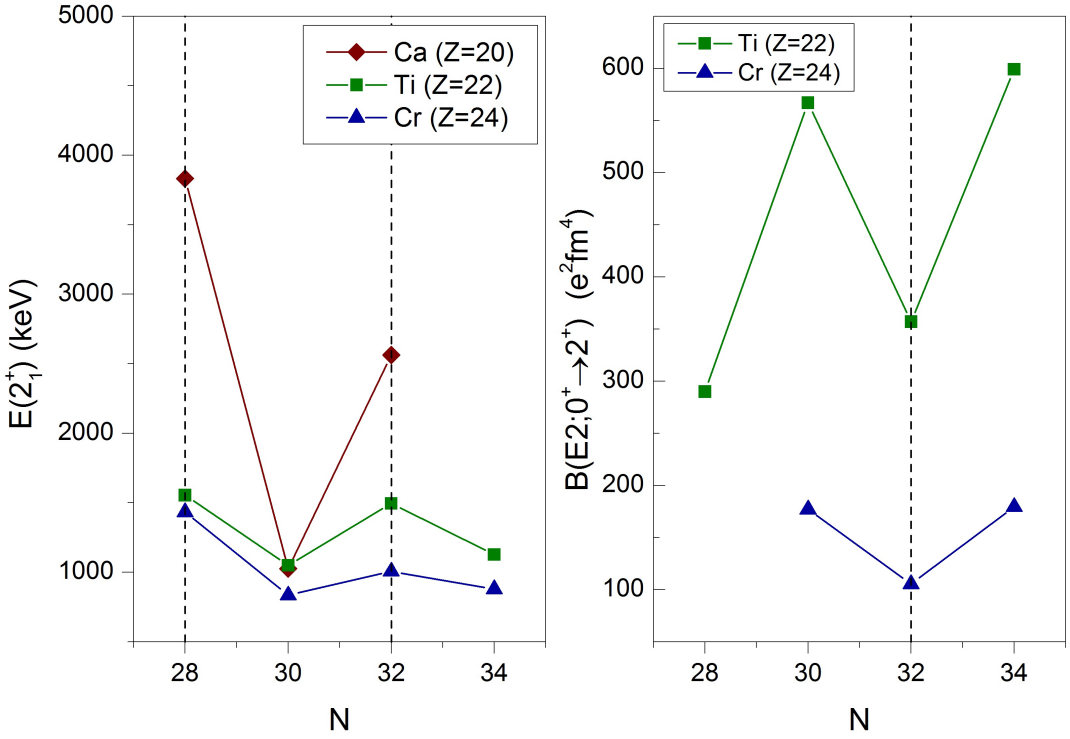

FIG. II.5: Left, the energy of the first excited 2^+ state in Ca, Ti and Cr is shown. The increased excitation energy at $N = 32$ relative to that at $N = 30$ and $N = 34$ suggests the development of a shell gap at N=32. Also the $N = 28$ magic number is clearly visible. Right, the $B(E2)$ transition probability for the neutron-rich Ti and Cr isotopes is depicted. The opposite behavior of $E(2_1^+)$ is observed: a dip at $N = 32$. This confirms the supposed magicity.

experiments [41]. Also with the improved interaction, the energy gap at $N = 34$ is believed to persist for ^{54}Ca. Because this isotope is till today experimentally out of reach, experiments are focussed on isotopes in its vicinity. In 2009, the first experimental evidence for a doubly-magic $^{54}Ca_{34}$ was found in a nucleon-transfer reaction experiment on ^{55}Ti [42]. In this experiment, a $1/2^-$ ground-state was deduced for ^{55}Ti which is in agreement with the GXPF1 calculations and hence hints to a $N = 34$ subshell.

So far, no experimental data on the $N = 32$ subshell for $Z < 20$ exist. The variation of mean square charge radius over an isotopic chain is a good observable to investigate this effect. Indeed, at a magic number a characteristic change in slope of the charge radii in function of the neutron number is observed. By the measurement of the mean square charge radii up to ^{51}K ($N = 32$), it is the goal to see whether the magicity of $N = 32$ persists in the potassium isotopes.

Chapter III

Nuclear ground-state properties and hyperfine structure

A nucleus is a complex system of protons and neutrons bound together by the strong force. The nuclear moments and mean square charge radius are important properties in the investigation of the role of this strong interaction in regions far from stability, since they provide a direct probe for the nuclear structure. In free atoms, these observables can be measured by examining the interaction of the nucleus with the electron cloud. This interaction, called the hyperfine interaction, leads to a very small splitting of the atomic energy levels, dependent on the properties of the nucleus. A precise measurement of the splitting therefore offers a way to extract the desired nuclear information. A very suitable technique to study the hyperfine splitting is collinear laser spectroscopy. By inducing optical transitions between atomic energy levels, the hyperfine spectrum of the nucleus can be probed.

The goal of this chapter is to introduce the concepts used in the following chapters of this thesis. First, the focus is on the nuclear ground-state properties and their importance as a tool in investigating the nuclear structure. Afterwards it is explained what can be learned on the nucleus by studying the atomic energy levels. The last part is then devoted to the experimental method used to measure these energy levels with a very high precision.

1 The nuclear mean square charge radius and isotope shift

The nucleus is usually depicted as a solid sphere with a volume proportional to the number of nucleons in the nucleus A, implying a radius r which is proportional to $A^{1/3}$. However, like in the atomic case, the nucleus has no sharp boundaries and one usually works with an average quantity, the mean square radius.
Many techniques such as electron scattering experiments or measurements of optical transition frequencies, rely on the electromagnetic interaction to investigate the nuclear properties. This interaction is only sensitive to the charge distribution, namely to the protons. The quantity of

interest in this case is the nuclear mean square charge radius $\langle r^2 \rangle$ which is defined by

$$\langle r^2 \rangle = \frac{\int \rho(r) r^2 dr}{\int \rho(r) dr} \tag{III.1}$$

given the charge density $\rho(r)$. The denominator is a normalization factor equal to the total charge in the nucleus eZ.

In between shell closures, the equilibrium shape of a nucleus is often not spherical but rather deformed in an oblate or a prolate shape. On the other hand, nuclei close to filled proton or neutron shells are generally strongly bound. This will be apparent in the nuclear shape which tends to be more spherical and which can be probed by measuring the nuclear mean square charge radius.
In laser spectroscopy, it is not the mean square charge radius itself but the difference in mean square charge radii $\delta\langle r^2 \rangle^{A,A'} = \langle r^2 \rangle^{A'} - \langle r^2 \rangle^{A}$ in an isotopic chain which is the accessible quantity. These changes then reveal interesting information about the nuclear interaction at work when the neutron shells get filled or emptied. The quantity needed for the determination of $\delta\langle r^2 \rangle^{A,A'}$ is the isotope shift $\delta\nu^{A,A'}$.

1.1 Isotope shift

A chemical element is characterized by the specific set of spectral lines in its spectrum. However, these spectral lines depend slightly on the isotope under consideration, resulting in a small frequency difference in the atomic transition frequency of two isotopes of the same element. This difference is called the isotope shift

$$\delta\nu^{A,A'} = \nu^{A'} - \nu^{A} \tag{III.2}$$

There are two effects which contribute to this shift in transition frequencies. The first effect, the mass shift, arises from the motion of the nucleus and the electrons around their common center of mass, which depends on the mass of the isotope. The second contribution is because of the extended charge distribution of the nucleus and is called the field shift.

The mass shift

In the center of mass frame of the atom, the total momentum is given by $\boldsymbol{p}_{\text{tot}} = \boldsymbol{p}_{\text{nuc}} + \sum_i \boldsymbol{p}_i$ where $\boldsymbol{p}_{\text{nuc}}$ is the momentum of the nucleus while $\boldsymbol{p}_i$ is the momentum of the i^{th} electron. By definition, this equation is equal to zero which implies that $\boldsymbol{p}_{\text{nuc}} = -\sum_i \boldsymbol{p}_i$. The total kinetic energy E_k is given by

$$\begin{aligned} E_k &= \frac{\boldsymbol{p}_{\text{nuc}}^2}{2M} + \sum_i \frac{\boldsymbol{p}_i^2}{2m_e} \\ &= \frac{1}{2M}\left(\sum_i \boldsymbol{p}_i^2 + \sum_{i,j} \boldsymbol{p}_i \cdot \boldsymbol{p}_j\right) + \sum_i \frac{\boldsymbol{p}_i^2}{2m_e} \\ &= \frac{1}{2}\frac{M+m_e}{Mm_e}\sum_i \boldsymbol{p}_i^2 + \frac{1}{2M}\sum_{i,j} \boldsymbol{p}_i \cdot \boldsymbol{p}_j \end{aligned} \tag{III.3}$$

The difference in the first term of this expression for two isotopes gives rise to the normal mass shift (NMS). For an infinitely massive atom, the kinetic energy is only due to the first term

$$E_k(\infty) = \frac{1}{2m_e}\sum_i \boldsymbol{p}_i^2 \tag{III.4}$$

Hence, the first term contribution E_{k1} to III.3 for a finite mass atom is given by

$$E_{k1}(M) = \frac{M + m_e}{M} E_k(\infty) \tag{III.5}$$

A quick calculation gives the energy difference between two isotopes A and A'

$$E_{k1}(M_A) - E_{k1}(M_{A'}) = \frac{(M_{A'} - M_A)m_e}{M_A M_{A'}} E_k(\infty) = \frac{(M_{A'} - M_A)m_e}{M_{A'}(M_A + m_e)} E_{k1}(M_A) \tag{III.6}$$

Usually the electron mass in the denominator is neglected and the expression is converted to frequency

$$\begin{aligned} \delta\nu_{\mathrm{NMS}}^{A,A'} &= m_e \nu_A \frac{M_{A'} - M_A}{M_{A'} M_A} \\ &= k_{\mathrm{NMS}} f(M_A, M_{A'}) \end{aligned} \tag{III.7}$$

where normal mass shift constant $k_{\mathrm{NMS}} = \nu_A m_e$ can be easily calculated when the transition frequency for the reference isotope and the electron mass are known. This factor is constant along the isotope chain.
Correlations between the momenta of the electrons are included by the second term in eq. III.3 and constitute the specific mass shift (SMS). These correlations are difficult to quantify for many-electron systems and are calculated in sophisticated calculations. It can however be shown that, similar to the normal mass shift, the specific mass shift can be written as a constant multiplied by the mass factor $f(M_A, M_{A'})$ [43]. When the contribution of both the normal and the specific mass shift is included, the total mass shift can be written as

$$\begin{aligned} \delta\nu_{\mathrm{MS}}^{A,A'} &= \delta\nu_{\mathrm{NMS}} + \delta\nu_{\mathrm{SMS}} \\ &= (k_{\mathrm{NMS}} + k_{\mathrm{SMS}}) f(M_A, M_{A'}) \end{aligned} \tag{III.8}$$

Although the mass shift is negligible in heavy mass nuclei, it will be the dominant term in light nuclei such as the potassium isotopes. In that case it is about two orders of magnitude bigger than the field shift.

The field shift

The nucleus is not a point-charge but occupies some volume in space. Electrons will be influenced by the exact size and shape of the nuclear distribution if they have a non-zero probability to be found inside the nucleus. Small changes of this nuclear shape over the isotopic chain, lead to a different spatial overlap in electronic and nuclear wave functions, an effect which is visible in the field shift.
For a certain transition, the field shift is the product of a nuclear parameter $\lambda^{A,A'}$ and an electronic parameter F_e

$$\delta\nu_{\mathrm{FS}}^{A,A'} = F_e \lambda^{A,A'} \tag{III.9}$$

The nuclear parameter can be expanded in the even radial moments of the charge distribution $\langle r^{2n}\rangle$ [44]

$$\lambda^{A,A'} = \delta\langle r^2\rangle^{A,A'} + \frac{C_2}{C_1}\delta\langle r^4\rangle^{A,A'} + \frac{C_3}{C_1}\delta\langle r^6\rangle^{A,A'} + \dots \tag{III.10}$$

For light and medium-mass elements, the higher order terms are smaller than the experimental precision and to a good approximation the nuclear parameter reduces to the first term

$$\lambda^{A,A'} \approx \delta\langle r^2\rangle^{A,A'} \tag{III.11}$$

The field shift constant F_e is the result of the change in electronic charge distribution at the nucleus for the two electronic levels of interest in the transition. Because the electronic configuration remains unchanged for one element, F_e is constant over the isotope chain and thus it can be obtained from reference measurements. In some cases it is also possible to calculate F_e directly from theory.
In light and medium-mass nuclei, the electron density probing the nuclear charge distribution is low which results in only a small field shift [45].

Finally the total isotope shift is expressed as

$$\delta\nu^{A,A'} = (k_{\mathrm{NMS}} + k_{\mathrm{SMS}})f(M_A, M_{A'}) + F\delta\langle r^2\rangle^{A,A'} \tag{III.12}$$

If all electronic factors are known, it is possible to calculate the changes in mean square nuclear charge radii $\delta\langle r^2\rangle^{AA'}$ from the measured isotope shifts. Note that because the field shift is only a small effect, a high-resolution experimental technique is required.

2 Nuclear moments

Although the strong interaction determines the distribution and the motion of the nucleons in the nucleus, a lot of nuclear information can be extracted by looking at the electromagnetic fields produced by these nucleons. As described in many electrodynamics textbooks (e.g. in [46]), each charge and current distribution can be expressed by an multipole expansion in magnetic and electric moments. The nucleus is no exception and valuable information on the nuclear structure is contained in the nuclear multipole moments.

In nuclear physics, only moments up to second order will be significant. These are the electric monopole moments, which is just the total charge eZ, the magnetic dipole moment and the electric quadrupole moment[1]. The last two will be discussed in more detail in the following section.

2.1 Magnetic dipole moment

In a classical picture, the magnetic dipole moment induced by an orbiting charged particle is proportional to the orbital angular momentum $\boldsymbol{L}$. For a particle with charge q and mass m the

[1]The electric dipole moment and magnetic quadrupole moments vanish due to parity considerations.

magnetic moment can then be written as

$$\boldsymbol{\mu_L} = \frac{q}{2m}\boldsymbol{L} \tag{III.13}$$

Quantum mechanically, nucleons have in addition to an orbital angular momentum also an intrinsic angular momentum, the spin. The magnetic dipole operator then originates from both the orbital as well as the spin part of the angular momentum. Because of the additivity of the dipole operator, the nuclear magnetic dipole operator can be written as the sum of the one-nucleon operators

$$\hat{\boldsymbol{\mu}} = \frac{\mu_N}{\hbar}\left(\sum_i^A g_L^i \hat{\boldsymbol{L}}^i + \sum_i^A g_S^i \hat{\boldsymbol{S}}^i\right) \tag{III.14}$$

Here $\mu_N = \frac{e\hbar}{2m_p}$ is the nuclear magneton and the dimensionless g-factors g_L and g_S are the orbital and spin gyromagnetic ratios. For a proton (π) $g_S^\pi = 5.585694675(57)$ and $g_L^\pi = 1$, while for a neutron (ν) $g_S^\nu = -3.82608545(90)$ and $g_L^\nu = 0$. This expression is usually rewritten in terms of the nuclear spin $\hat{\boldsymbol{I}} = \hat{\boldsymbol{L}} + \hat{\boldsymbol{S}}$

$$\hat{\boldsymbol{\mu}} = \frac{g\mu_N}{\hbar}\hat{\boldsymbol{I}} \tag{III.15}$$

The magnetic moment of the nucleus which is experimentally observed is the expectation value of the z-component of this operator for the state $|I, m_I = I\rangle$

$$\begin{aligned}\mu &= \langle I, m_I = I|\hat{\boldsymbol{\mu}}_z|I, m_I = I\rangle \\ &= g\mu_N I\end{aligned} \tag{III.16}$$

Note that the magnetic moment is expressed in units of nuclear magneton.

The magnetic moment is a very sensitive probe to study the nuclear structure. This can be understood by examining the case of an odd nucleus and an odd-odd nucleus in the single-particle model.
In the extreme single-particle model, the magnetic moment for an *odd nucleus* is defined by the last unpaired valence nucleon[2]. This single-nucleon magnetic moment for a proton or neutron in an orbital defined by the quantum numbers l, s and j, is given by the Schmidt moment [47]

$$\mu\left(j = l + 1/2\right) = \left[\left(j - \frac{1}{2}\right)g_L + \frac{1}{2}g_S\right]\mu_N \tag{III.17}$$

$$\mu\left(j = l - 1/2\right) = \frac{j}{j+1}\left[\left(j + \frac{3}{2}\right)g_L - \frac{1}{2}g_S\right]\mu_N \tag{III.18}$$

The experimentally found values usually deviate considerably from the Schmidt values. This deviation partly originates from the assumption that the g-factors inside a nucleus are the same as the free-nucleon g-factors. A simple correction consists of introducing effective g-factors which take into account the interaction of the core with the valence nucleon (core polarization) and the influence of the meson exchange current [48]. Typical values for this effective g-factors are $g_S^{\text{eff}} \approx 0.7 g_S$ and $g_L^{\text{eff}} \approx g_L$ [49].
For an *odd-odd nucleus* with spin I in which the odd proton (l_1, j_1) and odd neutron (l_2, j_2) are

[2]The other nucleons are assumed to be paired to spin 0 so they do not contribute to the total magnetic moment.

weakly bound, the magnetic moment can be expressed in terms of the single-nucleon magnetic moments of this odd proton $\mu(j_1)$ and neutron $\mu(j_2)$ [50]

$$\mu(I) = I\left[\frac{1}{2}\left(\frac{\mu(j_1)}{j_1} + \frac{\mu(j_2)}{j_2}\right) + \frac{1}{2}\left(\frac{\mu(j_1)}{j_1} - \frac{\mu(j_2)}{j_2}\right)\frac{j_1(j_1+1) - j_2(j_2+1)}{I(I+1)}\right] \tag{III.19}$$

These examples illustrate the dependence of the nuclear magnetic moment on the orbital which is occupied by the unpaired valence nucleon(s). The magnetic moment is therefore very sensitive to the configuration of the nucleons in their shells. Hence, the measurement of the magnetic moment allows a test of the validity of an assumed configuration. Although in general, the picture presented above is too simple, the concept that the magnetic moment is sensitive to the nuclear configuration remains valid.
As a last remark it is noted that the magnetic moment is not a good probe to investigate collectivity and deformation. In order to study those properties, the charge radii and quadrupole moments are more appropriate.

2.2 Electric quadrupole moment

Classically, the quadrupole moment induced by a collection of charges q_i is given by

$$Q = \sum_i q_i(3z_i^2 - r_i^2) \tag{III.20}$$

Here q_i, z_i and r_i are respectively the charge, z-coordinate and the radial coordinate of the i^{th} charge. It is clear that this expression vanishes if the charges move in a spherical symmetric way.
The quadrupole moment operator for a nucleus is however more conveniently expressed in a spherical tensor basis

$$\hat{\boldsymbol{Q}} = \sqrt{\frac{16\pi}{5}}\sum_i^A q_i \hat{r}_i^2 \boldsymbol{Y}_2(\theta_i, \varphi_i) \tag{III.21}$$

where $\boldsymbol{Y}_2$ are the spherical harmonic functions of rank two. Similar as in the dipole case, the experimental accessible quantity is the expectation value of $\hat{Q}_z = \hat{Q}_2^0$ for a state $|I, m_I = I\rangle$ which is called the spectroscopic quadrupole moment Q_s

$$Q_s = \langle I, m_I = I|\hat{Q}_2^0|I, m_I = I\rangle \tag{III.22}$$

The spectroscopic quadrupole moment is expressed in units of $e\text{fm}^2$ and is a measure of the average deviation of the nuclear charge distribution from spherical symmetry. When $Q_s > 0$ the nucleus has a prolate (cigar-shaped) deformation, while when $Q_s < 0$ it has an oblate (disc-shaped) deformation. Using the Wigner-Eckhart theorem [50], eq. III.22 can be expressed as function of the intrinsic quadrupole moment which is independent of the chosen axis system [49]

$$Q_s = \sqrt{\frac{16\pi}{5}}\sqrt{\frac{I(2I-1)}{(I+1)(2I+3)(2I+1)}}Q_{\text{int}} \tag{III.23}$$

Expression III.23 implies that nuclei with spin $I = 0$ or $I = 1/2$ have a zero spectroscopic quadrupole moment, although they can be intrinsically deformed.

Also in this case, it is possible to discuss the quadrupole moments in the framework of the shell model and the single particle moments of the valence nucleons. This will only be a good approximation for near-spherical nuclei close to closed shells. In between the shell closures the nuclei are often well deformed and a collective model such as the liquid drop model is more adequate to describe the nucleus.

3 Hyperfine structure and coupling constants

Atoms are not only composed of a nucleus, but also of an electron cloud which surrounds this nucleus. The interaction of the nuclear moments with the field produced by the atomic electrons is called the hyperfine interaction and is responsible for a splitting of the atomic energy levels. Because the magnitude of the splitting depends on the details of the nuclear structure, measuring this hyperfine splitting offers a direct way to gain information on the properties of the nucleus.
As an example the hyperfine structure of ^{67}Cu is shown in fig. III.1. The A-parameters and B-parameter contain, respectively, information on the magnetic moment and quadrupole moment of the nucleus.

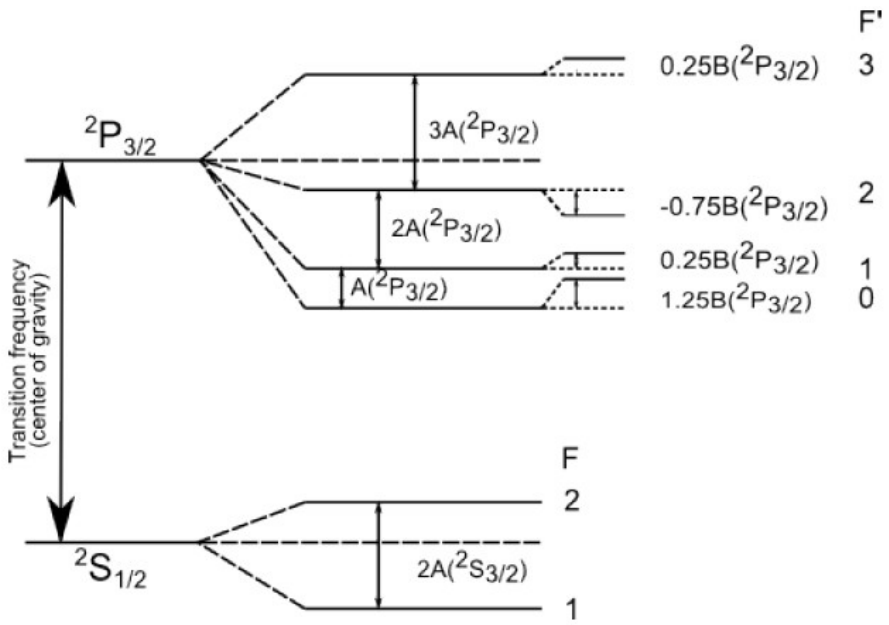

FIG. III.1: The hyperfine structure of ^{67}Cu ($I = 3/2$). Picture taken from [51].

In a free atom, not disturbed by external fields, the electronic spin $\boldsymbol{J}$ and nuclear spin $\boldsymbol{I}$ are coupled to a total angular momentum $\boldsymbol{F}$. Each value of F represents a different mutual orientation of I and J, ranging from parallel to antiparallel and thus F is restricted by $|I-J| \leq F \leq I+J$. Due to the electron-nucleus interaction each atomic level J is split in $2J+1$ (if $J < I$) or $2I+1$ (if $I < J$) sublevels characterized by F. The hyperfine structure is studied by inducing optical transitions between the F levels but it should be kept in mind that not every transition is allowed. For the dominant electric dipole transitions between a state $|IJ, Fm_F\rangle$ and $|IJ, F'm'_{F'}\rangle$,

following selection rules apply

$$\Delta F = 0, \pm 1$$
$$F = 0 \nrightarrow F' = 0 \tag{III.24}$$

The transitions in the hyperfine multiplet are characterized by specific relative intensities, theoretically given by the Racah coefficients [52]

$$I(F, F') \propto (2F+1)(2F'+1) \begin{Bmatrix} J' & F' & I \\ F & J & 1 \end{Bmatrix}^2 \tag{III.25}$$

Here the factor in curly brackets is the Wigner $6j$ symbol. The Racah intensities give a useful indication on which relative intensities should be expected although the exact empirical values are modified due to optical pumping between the hyperfine levels. There does not yet exist a fully satisfying description for this effect but in a previous experiment it has been shown that the relative intensities for a specific spin remain constant during the entire experiment for the same laser power [53]. This property offers a interesting tool in the analysis of hyperfine spectra.

The hyperfine hamiltonian is added as a small perturbation to the hamiltonian which describes the system without electron-nucleus interaction. This interaction hamiltonian consists of an expansion of the nuclear moments multiplied with the electromagnetic fields generated by the electrons

$$\hat{H}_{\text{int}} = \sum_{k=0} \hat{Q}^k \otimes \hat{V}^k \tag{III.26}$$

Here $\hat{Q}^k$ and $\hat{V}^k$ represent the k^{th} order term of respectively the nuclear moment and electronic field. For optical spectroscopy purposes, it is sufficient to consider the magnetic dipole contribution and the electric quadrupole contributions. These are the subject of the following sections.

3.1 The magnetic dipole interaction

The first-order term in the interaction hamiltonian is given by the potential energy of a dipole in a magnetic field. After all, the energy splitting is due to interaction of the nuclear dipole moment with the magnetic field generated by the atomic electrons at the position of the nucleus

$$\begin{aligned} \hat{H}_{\text{dip}} &= -\hat{\boldsymbol{\mu}} \cdot \hat{\boldsymbol{B}}(0) \\ &= -\frac{\mu B}{\hbar^2 I J} \hat{\boldsymbol{I}} \cdot \hat{\boldsymbol{J}} \end{aligned} \tag{III.27}$$

In the last line the magnetic dipole operator is replaced by its explicit expression (eq. III.15) and it is used that the magnetic field at the center of a current loop is parallel to the angular momentum of the moving charges. Usually this is written more compactly by introducing the hyperfine coupling constant A

$$A = \frac{\mu B}{IJ} \tag{III.28}$$

For $I = 0$ or $J = 0$ the A-parameter is defined to be zero, as an electron cloud with angular moment 0 does not give rise to a magnetic field nor does a nucleus with spin 0 have a magnetic

moment. By means of the well-known expression $2\hat{\boldsymbol{I}}\cdot\hat{\boldsymbol{J}} = \hat{F}^2 - \hat{I}^2 - \hat{J}^2$, the contribution of the dipole interaction to the energy splitting for a state $|IJ, Fm_F\rangle = |F\rangle$ can be calculated

$$\begin{aligned}\Delta E_{\text{dip}} &= -\frac{A}{2\hbar^2}\langle F|\hat{F}^2 - \hat{I}^2 - \hat{J}^2|F\rangle \\ &= -\frac{A}{2}\left[F(F+1) - I(I+1) - J(J+1)\right] \\ &= -\frac{A}{2}C(I,J,F) \end{aligned} \tag{III.29}$$

This expression defines the energy difference between the unperturbed state $|J\rangle$ and the hyperfine level $|F\rangle$ due to the magnetic dipole interaction. From now on the short-hand notation $C = C(I,J,F) = F(F+1) - I(I+1) - J(J+1)$ is used.

The coupling constant A contains the information on the nuclear moment and it is also this parameter which can be determined with laser spectroscopy. The electronic contribution to A for a certain atomic state is the same over the isotope chain. Consequently the magnetic moment of the measured isotopes can be determined relative to that of a reference isotope using

$$\mu = \frac{AI}{A_{\text{ref}}I_{\text{ref}}}\mu_{\text{ref}} \tag{III.30}$$

given that the A-parameter and magnetic moment is known for a reference isotope. Strictly speaking, this expression is only valid for a point dipole moment. In reality, the nucleus occupies some volume in space and s and relativistic $p_{1/2}$ electrons can penetrate the nuclear volume. In this case, the hyperfine interaction is influenced by how the nuclear moment is distributed over the nuclear volume. This effect, due to the extended nuclear magnetization, is called the Bohr-Weisskopf effect and leads to a correction of eq. III.30 [54]

$$\mu = \frac{AI}{A_{\text{ref}}I_{\text{ref}}}\mu_{\text{ref}}\,(1+\Delta) \tag{III.31}$$

where Δ is called the hyperfine anomaly. In many cases and in particular when the hyperfine anomaly is smaller than the experimental errors, eq. III.30 can be used.
In general, the Bohr-Weisskopf effect has to be taken into account when dealing with the ratio of the hyperfine coupling constants. A specific example which will be used later on, is the ratio of A-parameters of different atomic levels i, j for two isotopes A and A' [3] which is given by

$$\frac{A^A(i)}{A^A(j)} = \frac{A^{A'}(i)}{A^{A'}(j)}\,(1+\Delta) \tag{III.32}$$

3.2 The electric quadrupole interaction

The second significant term in the interaction hamiltonian is due to the interaction of the quadrupole moment of the nucleus with the electric field gradient produced by the electron cloud [55]

$$\hat{H}_{\text{quad}} = -\frac{1}{6}\hat{\boldsymbol{Q}}\cdot\nabla\boldsymbol{E} \tag{III.33}$$

[3] Both for the hyperfine coupling constant and for the mass number the same symbol is used in this text. From the context it should be clear which meaning is intended. In this specific section, the A's in superscript alway signify the mass numbers.

where the electric field gradient $\nabla E_{ij} = -\partial V/\partial x_i \partial y_i$ is a function of the electrostatic potential. This interaction shifts the energy with an amount ΔE_{quad} with respect to the unperturbed levels with [56]

$$\Delta E_{\text{quad}} = B\frac{3C(C+1) - 4I(I+1)J(J+1)}{8I(2I-1)J(2J-1)} \tag{III.34}$$

In this expression a second hyperfine coupling constant B is introduced, related to the spectroscopic quadrupole moment

$$B = eQ_s\frac{\partial^2 V}{\partial z^2} \tag{III.35}$$

Note that for an atom with $I < 1$ or $J < 1$ no hyperfine splitting due to the quadrupole interaction arises. This means that for the transition studied in this thesis $^2S_{1/2} \rightarrow {}^2P_{1/2}$, the only splitting is due to the magnetic term. For this reason, the quadrupole interaction will not be considered anymore in the remainder of this thesis. The sections on the quadrupole moment and the quadrupole interaction are only presented to give a more complete picture of the hyperfine interaction.

4 Collinear laser spectroscopy

The splitting induced by the electron-nucleus interaction is small compared to the energy of the total atomic system. To place this into perspective, the nuclear energy scale is in the order of keV-MeV, the electronic energy levels are separated by a few eV and the spin-orbit interaction of the electrons causes a splitting of a few meV. The hyperfine splitting however, is three orders of magnitude smaller, in the order of μeV[4]. To be able to measure the hyperfine structure, a high-precision technique is needed. The collinear laser spectroscopy method delivers the required precision by reducing the doppler broadening.

The concept of collinear laser spectroscopy is quite straight-forward. A fast ion beam is collinearly superimposed with a laser. The photons interact with the ions and when the laser frequency matches the frequency of a transition between the hyperfine levels, resonant excitation takes place. Afterwards, the fluorescent decay is observed in a light detection system.
To measure the entire hyperfine structure, the laser frequency is scanned across the resonances. This can be achieved by actually tuning the laser itself but in practice, this is difficult to accomplish. An easier solution takes advantage of the doppler effect. Indeed, in the reference frame of the accelerated ions the laser frequency ν_L is shifted according to

$$\nu_{\text{ion}} = \nu_L\sqrt{\frac{1-\beta}{1+\beta}} \tag{III.36}$$

with β the often used relativistic symbol

$$\beta = \frac{v}{c} = \sqrt{1 - \left(\frac{Mc^2}{eV_{\text{acc}} + Mc^2}\right)^2} \tag{III.37}$$

[4]Energy and frequency is often used interchangeable, for a quick conversion 1 μeV corresponds to about 250 MHz.

Hence, changing the acceleration voltage V_{acc} modifies the frequency ν_{ion} seen by the ions and the hyperfine structure can be scanned with this so-called *Doppler tuning*.

The use of accelerated ions also enables to overcome the resolution limits set by the doppler broadening of the spectral lines. Regardless of the technique used, a spectral line always has a intrinsic non-zero width, related to the finite lifetime of the states under consideration. Besides this natural linewidth, the thermal motions of the atoms cause an additional broadening. At a temperature T, the thermal velocities v are distributed according to the Maxwell-Boltzmann distribution and the doppler width $\delta\nu_D$ for an atom of mass M and optical transition frequency ν_{trans} is given by [57]

$$\begin{aligned}\delta\nu_D &= \nu_{\text{trans}}\frac{\delta v}{c} \\ &= \frac{\nu}{c}\sqrt{\frac{8k_BT\ln 2}{M}}\end{aligned} \tag{III.38}$$

With a typical value of several GHz, this width is commonly bigger than the hyperfine splitting. By using accelerated beams, as in collinear laser spectroscopy, it is however possible to reduce the doppler-broadening to a level comparable with the natural linewidth.
When the ions leave the ion source, they have a certain spread on the kinetic energy δE. Upon acceleration, all ions get the same increase in kinetic energy eV_{acc} and the energy spread remains constant. An increase in velocity then results in a reduced velocity spread due to the well-known relation between energy and velocity

$$\delta E = \delta\frac{Mv^2}{2} = Mv\delta v \tag{III.39}$$

In combination with $v = \sqrt{2eV_{\text{acc}}/M}$ the expression for the doppler-width becomes

$$\delta\nu_D = \nu\frac{\delta E}{\sqrt{2eV_{\text{acc}}Mc^2}} \tag{III.40}$$

Given an original energy spread of about 1 eV and an acceleration of a few kV, the doppler width can be reduced to ~ 10 MHz, comparable to the natural line width.

Because the method relies on the detection of fluorescent photons, the main source of background is the collection of stray laser light in the photomultiplier tubes. The contribution of the background photons to the signal is reduced considerably when a bunched instead of a continuous beam of ions is used. With this improvement, it is possible to record photons only when the ion bunch passes in front of the photomultiplier tubes. By doing so, the detection limit is lowered from a minimum of 10^6 ions/s in continuous mode to 10^4 ion/s in bunched mode. This means that by installing an ion-buncher, exotic nuclei with much lower yields are within reach.

A spectral line observed in the hyperfine spectrum is never purely monochromatic since several effects contribute to a non-zero linewidth. For collinear laser spectroscopy, natural line broadening, thermal doppler broadening and homogeneous power broadening are the most relevant ones. This last contribution is related to the interaction of the laser with the atomic energy levels which can effectively shorten the lifetime of the atomic excited state. Due to the

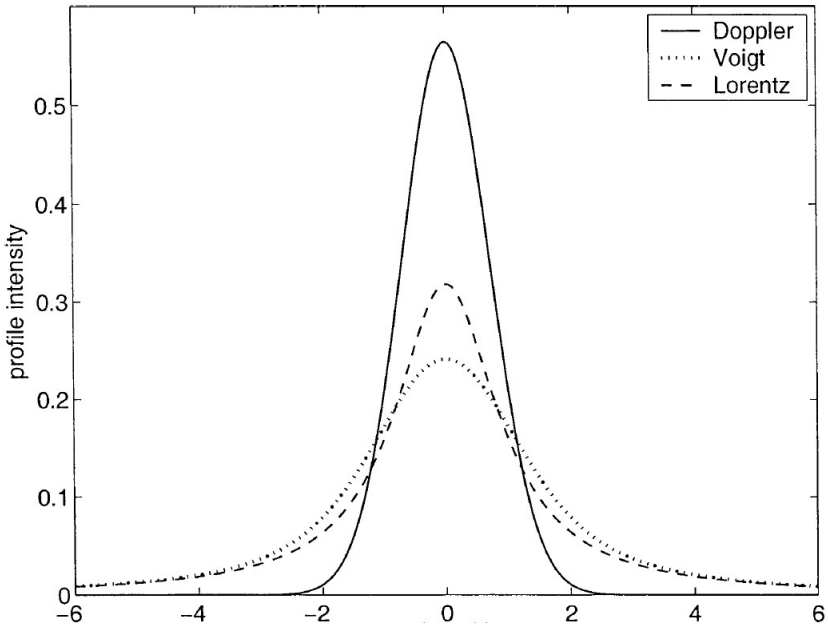

FIG. III.2: Comparison between a lorentzian, gaussian and voigt line profile. Picture taken from [58].

uncertainty principle, this mechanism is responsible for a broadening of the line shape. The amount of broadening depends on the laser power, where higher powers result in an increased line width.
Both power broadening and natural line broadening result in a lorentzian line profile

$$L(\nu, \nu_{\text{trans}}, \Gamma) = \frac{1}{\pi}\left[\frac{\Gamma/2}{(\nu - \nu_{\text{trans}})^2 + \Gamma^2/4}\right] \tag{III.41}$$

where Γ is the full-width at half maximum (FWHM). On the other hand, the effect of doppler broadening is more accurately described by a gaussian line profile

$$G(\nu, \nu_{\text{trans}}, \sigma) = \frac{1}{\sigma\sqrt{2\pi}} \exp\left(-\frac{(\nu - \nu_{\text{trans}})^2}{2\sigma^2}\right) \tag{III.42}$$

where $2\sqrt{2\ln 2}\sigma$ gives the FWHM.
Although the doppler broadening in collinear laser spectroscopy is greatly reduced, also the gaussian component has to be included in the spectral line. This yields a voigt profile, the convolution of a lorentzian profile and a gaussian profile, which is used in the analysis the spectra. All three line profiles are compared in fig. III.2.

Chapter IV

The experiment

In november 2010, a first experimental run to determine the ground-state properties of the neutron rich potassium isotopes was performed at ISOLDE, CERN [59]. The magnetic moments, spins and isotope shifts of $^{48\text{-}50}$K were successfully measured for the first time, together with a re-measurement of the hyperfine spectra of ^{38,39,42,44,46,47}K. Due to a severe beam contamination at mass 51, it was however not possible to measure the hyperfine structure of $^{51}_{19}K_{32}$. Therefore a new experimental run was realized in the summer of 2011 [60]. The main goal of this experiment was to extend the measurements of the isotope shift to $N = 32$ and to determine ground-state spin and structure of ^{51}K through the measurement of the hyperfine spectrum.

The potassium isotopes were studied with bunched-beam collinear laser spectroscopy at the COLLAPS beam line. The $4s\ ^2S_{1/2} \rightarrow 4p\ ^2P_{1/2}$ transition at 769 nm was chosen as optical transition with which the nuclear ground state properties were investigated. Since this D_1 transition is not sensitive to the quadrupole moments, only the magnetic moments, spins and isotope shifts can be determined in this experimental campaign.

During the experiment of 2011, the hyperfine spectra of 5 neutron-rich potassium isotopes were obtained in 5 days of measurements. An overview of the properties of these isotopes can be found in table IV.1. The hyperfine structure for each isotope was measured in several independent measurements. In order to be able to minimize influences of time-dependent drifts in the experimental set-up, measurements of the hyperfine spectrum of the reference isotope (^{47}K) were alternated with the measurements of other isotopes.

	I	$T_{1/2}$ [63]	Mass [64] (u)	$A(^2S_{1/2})$ (MHz)	$A(^2P_{1/2})$ (MHz)	$\delta\nu^{47,A}$ (MHz)
^{39}K	3/2	Stable	38.96370648636(492)	231.0(3)	27.5(4)	-857.5(17)
^{42}K	2	12.321(25) h	41.962402306(113)	unknown	-60.6(16)	-505.8(25)
^{47}K	1/2	17.50(24) s	46.961664836(2700)	3420(29)	411.9(50)	0
^{50}K	(0 or 1) [61, 62]	472(4) ms	49.972370747(3671)	0	0	unknown
^{51}K	(3/2) [32]	365(5) ms	50.976850(640)	unknown	unknown	unknown

TABLE IV.1: The spin (as it was known before the 2010 experiment), half-life and mass of the measured K-isotopes. The last columns show the A-parameters and isotope shifts, as found in the work of Touchard [20].

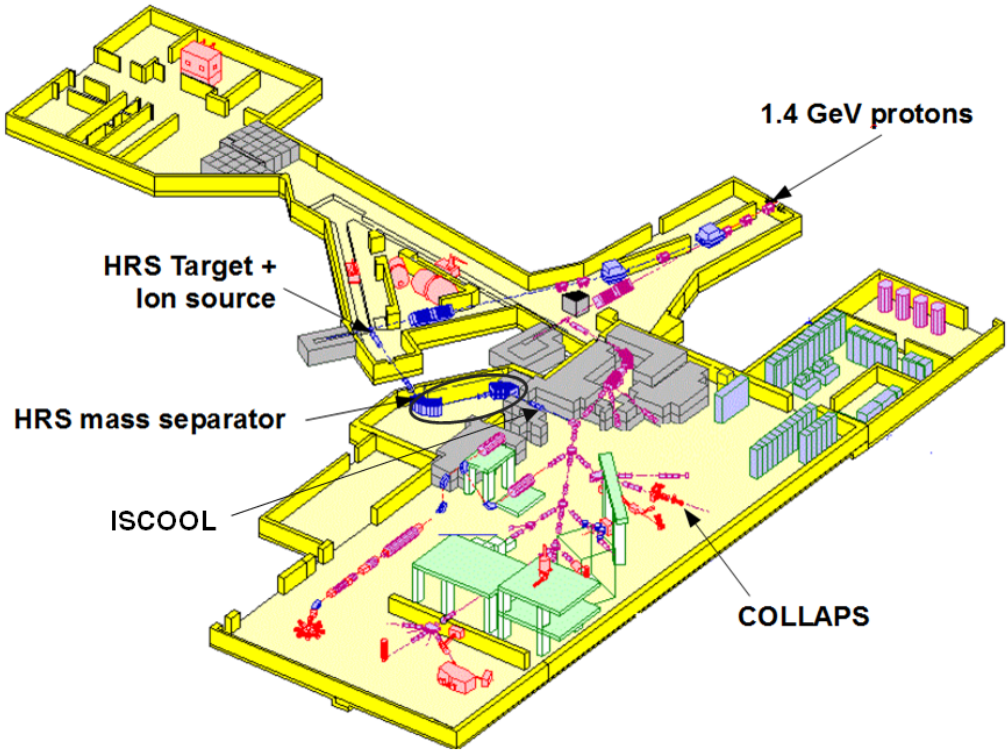

FIG. IV.1: Lay-out of the ISOLDE experimental hall at CERN. Important elements are indicated with an arrow and discussed in more detail in the text.

1 Collinear laser spectroscopy at ISOLDE

1.1 The ISOLDE facility

The neutron-rich potassium isotopes and other short-lived nuclei have to be produced in dedicated facilities such as ISOLDE. This facility is located at the site of the European Organization for Nuclear Research (CERN) in Geneva and has produced more than 600 different kinds of isotopes with half-lives down to milliseconds [65].
At ISOLDE, shown in fig. IV.1, the radioactive isotopes are produced and separated with the Isotope Separator On Line (ISOL) method. The Proton Synchrotron Booster (PSB) delivers 1.4 GeV proton bunches to the ISOLDE hall where they are used to irradiate a thick, hot target. This produces a wide variety of (exotic) nuclei via spallation, fission and fragmentation reactions. Heating the target ensures a fast diffusion of the reaction products out of the target into the ion source. Depending on the specific requirements, three different ionization methods can be used: surface, plasma or laser ionization. The ions are subsequently guided to one of the two mass separators, the General Purpose Separator (GPS) or the High Resolution Separator (HRS). As the names suggest, HRS offers the highest mass resolving power ($M/\Delta M \approx 5000$) but GPS ($M/\Delta M \approx 2400$) on the other hand, is able to deliver three different beams simultaneously into the experimental hall. Finally, the mass-separated ions are accelerated up to 60 keV and fed to the experimental installations where fundamental research in many fields of nuclear, atomic, solid-state physics and related sciences is conducted.

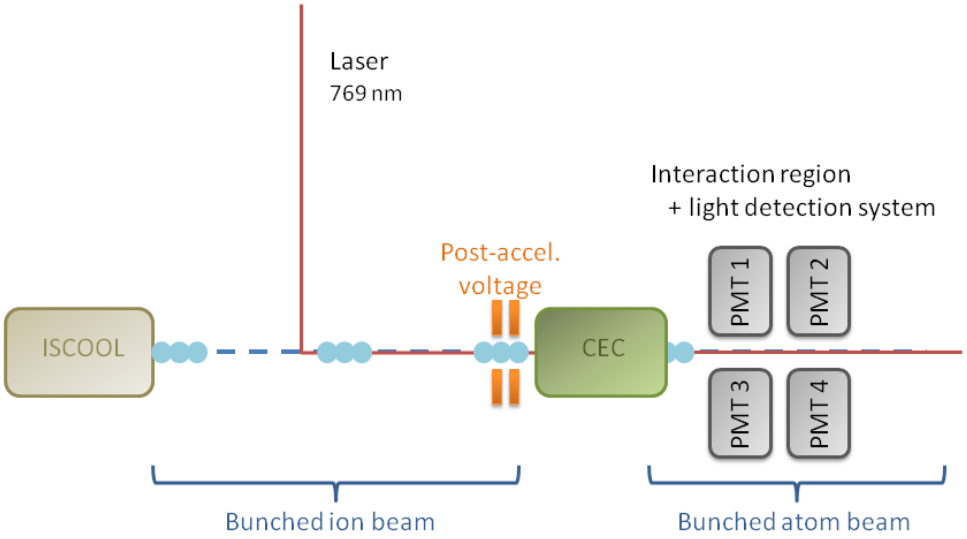

FIG. IV.2: Schematic depiction of the COLLAPS beam line located in the ISOLDE hall at CERN. Detailed information can be found in the text.

In the potassium experiments, the isotopes are produced by the bombardment of a 48 g/cm^2 thick UC_x target. Afterwards, they are ionized in a surface ionization source and mass separated in HRS. The production rates of the potassium isotopes can in principle be found on the Yield Database of the ISOLDE website [65]. However, yield measurements on the ISOLDE tape station performed before the experiment in 2010 reported three times lower yields than quoted on this database.

1.2 The COLLAPS beamline

In ISOLDE, the collinear laser spectroscopy experiments are performed at the COLLAPS beam line, depicted in fig. IV.2.
For the purpose of doing bunched-beam laser spectroscopy, a gas-filled Paul-trap (ISCOOL) was installed in the focal plane of HRS in 2007 [66]. The ions are slowed down due to collisions with the gas particles in the trap while the trapping potential is generated by 4 quadrupole rods on which a RF field is applied. The ions are accumulated for around 100 ms after which they are released in bunches of ions of about 10 μs. Before the bunched ions are injected in the beam line, they are reaccelerated to 30 keV with the ISCOOL acceleration voltage V_{ISCOOL}.
In the first stage of the COLLAPS beam line, the bunched ions pass the post-acceleration region in which they are accelerated with an voltage $V_{\text{post-acc}}$ appropriate for the specific mass of the isotope, ranging from -10 to 10 kV. Also in this region, a voltage V_{scan} is applied to scan across the resonances of the hyperfine structure. The scanning voltage itself is limited to voltages of $\pm$10V but to increase the range of the doppler tuning, V_{scan} is amplified with a factor $k \sim 50$. Hence, the total voltage applied is the sum of three terms

$$V_{\text{acc}} = V_{\text{ISCOOL}} + V_{\text{post-acc}} + k \cdot V_{\text{scan}} \tag{IV.1}$$

Before the ions can interact with the co-propagating laser, they are neutralized by a hot alkali vapor in the charge exchange cell (CEC). In this process the fast (K^+) ions pass through a

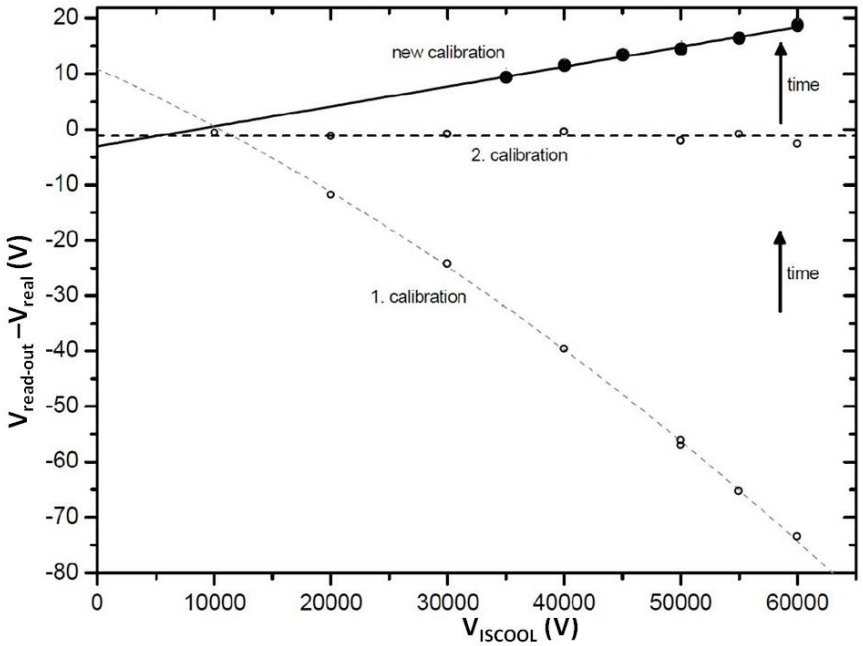

FIG. IV.3: The three calibrations of V_{ISCOOL} performed with high-precision voltage dividers. A discrepancy between the calibrations over time is observed. Picture taken from [67].

vapor cell of neutral atoms and they are neutralized via

$$\mathbf{K}^+ + \mathrm{K} \rightarrow \mathbf{K} + \mathrm{K}^+ + (\Delta E \approx 0) \tag{IV.2}$$

Here the bold symbols indicate the isotopes in the beam and the normal symbols indicate the isotopes in the CEC. Because the cross section for this reaction is very large (in the order of 10^{10} barn [57]), almost all ions are neutralized in the process. After neutralization the bunched atoms arrive at the interaction region. Here, the atoms are resonantly excited by the laser light. The subsequent fluorescence decay is detected by 4 independent photomultiplier tubes (PMT) which are placed perpendicular to the beam line.

1.3 The ISCOOL acceleration voltage

In collinear laser spectroscopy an exact knowledge of the acceleration voltage is indispensable. since it determines how good the laser frequency in the ions' rest frame is known, and thus how reliable the obtained results are.
For each hyperfine spectrum which is measured, the values of $V_{\text{post-acc}}$ and V_{scan} are recorded automatically. The amplification factor k is determined on several occasions during the experiment and is consistently measured to be $k = 50.4271(13)$. However, the determination of the exact value of V_{ISCOOL} poses a problem. The ISCOOL voltage divider is specified to have an accuracy of 0.2%, which implies an uncertainty of 60V on 30kV. This is greatly insufficient for laser spectroscopy purposes and therefore 3 external calibrations of the voltage divider were performed [67]. These showed a discrepancy between the read-out of the voltage divider and the real voltage output. Unfortunately, the different calibrations contradict each other (see fig. IV.3) and the correction voltage $V_{\text{corr}} = V_{\text{real}} - V_{\text{read-out}}$ which has to be added to eq. IV.1 is

assumed to vary in time. Because it is not possible to calibrate the voltage divider for each separate experiment, the correction voltage has to be determined in an indirect way as described in section 3.4.

1.4 The light detection system

The peak response of the Burle 8852 photomultiplier tubes is around 550 nm. The wavelength of the fluorescence photons of the D_1 transition in potassium is however at 769 nm, a wavelength at which the spectral response is about 50% lower than at its maximum. With originally 2 PMTs in the set-up, this resulted in a detection efficiency of 1 photon in $3 \cdot 10^5$ K-ions. In order to be able to measure the hyperfine spectra of the exotic potassium isotopes, the detection efficiency had to be improved by a factor of 10. Therefore, a better lens geometry was designed and the number of PMTs was doubled from 2 to 4 [60].

In the experiment performed in 2010, a huge beam-induced photon background was observed in the hyperfine spectra of ^{51}K. This could be attributed to a beam contamination at mass 51. The contaminating ions were collisionally excited in the charge exchange cell producing fluorescence photons in the de-excitement. Due to this noise, it was impossible to get an acceptable hyperfine spectrum of ^{51}K in a reasonable amount of time. Luckily, the background photons do not have the same frequency as the potassium photons. Therefore, in the 2011 experiment the problem could be circumvented by placing a frequency filter in front of the lens. Consequently, a successful measurement of the hyperfine spectrum of ^{51}K was possible in 2011.

2 Data collection

During the experiment the data are collected with MCP, the Measurement and Control Program. In this program, the spectra are recorded as the number of photon counts versus the scanning voltage. This is recorded for each photomultiplier tube separately, with the option to combine these separate spectra in one spectrum. Other information which can be extracted from the mcp-file is the time at which the spectra are recorded, the exact post-acceleration and scan voltage, the number of scanning steps and step size. In the case that the left and right multiplet[1]are recorded in separate tracks, also the number of scans of each multiplet is recorded. The precise laser wavenumber can not be found in the mcp-file but is saved in a separate file.
Another important source of information is the logbook which is kept to keep track of what happened during the experiment. Both the standard actions as well as the irregularities such as the laser frequency which is changed or proton pulses which are empty are noted down. Especially these irregularities have to be taken into account when deciding which spectra are good and which should be treated with more care.

In the mcp-file the spectra are recorded as counts versus *scanning voltage* but for further analysis

[1]The $^2S_{1/2}$ electronic level is split into two hyperfine levels. The resonances corresponding to excitations from the lowest energy level are well separated from the resonances corresponding to excitations from the second energy level. One often speaks of multiplets in the hyperfine spectrum. This is also visualized in fig. IV.4.

it will be necessary to convert the spectra to counts versus *frequency*. This conversion is done according to eq. III.36 and eq. III.37 where the masses M are given in table IV.1[2] and the total acceleration voltage is specified by eq. IV.1. The laser frequency $\nu_L = c\lambda^{-1}$ was locked to $\lambda^{-1} = 13001.3295\ \text{cm}^{-1}$ during the first 4 days of the experiment, while for the last day it was locked to $\lambda^{-1} = 13001.3205\ \text{cm}^{-1}$. In order to have the transition frequencies centered around $\nu_0 = 0$, the frequencies are shifted with the transition frequency of the D_1 line of ^{39}K: $\nu_{\text{shift}} = 389286058.716$ MHz [69].

3 Analysis

The main goal of the analysis is to extract the hyperfine structure constants ($A(^2S_{1/2})$ and $A(^2P_{1/2})$) and isotope shifts for each isotope. These parameters are determined by the position of the peaks in the spectrum. For the optical transition used in this experiment, the magnetic dipole term is the only non-negligible term contributing to the hyperfine splitting. The position of a peak i is then given by

$$\nu_i = -\frac{1}{2}C_i(I,J,F)A(^2S_{1/2}) + \frac{1}{2}C_i(I,J',F')A(^2P_{1/2}) + \nu_0 \tag{IV.3}$$

where each peak i corresponds to a particular transition between two hyperfine levels (characterized by F and F'). ν_0 is the fine structure transition frequency between $^2S_{1/2}$ and $^2P_{1/2}$, called the center of gravity or centroid frequency. The expression can be easily found by combining eq. III.29 for the two hyperfine levels under consideration. With eq. IV.3 as a condition on the positions of the resonances, it is possible to determine the $A(S_{1/2}), A(P_{1/2})$ and ν_0 in a fit.
The number of peaks in the spectrum is determined by the electronic spin J, the nuclear spin I and the allowed transitions given by the angular momentum coupling selection rules, eq. III.24. The determination of the peak positions for a certain level scheme is illustrated fig. IV.4. The corresponding hyperfine spectrum is added for clarity. A typical hyperfine spectrum for ^{39,42,47}K can be found in appendix A.

3.1 Fitting procedure

In the fitting procedure, the line shape of a resonance is described by a voigt profile and the positions of the resonances have to satisfy eq. IV.3. In a given hyperfine spectrum, the resonances are fitted with a common line width for all peaks.
In the fit a number of parameters are left as free fit parameters. These include the aforementioned parameters $\left(A(^2S_{1/2}), A(^2P_{1/2}) \text{ and } \nu_0\right)$ and also the height of the background, the intensity of each peak and the peak width. On each of these parameters an uncertainty ϵ_{par} is given, which is determined during the fit procedure.

[2] In February 2012, the results of a new mass measurement of $^{47-50}$K were published [68]. Due to the timing of this publication, these results could not be used in the analysis in this work. Because the difference between the masses used and the new published values is only minor, it is not expected that this will influence the results obtained in this work.

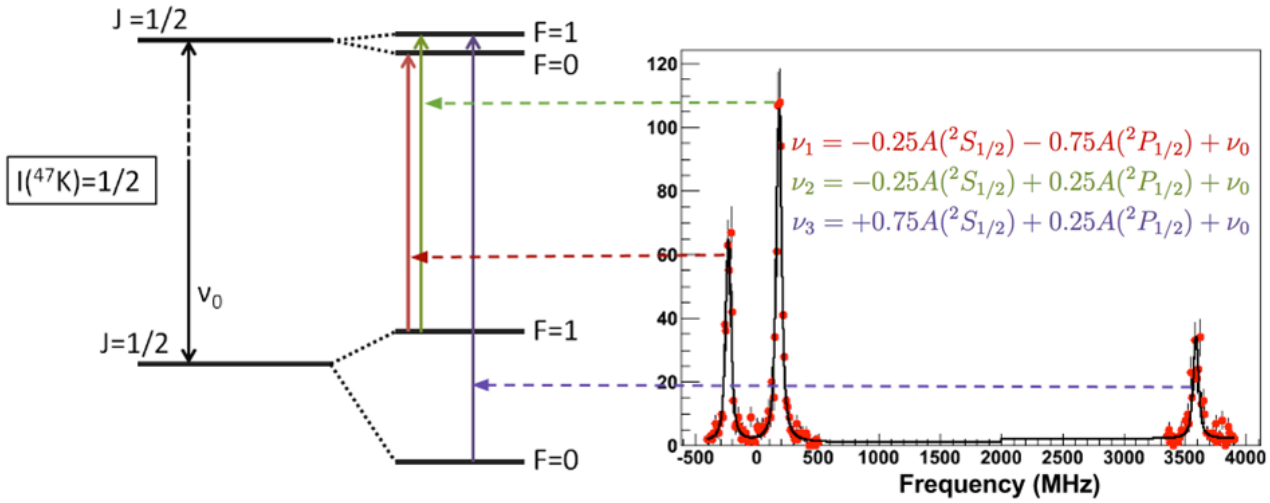

FIG. IV.4: Illustration of a hyperfine spectrum of ^{47}K with the expressions for the positions of the peaks indicated in the same color as the transition.

The experimental spectra are fitted with a script written in the ROOT framework based on the standard MINUIT fitting package. This yields the best-fit parameters using a χ^2 minimization procedure. The chi-square value gives the difference between the measured values n_i and the theoretical prediction given by the fit function $f_i(x)$, weighted by the errors on the measurement ϵ_i [70]

$$\chi^2 = \sum_i^N \frac{(n_i - f_i(x))^2}{\epsilon_i^2} \tag{IV.4}$$

Here N is the number of datapoints and x represents the fit parameters. Because n_i are the number of counts due to the statistical process of de-excitation through photon emission, the errors are given by $\epsilon_i = \sqrt{n_i}$.
For a good fit χ^2 should be roughly equal to the number of degrees of freedom[3] d or stated differently, the reduced chi-square $\chi^2_{\text{red}} = \chi^2/d$ should be around 1 [70]. When the χ^2_{red} is reasonably bigger, maybe two or three times as big, the proposed fit parameters are still accepted if the fitting function is believed to be correct. However in this case, the errors on these parameters are multiplied by the square root of the reduced chi-square. This multiplied error is then the statistical error on the parameter which is used in the further analysis and which corresponds to a 68% (1σ) confidence level.

In the analysis of the ^{51}K spectra it is not possible to leave all parameters free because of the bad resolution of the right multiplet. A more detailed description of this case follows in section 3.7.

[3]The number of degrees of freedom d is defined as the number of datapoint N minus the number of fit parameters.

3.2 Weighted mean and errors

When the results of N_{im} independent measurements are combined, the mean of an observable O weighted by the errors ϵ_i on the individual measurements is calculated by [70]

$$\langle O \rangle = \frac{\sum_i O_i/\epsilon_i^2}{\sum_i 1/\epsilon_i^2} \tag{IV.5}$$

The statistical uncertainty on this value given by

$$\epsilon_{\text{stat}}^2 = \frac{1}{\sum_i 1/\epsilon_i^2} \tag{IV.6}$$

If there is a considerable scatter in the values of the individual measurements, this statistical uncertainty does not represent the true uncertainty. In this case the error is specified better by

$$\epsilon_{\text{scat}}^2 = \frac{1}{1-\sum_i \varepsilon_i^4} \frac{1}{N_{\text{im}}} \sum_i^{N_{\text{im}}} \frac{(O_i - \langle O \rangle)^2}{\varepsilon_i^2} \tag{IV.7}$$

where ε_i are the normalized errors such that $\varepsilon_i^2 = \epsilon_i^2/\sum_i \epsilon_i^2$. The expression which gives the largest value should be taken as final error on $\langle O \rangle$. In general, there is a systematic error which should be added quadratically to this value to get the total error.

3.3 Selection of hyperfine spectra

	^{39}K	^{42}K	^{47}K	^{50}K	^{51}K
# runs	1	3	9	3	1

TABLE IV.2: Final number of hyperfine spectra per isotope.

In the experiment a total of 26 independent hyperfine spectra were recorded but not all of them can be used in the final analysis.
A good way to test the quality of the hyperfine spectra is by examining the fit parameters over a larger number of files. The ratio between $A(^2S_{1/2})$ and $A(^2P_{1/2})$ is quite constant over the isotopic chain, as shown in fig. IV.5a. There are however two files (no. 21 and no. 68) for which the ratio strongly deviates from the observed trend. These files are not taken into account in the calculation of the final A-parameters and isotope shifts. Similarly, there is one hyperfine spectrum of ^{47}K (no. 71) for which $A(^2S_{1/2})$ is considerably lower than for the other spectra, as can be seen in fig. IV.5b. Also this file is no longer considered in further analysis. Another two files can be excluded based on a unreasonable low gaussian width component (no. 64) and unreasonable low lorentzian width component (no. 58).
These inconsistencies can in most cases be traced back to unstable experimental conditions. During the recording of file no. 71, there were problems with a jumping laser frequency and after this recording the laser frequency is set to a different value. Also for spectrum no. 21, an instability in laser frequency is noticed. In between run no. 46 and run no. 64 the proton intensity was fluctuating in time, resulting in empty pulses[4] when the average proton current

[4]Due to safety considerations, the proton current on the target is limited to 2 μA. When the average current is temporally higher, there are "empty pulses" which means that although our data acquisition is triggered, no ions pass through the beam line.

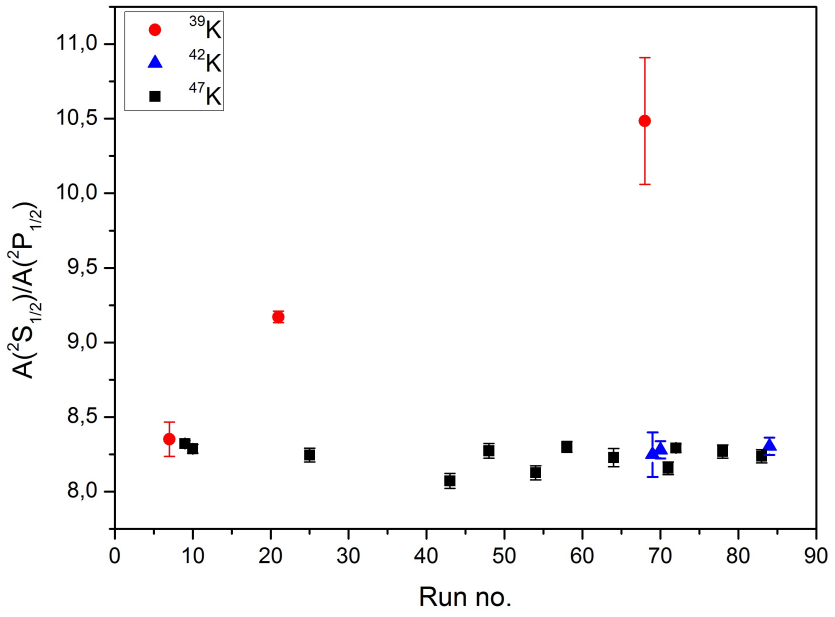

(a)

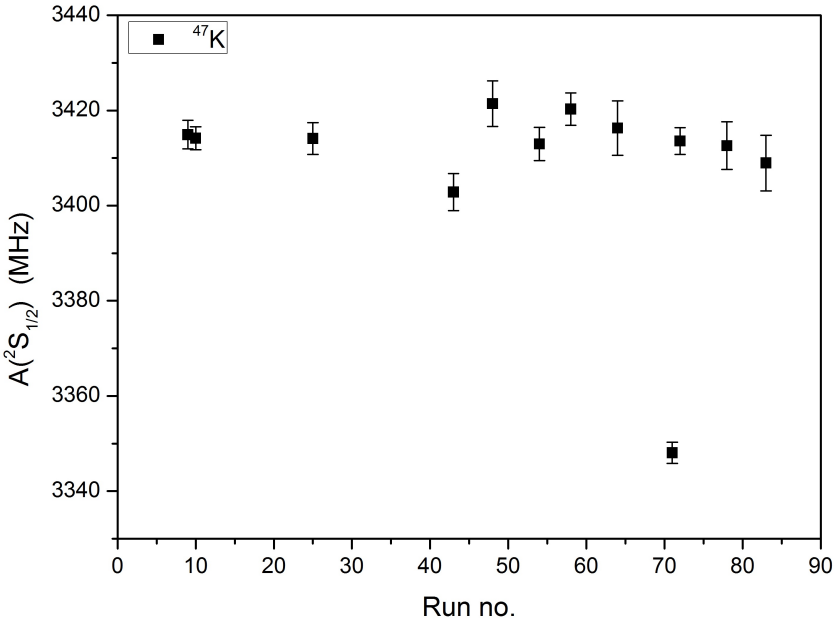

(b)

FIG. IV.5: (a) The ratio of the hyperfine coupling constants plotted over the all hyperfine spectra. (b) The hyperfine coupling constant for the $^2S_{1/2}$ level of ^{47}K plotted for all spectra obtained for this isotope.

on the target was higher than 2 μA.

Another inconvenience in the 2011 experiment, was that the proton beam had to be shared with another experimental set-up. This resulted in less ions coming through the COLLAPS beam line, increasing the time needed to measure a hyperfine spectrum. Especially for ^{51}K which already has a low yield, this influenced the quality (resolution) of the obtained spectra. Furthermore, one of the four PMTs broke down in the middle of the experiment which reduced the statistics as well.

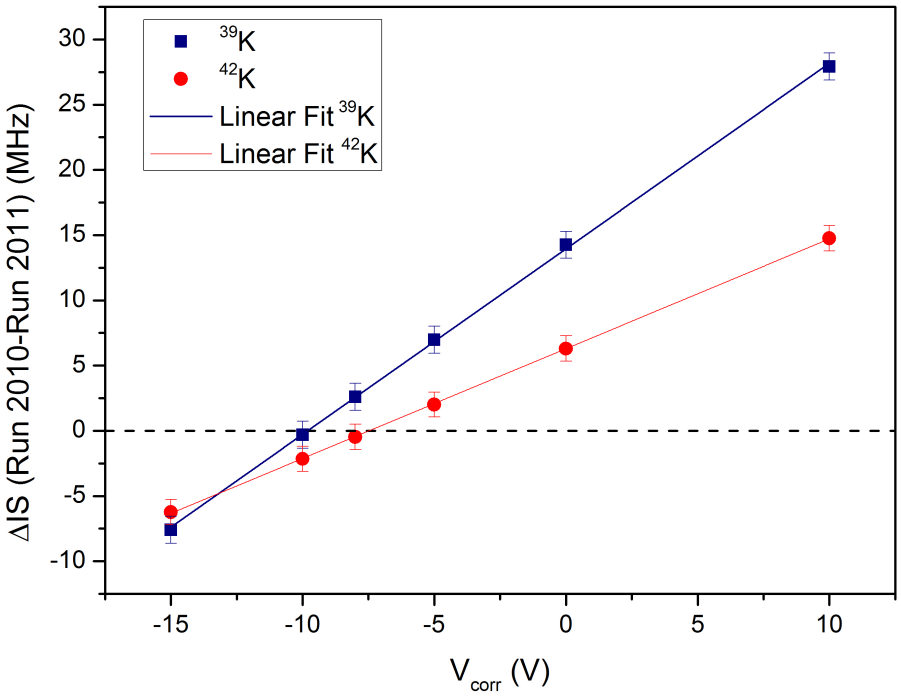

FIG. IV.6: The difference between the isotope shift from run 2010 and run 2011, calculated for different correction voltages. The difference is expressed in MHz. The full blue line, given by Δ IS^{39} = $1.42V_{\mathrm{corr}} + 13.95$ MHz, corresponds to the linear fit for ^{39}K. For ^{42}K the linear fit is the red full line which is described by Δ IS^{42} = $0.84V_{\mathrm{corr}} + 6.30$ MHz.

For 4 files (no. 22, 35, 36, 37) of ^{47}K only half of the hyperfine spectrum is recorded due to an erroneous setting in the measurement program. These files are not considered in the analysis because with only 1 multiplet it is expected that they will not render as accurate results as the other files. Furthermore, the spectrum of file no. 13 (^{50}K) shows a sudden peak in the background which is a clear indication of a strong fluctuation in the laser frequency.

In table. IV.2, the remaining number of independent hyperfine spectra per potassium isotope are summarized. As a general remark, it is noted that only a low number of hyperfine spectra can be used in the final analysis. In particular, for ^{39}K and ^{51}K there is only one useful spectrum. For a precise determination of the A-values and the isotope shifts, a higher number of spectra would be highly desirable.

3.4 ISCOOL correction voltage

To obtain reliable results, the correction voltage which has to be added to V_{ISCOOL} has to be determined. This is necessary because a difference as small as 1 V already has a considerable effect on the calculated isotope shifts. Because the different external calibrations of V_{ISCOOL} contradict each other [67], an indirect technique based on the measured isotope shifts is used in the determination of V_{corr}.

In this work, ^{47}K is taken as the reference isotope, so the isotope shift $\delta\nu^{47,A} = \nu_0^A - \nu_0^{47}$ is calculated with respect to ^{47}K. To reduce the influence of changing experimental conditions, the centroid frequencies ν_0^A and ν_0^{47} are always taken from spectra which were recorded in a short timespan of each other. The experimental values for different correction voltages can be compared to known values in literature. In particular, the isotope shifts were calculated for six different correction voltages: 10V, 0V, -5V, -8V, -10V and -15V. This is the range in which the correction voltage is expected to be based on previous runs and the external calibrations. The -8V value is the correction voltage predicted by the last calibration [67].
Because the isotope shifts for ^{39}K, ^{42}K and ^{50}K measured in the 2010 run [28] are in good agreement with the values known in literature [20] and in addition have a better precision, the 2010 values are used as the comparison values.

After more detailed inspection, the ^{50}K spectra are clearly asymmetric and the symmetric voigt line shape is an inappropriate fit function. Because fitting asymmetric data with a symmetric line shape has a severe effect on the center of gravity and therefore on the isotope shift, only the isotope shifts of ^{39}K and ^{42}K can be used to determine the correction voltage. A further discussion of the line shape of ^{50}K can be found in section 3.6.
In the 2010 experiment, it is calculated that $\delta\nu^{47,39} = -859.3(7)$ MHz and $\delta\nu^{47,42} = -506.8(6)$ MHz. The difference ΔIS between our measured value and this comparison value for each isotope is plotted in fig. IV.6.
For each isotope, it is possible to fit the data with a linear trend, shown as a full line on the graph. The voltage for which ΔIS corresponds to zero gives the preferred correction voltage for that isotope. Taking the average value for both isotopes gives a correction voltage of $V_{\text{corr}} = -9.2(12)$ V.
Given the slope of the linear fit, it is possible to estimate the systematic error on the isotope shift due to the uncertainty of 1.2 V on the correction voltage. Because the slope differs from isotope to isotope, this has in general to be determined for each isotope separately. For ^{39}K this results in an extra uncertainty of 1.7 MHz, while for ^{42}K 1 MHz uncertainty should be added.

Likewise, the hyperfine coupling constants A also vary linearly when the correction voltage is changed. In a similar way as for the isotope shifts, the error on the A-parameters caused by the uncertainty of on the correction voltage is determined. These errors are in the order of 0.01 MHz for both $A(^2S_{1/2})$ and $A(^2P_{1/2})$, which mean they are more than an order of magnitude smaller than the statistical errors and can safely be ignored.

3.5 The influence of fixing fit parameters

In general, it is preferred to keep all parameter mentioned in subsection 3.1 as free parameters to be determined in the fitting procedure. In the ^{51}K spectra, the statistics are too low to get reliable results and it will be necessary to fix some of the parameters to reasonable values. This requires a good knowledge of the fitting parameters found for the other isotopes and an investigation of the effect of fixing each of the parameters.

First the influence of fixing the ratio $R = A(^2S_{1/2})/A(^2P_{1/2})$ between the hyperfine coupling constants is considered. For elements with a very small hyperfine anomaly, this ratio is constant over the isotope chain. Because fixing the ratio reduces the parameters which constrain the

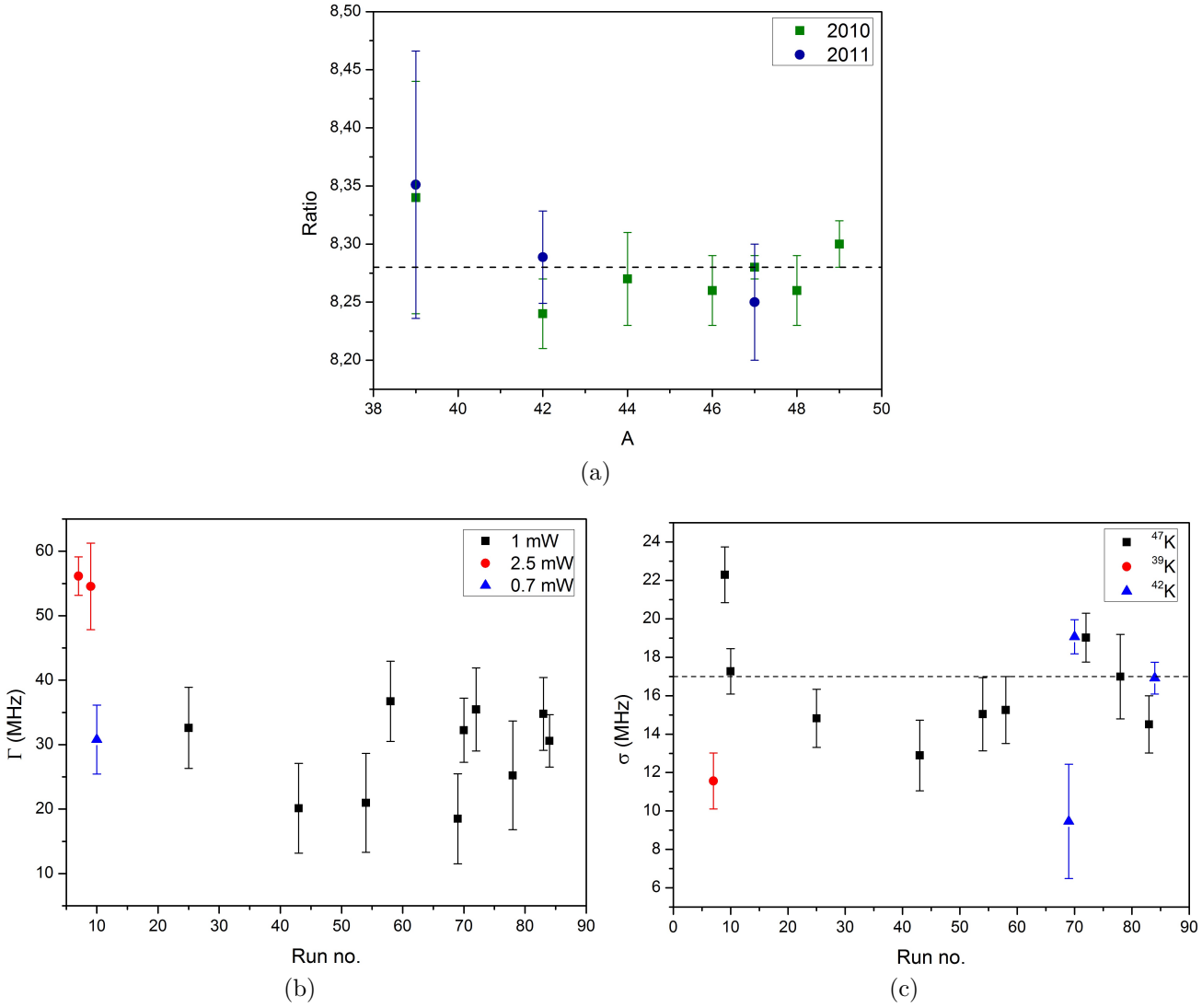

FIG. IV.7: a) The ratio of the hyperfine constants plotted for the neutron-rich potassium isotopes. The weighted mean value $\langle R \rangle = 8.278(8)$ is indicated by the dashed line. The mean value is completely determined by the small error on the ratio of ^{47}K obtained in 2010 [28]. (b) The lorentzian width found for the hyperfine spectra recorded at different laser powers. (c) The gaussian width found for the hyperfine spectra in which the lorentzian width is fixed as discussed in the text. The dashed line represents the mean value of the gaussian width $\langle \sigma \rangle = 16.8(8)$ MHz.

peak position from 3 to 2 (see eq. IV.3), it is a powerful and often used technique.
For the electronic levels important in our experiment, only the valence electron of the $^2S_{1/2}$ state has a considerable probability to penetrate the nuclear volume. Therefore, the following expression is valid

$$R = \frac{A^A(^2S_{1/2})}{A^A(^2P_{1/2})} = \frac{A^{A'}(^2S_{1/2})}{A^{A'}(^2P_{1/2})}\left(1 + {}^A\Delta^{A'}(^2S_{1/2})\right) \tag{IV.8}$$

This means that it is a good approximation to assume a constant ratio R if the hyperfine anomaly in the potassium isotopes is small. This anomaly is measured in only 4 cases: $^{39}\Delta^{37} = -0.00249(35)$ [71], $^{39}\Delta^{40} = 0.00466(19)$ [72], $^{39}\Delta^{41} = -0.00222936(14)$ [73] and $^{39}\Delta^{42} = 0.00336(38)$ [74]. These values are in the order of 0.005 which is small but certainly not insignificant.

In order to get a feeling what this means, the ratio R is plotted over the neutron-rich isotope chain (fig. IV.7a). In this plot information from 2010 (green) is combined with information from this work (blue). It can be seen that the ratio is quite consistent over the isotope chain, but there is some non negligible scatter around the mean value $\langle R \rangle = 8.278(8)$. Based on the trend in fig. IV.7a, the ratio of ^{51}K is expected to lie in between 8.24 and 8.35. Fixing the ratios for ^{39}K ($R^{2011} = 8.35(11)$), ^{42}K ($R^{2011} = 8.29(4)$) and ^{47}K ($R^{2011} = 8.25(5)$) to the mean value is therefore a good way to test the effect on ^{51}K. In the top row of fig. IV.8 (a and b), the difference in A and ν_0 between values obtained with a free ratio and with a fixed ratio, is shown. The effect on the center of gravity is smaller than the error bars and is therefore neglected in further analysis. However, there is a notable influence on the A-parameters. To estimate the additional uncertainty on the $A(^2S_{1/2})$ of ^{51}K, the average of the (absolute value of the) deviation is calculated: 1.4 MHz.

Secondly, the effect of fixing the width of the spectral lines is investigated.
The lorentzian contribution Γ to the width of the voigt profile is mainly influenced by the laser power and is in principle isotope independent. If the laser power is kept at a constant level during part of the experiment, it should be possible to find a common value for Γ for the spectra recorded in that period. The laser power was changed three times in the timespan of the experiment: for file 7 and 9 the laser power was set at 2.5 mW, for file 10 until file 20 the power was changed to 0.7 mW and for all other files the power was kept a constant level of 1 mW. The variation of Γ for the different recorded spectra is shown in fig. IV.7b. A clear difference is observed between the width at 2.5 mW and the width at 0.7 and 1 mW. Also there is a notable spread on the widths at the same laser power. However, when the A-parameters and centroid frequencies are compared for free Γ or for Γ fixed to the average at that laser power ($\Gamma^{2.5\text{mW}} = 55.9$ MHz and $\Gamma^{1\text{mW}} = 28.6$ MHz), the results are remarkable constant, see the middle row in fig. IV.8 (c and d). This gives confidence that fixing the lorentzian width is a good choice in order to decrease the number of free fit parameters in the analysis of ^{51}K.
It is also investigated what happens if the gaussian part of the width is constrained as well. With the lorentzian width fixed as discussed in the previous paragraph, the variation of the gaussian width σ is shown in fig. IV.7c. The gaussian width originates from the doppler broadening and differs from one isotope to another through the mass and V_{acc} in equation III.40. This isotope dependence is expected to be small and due to the large inherent spread, indistinguishable in the experimental data.
Although σ scatters with the same order of magnitude as Γ, fixing both widths does have an effect on the center of gravity, see fig. IV.8f. Since fixing the gaussian width introduces an additional error without gaining much in the fitting procedure[5], it is decided to leave this parameter free.

In the analysis of the hyperfine spectra of ^{51}K, the ratio and the lorentzian width will be constrained to their average value $\langle R \rangle = 8.278(8)$ and $\langle \Gamma \rangle = 28.6$ MHz.

[5]This has to be compared to the effect of fixing the ratio. If only the lorentzian and gaussian width would be fixed in the fitting procedure, it would still not be possible to fit the spectra of ^{51}K. However, imposing a fixed ratio is a much stronger constraint which does allow for a fit of the spectrum. In that sense, it is justified to fix the ratio and not the gaussian width although the first one causes a bigger error.

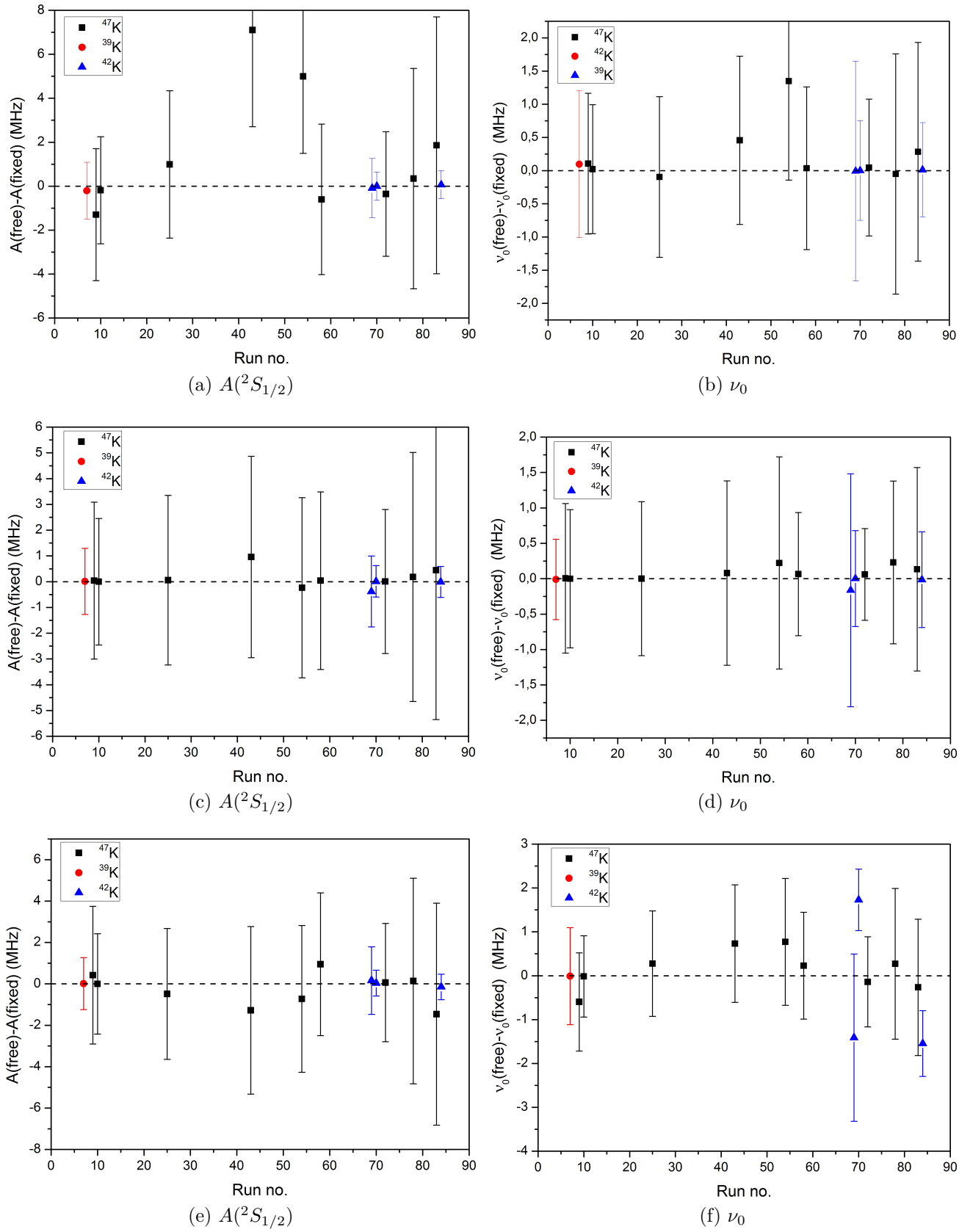

(a) $A(^2S_{1/2})$ (b) ν_0

(c) $A(^2S_{1/2})$ (d) ν_0

(e) $A(^2S_{1/2})$ (f) ν_0

FIG. IV.8: Effect on $A(^2S_{1/2})$ and the center of gravity ν_0 due to fixing fit parameters. The difference in results is shown for fixing the ratio to $\langle R \rangle = 8.278$ (a,b), for fixing the lorentzian width to the average value for the appropriate laser power (c,d) and for fixing both the lorentzian and the gaussian width (d,e).

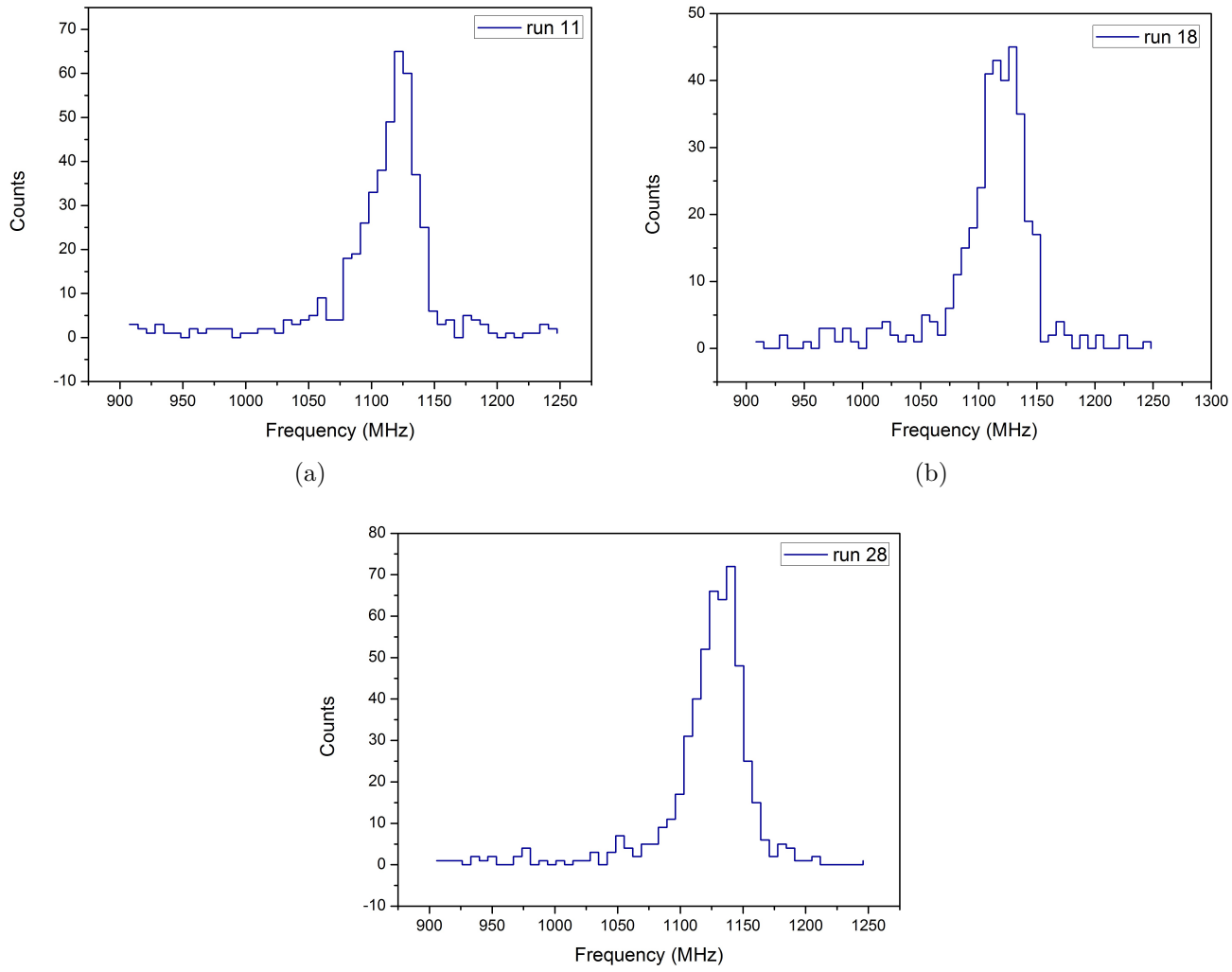

FIG. IV.9: The raw datafiles obtained for the hyperfine spectra of ^{50}K. The spectral lines show a clear asymmetric feature.

3.6 Asymmetric line profile in ^{50}K spectra

The hyperfine spectra recorded for ^{50}K ($I = 0$) show a clear asymmetric tail as can be seen in fig. IV.9. Hence, the (symmetric) voigt profile does not provide a suitable line shape. It is expected that the centroid frequency obtained in a fit with a voigt profile differs from the correct frequency. This results in an incorrect isotope shift. An estimate of the error due to the use of the improper line shape can be made by comparing the isotope shifts calculated in this work and the isotope shifts obtained in 2010. With a calculated value of 211.1(17) MHz compared to 207.5(7) MHz in 2010, the difference of 3.6 MHz is taken as the systematic error on $\delta\nu^{47,50}$.

The asymmetry has been shown to be related to collisions in the charge exchange cell [75]. Apart from resonant (ΔE) neutralization reactions, also non-resonant ($\Delta E \neq 0$) neutralization reactions can occur in the CEC. In the non-resonant case, the energy defect is taken from the

kinetic energy of the fast moving incoming ion. Hence, part of the neutralized beam moves at a slightly lower velocity. The excitations of the slower moving atoms give rise to a shoulder on the main hyperfine peak. Furthermore, the ions or atoms[6] can also lose energy in inelastic collisions without charge exchange, resulting in additional satellite peaks. The amount of peaks and the relative amplitudes of the peaks are related to the density of the vapor and the length of the CEC.
So far, this phenomenon is not understood to a satisfactory level. It is not clear why the asymmetry is only present in the spectra of ^{50}K and not in the spectra of the other isotopes, although the asymmetric contribution is expected to be more pronounced for spectra with low statistics [76].

To account for energy loss in the charge exchange cell, a quadrupole voigt line shape was developed by our COLLAPS collaborators at the Max Planck Institute for Nuclear Physics in Heidelberg [76]. The quadrupole voigt consists of one main peak with three side peaks which allows for an asymmetric line shape. For the (symmetric) hyperfine spectra recorded in the 2010 run, it was shown that results obtained with a quadrupole voigt are consistent with the values obtained with a simple voigt. It is however not believed that the physics behind the line shape is fully understood and at this moment the quadrupole voigt is interpreted merely as a complex fit function which matches the line profile.
Due to the limited time, no re-analysis of the 2011 data with the quadrupole voigt is performed in this work. It is in any case clear that the asymmetry in the spectral lines needs to be investigated further in future experiments.

3.7 Analysis of the spectra of ^{51}K

The goal of the analysis of the hyperfine spectra of ^{51}K is the determination of the ground-state spin, hyperfine coupling constant $A(^2S_{1/2})$ and isotope shift. The hyperfine spectra are normally very distinctive for different spins, in particular the relative intensities of the transitions. However due to the low resolution in the right multiplet, it is difficult to decide on the spin without a thorough investigation. Therefore, the spectra are fitted assuming three different spins i.e. $I = 1/2$, $I = 3/2$ and $I = 5/2$.

During the experiment 3 independent spectra were recorded. The first one was a scan over a broad frequency range for which the datataking took more than 15 hours. In the second spectrum, the range was adapted and the measuring time was over 20 hours. In the last run the same frequency range was scanned but the datataking had to be stopped after 10 hours as the approved beam time was finished. Even with the elongated measurement time compared to measurement times of less than an hour for the other isotopes, poor statistics were obtained, especially for the last run. Note that since the range is different in the first spectrum and the laser frequency is changed in the last spectrum, it is not possible to combine the spectra to improve the statistics.
The raw datafiles are shown in fig. IV.10. In run 33 only one multiplet is recorded while in run 82 the peaks are buried in the noise. Therefore, the focus in this analysis will be on the only remaining spectrum, spectrum 62. However, also in this file the right multiplet is badly

[6] Depending on whether the collision happens before of after the neutralization process

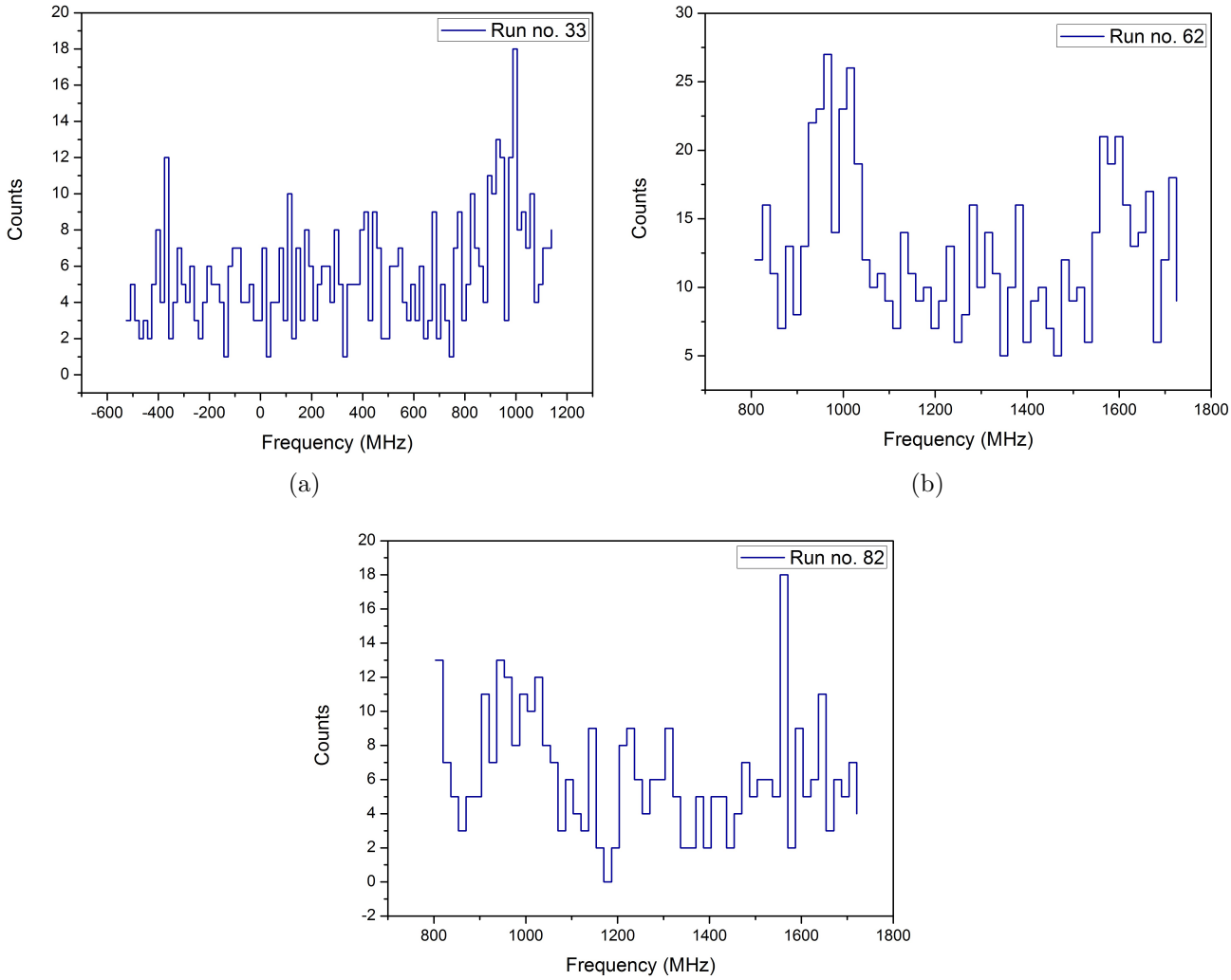

FIG. IV.10: The raw datafiles obtained for the hyperfine spectra of ^{51}K.

resolved. As discussed in the next paragraphs, this complicates the direct determination of the ground-state spin.

The range in which the structure is observed is the first indication of the spin. From the magnetic moments calculated with a SDPF-U interaction [17], the A-parameters can be obtained for different spin assumptions. Spin $I = 1/2$ is predicted to have a large coupling constant ($A(^2S_{1/2}) \approx 800$ MHz) and hence a large structure, while spin $I = 3/2$ is expected to have a more collapsed structure (($A(^2S_{1/2}) \approx 250$ MHz). Furthermore, it is possible to estimate the positions of the peaks assuming that the mean square charge radius does not change dramatically going from $A = 50$ to $A = 51$. A first inspection of the spectrum of run no. 33 corresponds to the more collapsed structure of $I = 3/2$, hence in the next run the scanning range is modified.

In the fitting procedure of ^{51}K, the number of free fit parameters is reduced compared to the fitting procedure of the other isotopes. As discussed in previous section, the ratio of the

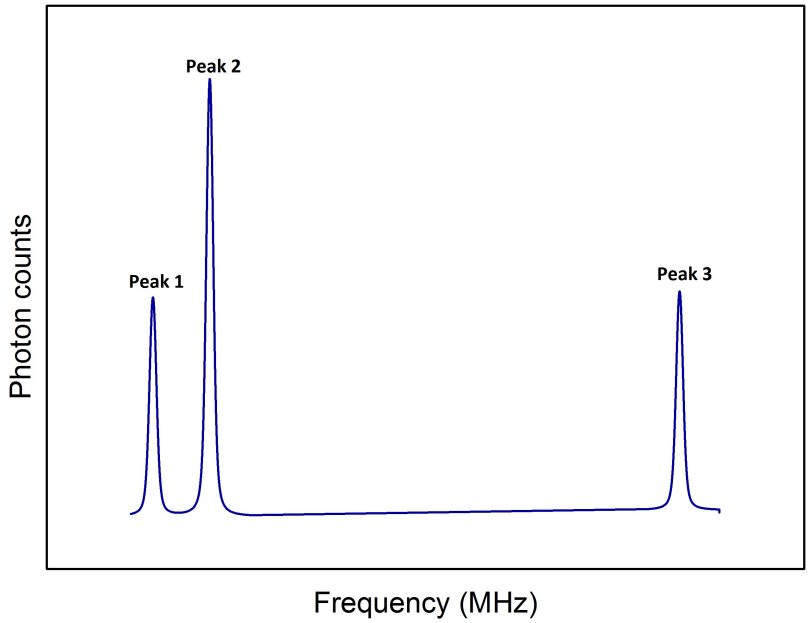

FIG. IV.11: Typical hyperfine spectrum for the $^2S_{1/2} \rightarrow {}^2P_{1/2}$ transition for an isotope with spin 1/2.

hyperfine coupling constant is constrained to $R = 8.278$ and the lorentzian width to $\Gamma = 28.6$ MHz. Additionally, the relative peak intensities have to be fixed. Since the intensities should only depend on spin (eq. III.25) and laser power, the empirical values found for ^{47}K ($I = 1/2$) and ^{39}K ($I = 3/2$) can be used. For $I = 5/2$ only theoretical values are available. Because optical pumping between the hyperfine levels is a function of laser power, only files recorded at the same laser power, i.e. 1 mW, as the ^{51}K runs are considered in the calculation of the empirical relative intensities for spin 1/2 and spin 3/2.

For spin $I = 1/2$ a typical spectrum for a laser power of 1 mW looks like fig. IV.11. It has two peaks in the left multiplet and one peak in the right multiplet. The ^{51}K spectrum has been analyzed with three different constraints on the relative intensities. In the first fit, the intensities are left as free parameters, afterwards the intensities are constrained to the relative values found for ^{47}K and finally the theoretical predicted Racah intensities (eq. III.25) are used. The experimentally found hyperfine coupling constant and isotope shift for run 62 are summarized in table IV.3. The intensities are normalized to peak 3. The difference in isotope shift for the different relative intensities is purely an effect of the center of gravity found for ^{51}K as they are compared to the same centroid value for ^{47}K.
Although the relative intensities differ considerable in the three cases, all results agree within errorbars. This can be understood because the A-parameters and centroid frequency are determined by the positions of the peaks and not by the intensities. These peak positions do not change when the relative intensities are changed, as can be seen in fig. IV.12. However, a closer look at the fitted spectra and χ^2_{red} values reveals that the fit with the relative intensities fixed to the empirical values is not so good. On the other hand, the fit where all intensities are left as free parameters gives relative intensities which do not match the predicted trend that peak 2 should be bigger than peak 3. Based on these observations, it is decided to take the results for the fit with the Racah intensities: $A(^2S_{1/2}) = 577(11)$ MHz and $\delta\nu^{51,47} = 201(5)$ MHz.

$I = 1/2$	Relative intensities	$A(^2S_{1/2})$ (MHz)	$\delta\nu^{47,51}$ (MHz)	χ^2_{red}
Free intensities	$I_1 = 1.1(4)$ $I_2 = 1.0(3)$ $I_3 = 1$	573(9)	204(5)	1.045
^{47}K intensities	$I_1 = 2.0(2)$ $I_2 = 3.3(2)$ $I_3 = 1$	576(16)	201(5)	1.246
Racah intensities	$I_1 = 1$ $I_2 = 2$ $I_3 = 1$	577(11)	201(5)	1.111

TABLE IV.3: The hyperfine coupling constants and the isotope shifts found for different assumed relative intensities for a spin $I = 1/2$ isotope.

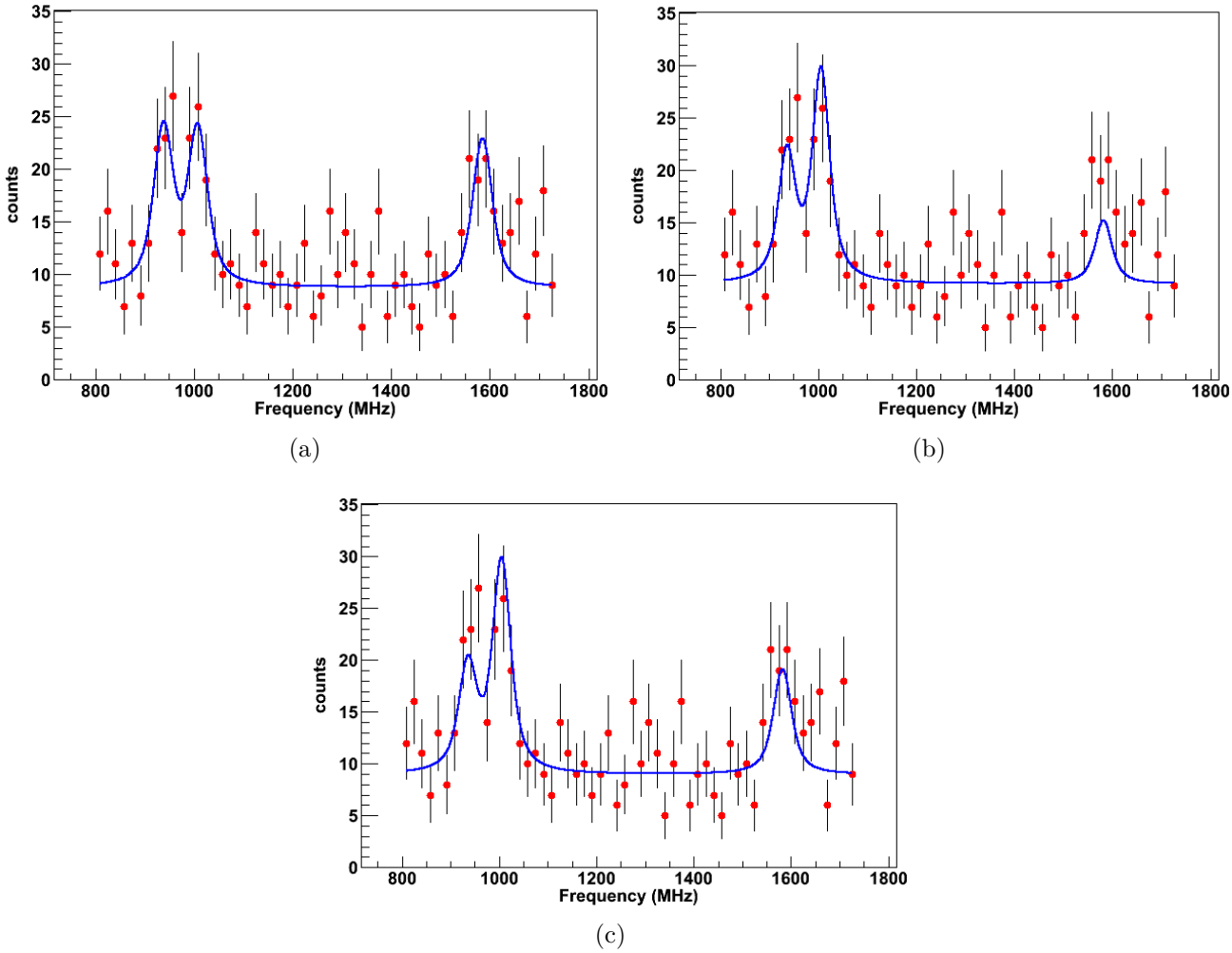

FIG. IV.12: Different fitted spectra for file no. 62 (^{51}K) with (a) no constraints on the intensities of the peak (b) the relative intensities constrained to the values found for ^{47}K and (c) the relative intensities constrained to the theoretical values.

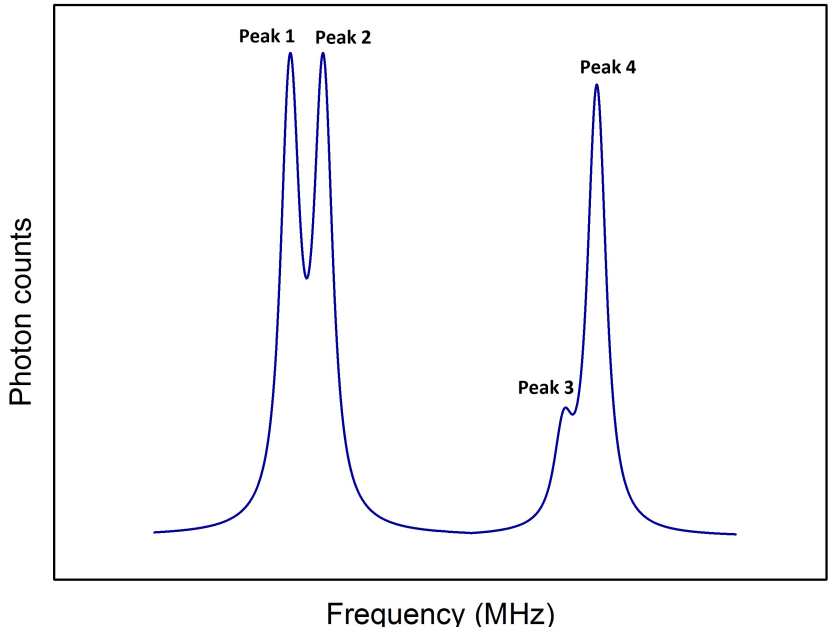

FIG. IV.13: A typical hyperfine spectrum for the $^2S_{1/2} \rightarrow {}^2P_{1/2}$ transition for an isotope with spin 3/2.

Note that within the given error bars, the other results agree with the selected value. Therefore no further systematic error has to be added to account for the uncertainty on the relative intensities.

For spin $I = 3/2$ a typical spectrum looks like fig. IV.13, with two peaks in the left multiplet and two peaks in the right multiplet. The Racah coefficients predict that the third peak should be considerably less intense than the fourth peak. This trend is indeed observed in the experimental spectra of ^{39}K in the 2010 run (laser power 0.8 mW) and the spectrum of ^{39}K in this run (laser power 2.5 mW). However, in the fit where the relative intensities are left as free parameters, the third peak is observed to be the biggest of the two as can be seen in fig. IV.15a. Clearly, this is an effect of the low statistics and should be solved by fixing the relative intensities.
Unfortunately, file no. 62 is recorded at a laser power of 1 mW and the only good file of ^{39}K is recorded at 2.5 mW. This prohibits the use of this last file in the determination of the relative intensities. There is however a ^{39}K spectrum recorded (file no. 21) with good statistics and with the correct laser power. The problem is that for this file it is impossible to get a good fit of the left multiplet[7]. The file is reanalyzed with the sole purpose of extracting the relative intensities in the right multiplet, the multiplet which poses a problem in file no. 62. For this the A-parameters are fixed to the values found in the 2010 experiment[8] $A(^2S_{1/2}) = 231.4$ MHz and $A(^2P_{1/2}) = 27.7$ MHz and the lorentzian width is fixed to the value found in this run $\Gamma = 28.6$ MHz. Although these constraints do not solve the bad fit for the left multiplet, it gives a reasonably fit for the right multiplet as can be seen in fig. IV.14.
Finally, the ^{51}K spectrum is analyzed with five different constraints on the relative intensities.

[7]This is related to a sudden jump in laser frequency.

[8]These values are in agreement with the literature values found by Touchard in 1982 [20] but have a better precision and are therefore preferred over the Touchard values.

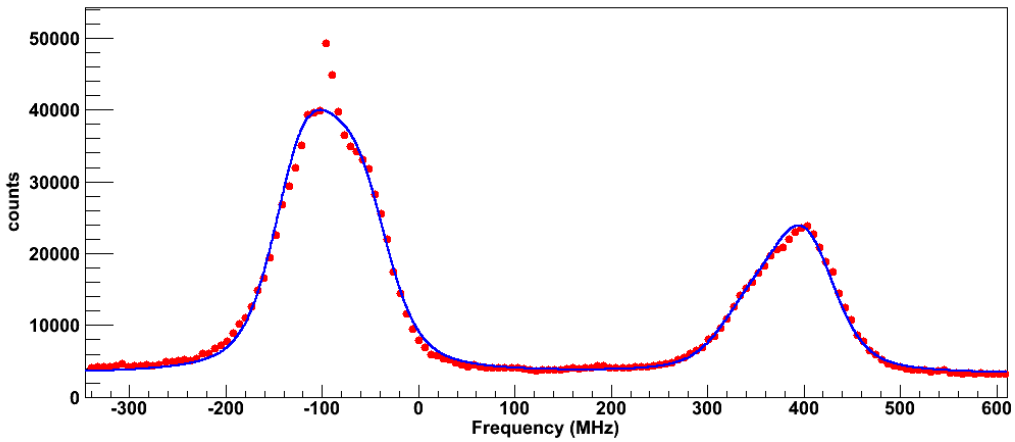

FIG. IV.14: Fitted spectrum for file no. 21 (^{39}K) with constraints on the fit parameters as discussed in the text.

In one fit the relative intensities are left as free fit parameters, in a second fit the relative intensities of the right multiplet (RM) are constrained to the values found for spectrum no. 21 for ^{39}K. For comparison the spectrum is also fitted with the theoretical predicted Racah intensities, the intensities found for a laser power of 2.5 mW in this run and the intensities found for a laser power of 0.8 mW, from the 2010 run. The results are summarized in table. IV.4 where the relative intensities are normalized to peak 1.

$I = 3/2$	Relative intensities	$A(^2S_{1/2})$ (MHz)	$\delta\nu^{47,51}$ (MHz)	χ^2_{red}
Free intensities	$I_1 = 1$ $I_2 = 0.94(34)$ $I_3 = 0.84(31)$ $I_4 = 0.30(21)$	318(5)	291(5)	1.009
^{39}K intensities: RM file no. 21	$I_1 = 1$ (free) $I_2 = 0.91(34)$ (free) $I_3 = 0.27(2)$ $I_4 = 0.64(3)$	307(16)	283(12)	1.230
Racah intensities	$I_1 = 1$ $I_2 = 1$ $I_3 = 0.2$ $I_4 = 1$	288(5)	267(5)	1.096
^{39}K intensities: laser power 0.8 mW	$I_1 = 1$ $I_2 = 0.78(2)$ $I_3 = 0.269(13)$ $I_4 = 0.77(2)$	288(8)	269(5)	1.172
^{39}K intensities: laser power 2.5 mW	$I_1 = 1$ $I_2 = 0.54(2)$ $I_3 = 0.324(14)$ $I_4 = 0.433(15)$	311(6)	290(5)	1.150

TABLE IV.4: The hyperfine coupling constants and the isotope shifts found for different assumed relative intensities for a spin $I = 3/2$ isotope.

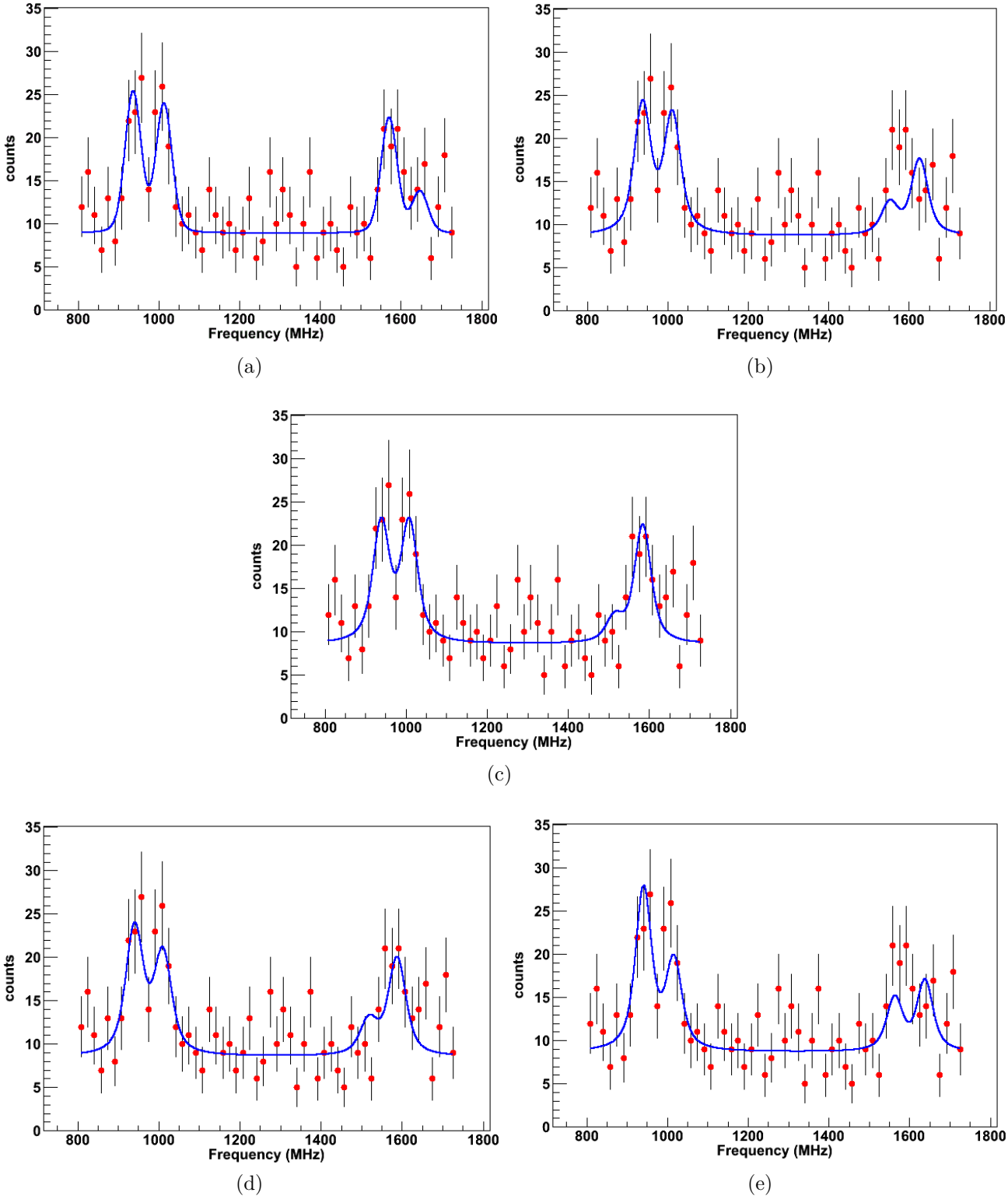

FIG. IV.15: Different fitted spectra for file no. 62 (^{51}K) with (a) no constraints on the intensities of the peak, (b) the relative intensities of the right multiplet constrained to the values found for file no. 21 (^{39}K), (c) the relative intensities constrained to the theoretical values (d) the relative intensities constrained to the values found for laser power 0.8 mW and (e) the relative intensities constrained to the values found for laser power 2.5 mW.

The results show that the relative intensities have a considerable effect on the A-parameters and the centroid frequency. This is easily understood since fixing the intensities forces the peaks of the right multiplet to different positions. This variation in peak positions is clearly visible in fig. IV.15 which shows the fits for different relative intensities.
A first remark is that the relative peak intensities in the free fit (fig. IV.15a) disagree with the theoretical predictions. This is in particular evident in the right multiplet for which it is known experimentally and theoretically that the fourth peak should be much bigger than the third peak. However, in the free fit the opposite is observed. Another remark is that the fitted spectra in fig. IV.15b and e, do not match the datapoints in the right multiplet very well.
On the other hand, the spectra analyzed with the Racah intensities (fig. IV.15c) and with the experimental 0.8mW (fig. IV.15d) intensities show visual agreement with the experimental spectrum. The reduced chi-square χ^2_{red} value for first is however much lower than for the last. Therefore the A-parameters and isotope shifts obtained with Racah intensities are taken as final result for $I = 3/2$.
Considering the large deviations between the results, it is clear that the subject of relative intensities is not fully understood. To account for this, a systematic error is included so that the value for the 1 mW intensities is covered as well. This results in a final $A(^2S_{1/2}) = 288(5)_{\text{stat}}(19)_{\text{sys}}$ MHz and $\delta\nu^{51,47} = 267(5)_{\text{stat}}(16)_{\text{sys}}$ MHz.

The hyperfine structure for a spin $I = 5/2$ isotope consists of two peaks in the left multiplet and two peaks in the right multiplet. However, there is no K-isotope measured with spin $I = 5/2$ which means it is impossible to fix the relative intensities to empirical values. The only possibility to constrain the relative intensities is by means of the theoretical Racah intensities. The results are summarized in table IV.5 where the intensities are normalized to peak 1.

$\boldsymbol{I = 5/2}$	Relative intensities	$A(^2S_{1/2})$ (MHz)	$\delta\nu^{47,51}$ (MHz)	χ^2_{red}
Free intensities	$I_1 = 1$ $I_2 = 0.94(34)$ $I_3 = 0.84(31)$ $I_4 = 0.30(21)$	212(4)	314(6)	1.086
Racah intensities	$I_1 = 1$ $I_2 = 0.8$ $I_3 = 0.285714$ $I_4 = 1$	192(5)	290(8)	1.184

TABLE IV.5: The hyperfine coupling constants and the isotope shifts found for different assumed relative intensities for a spin $I = 5/2$ isotope.

Again, a similar remark can be made about the theoretical relative intensities and the experimentally found intensities. In analogy to the two previous cases, the values obtained in the fit with the intensities fixed to the theoretical predictions are taken as final values $A(^2S_{1/2}) = 192(5)_{\text{stat}}(19)_{\text{sys}}$ MHz and $\delta\nu^{51,47} = 290(8)_{\text{stat}}(16)_{\text{sys}}$ MHz. Due to the lack of empirical intensities, the systematic errors are set equal to the $I = 3/2$ case.

Analogously to section 3.4, the systematic error on the isotope shift due to the uncertainty on the correction voltage can be determined. For all three spin assignment, the error is determined to be 0.7 MHz. This value is negligible compared to the uncertainty due to the relative intensities. Because this last error is absent for $I = 1/2$, a systematic error of 0.7 MHz is added.

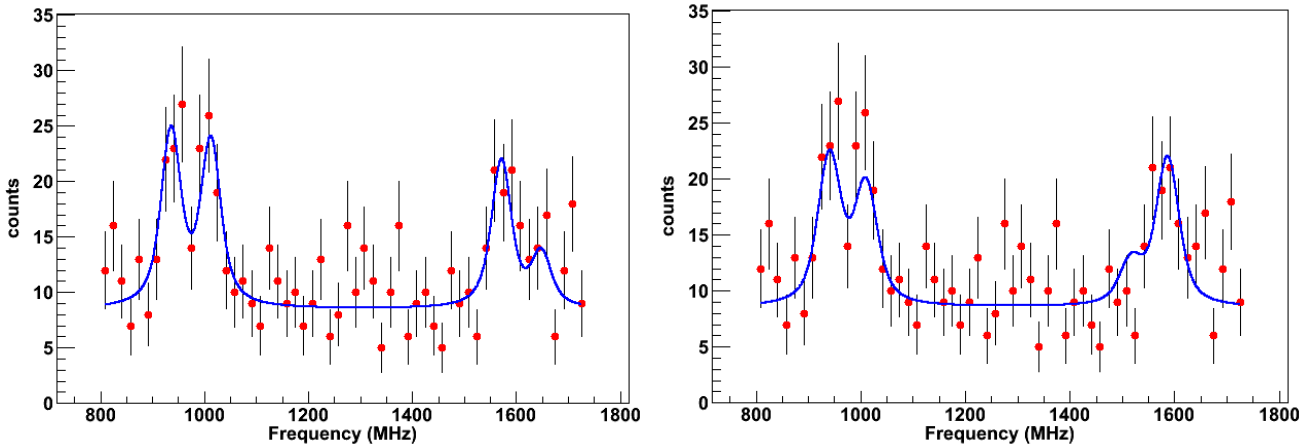

(a) (b)

FIG. IV.16: Different fitted spectra for file no. 62 (^{51}K) with (a) no constraints on the intensities of the peak and (b) the relative intensities constrained to the theoretical values.

Similarly, the additional 1.4 MHz uncertainty on $A(^2S_{1/2})$ due to the fixed ratio between hyperfine constants, only needs to be considered in the $I = 1/2$ case. Note that this last systematic error is an order of magnitude smaller than the statistical error.

Now the question arises if it is possible to assign a spin based on this analysis? With the aid of the χ^2 value, a confidence level $n\sigma$ can be calculated where n is evaluated with [53]

$$n = \sqrt{\frac{\chi^2 - \chi^2_{\text{min}}}{\chi^2_{\text{min}}/d}} \tag{IV.9}$$

In this expression, χ^2 refers to the value found in the fits from which the final A-parameters and centroid frequencies are taken, i.e. the fits with the relative intensities fixed to the Racah intensities. The minimal χ^2_{min} is reached for spin $I = 3/2$. Based on this fact, the spin is expected to be 3/2 although spin $I = 1/2$ can be discarded with a confidence level of only 0.84σ ($\approx 60\%$). For spin $I = 5/2$ it is more clear as this spin assignment can be discarded with 1.99σ ($\approx 95\%$). However a firm spin assignment will only be possible based on information on the magnetic moments and the changes in mean square charge radii.

Chapter V

Results and discussion

In the following chapter the final coupling constants and isotope shifts are presented. From these parameters the magnetic moments and changes in mean square charge radii are derived. When available, the results are compared with the values known in literature and the values calculated in the experiment of 2010. The empirical magnetic moments are discussed in the framework of shell model calculations. The mean square charge radii of the potassium isotopes are examined in the light of the observed trends in the calcium region. From the entire discussion, the spin of ^{51}K is assigned to be $I = 3/2$.

1 The hyperfine coupling constants and magnetic moments

The experimental hyperfine coupling constants for ^{39}K, ^{42}K and ^{47}K obtained in this work are summarized in table V.1 and visualized in Appendix B. The results are compared with the value found in the 2010 [28] run and the literature values. All calculated averages are within error bars in agreement with the previously known values. The $A(^2S_{1/2})$ of ^{47}K is an exception to this. While the A-values of ^{47}K measured in 2010 and 2011 are consistent within 1σ, both values disagree with the literature value. Note however that the 2010 value is an order of magnitude more precise than the previously published value.

From the A-parameters it is possible to calculate the magnetic moments if A_{ref} and μ_{ref} of a reference isotope are known (III.30)

$$\mu = \frac{AI}{A_{\mathrm{ref}} I_{\mathrm{ref}}} \mu_{\mathrm{ref}} \tag{V.1}$$

In the potassium chain the A-parameter and the magnetic moment of ^{39}K are known to high precision: $A(^2S_{1/2}) = 230.8598601(7)$ and $\mu = 0.3914662(7)$ [73]. With these reference values the magnetic moments are calculated and they are displayed in table V.1.
The magnetic moments found in this experiment agree with the results in the experiment of 2010 but show a discrepancy with the literature values for ^{42}K.

For ^{51}K it was impossible to firmly assign a spin based on the fitting alone. The hyperfine constants and magnetic moments derived from it, are therefore displayed for the three assumed

TABLE V.1: The A-parameters for the $^2S_{1/2}$ and $^2P_{1/2}$ levels obtained in this work. Results are shown for the separate spectra with the weighted mean noted in the third column. Also the magnetic moment derived from the mean $A(^2S_{1/2})$ parameter is shown. When available, the results obtained in the experiment of 2010 and the literature values are included.

		$A(^2S_{1/2})$				$A(^2P_{1/2})$				μ		
Mass no.	run no.	A (MHz)	$\langle A\rangle$ (MHz)	2010 (MHz)	Lit. (MHz)	A (MHz)	$\langle A\rangle$ (MHz)	2010 (MHz)	Lit. (MHz)	μ μ_N	2010 μ_N	Lit. μ_N
39	7	232.2(13)	232.2(13)	231.4(6)	231.0(3) [20]	27.8(7)	27.8(7)	27.7(3)	27.5(4)	0.394(2)	0.3924(10)	0.3914622(3) [73]
42	69	-503.3(13)				-61.0(13)						
	70	-504.3(6)	-504.3(4)	-504.0(2)		-60.9(6)	-60.8(4)	-61.2(2)	-60.6(16) [20]	-1.1401(7)	-1.1395(5)	-1.1425(6) [74, 77]
	84	-504.4(6)				-60.7(5)						
47	9	3415(3)				410(2)						
	10	3414(2)				412(2)						
	25	3414(3)				414(3)						
	43	3403(4)				421(2)						
	54	3412(3)	3413.5(14)	3413.2(2)	3420.2(29) [20]	420(3)	414(2)	411.9(2)	411.9(50) [20]	1.929(2)	1.92924(11)	1.933(9) [20]
	58	3420(3)				412(3)						
	72	3414(3)				412(2)						
	78	3413(5)				413(3)						
	83	3409(6)				414(2)						

TABLE V.2: Isotope shifts and charge radii obtained in this work. The results are shown for the separate files with the mean in the third column. When available, the values obtained in the experiment of 2010 and the literature values are included.

		Isotope shift				Charge radii		
A	run no. A -run no. 47	$\delta\nu^{47,A}$ (MHz)	$\langle\delta\nu^{47,A}\rangle$ (MHz)	2010 (MHz)	Lit. (MHz)	$\delta\langle r^2\rangle$ $\left(\text{fm}^2\right)$	2010 $\left(\text{fm}^2\right)$	Lit. $\left(\text{fm}^2\right)$
39	7-9	$-860.2(15)_{\text{stat}}(17)_{\text{sys}}$	$-860.2(15)_{\text{stat}}(17)_{\text{sys}}$	-859.3(7)	-857.5(17) [20]	$-0.058(7)_{\text{stat}}(15)_{\text{sys}}$	-0.066(6)	-0.081(14) [78]
42	70-58	$-505.8(14)_{\text{stat}}(10)_{\text{sys}}$	$-505.2(11)_{\text{stat}}(10)_{\text{sys}}$	-506.8(6)	-505.8(25) [20]	$0.022(10)_{\text{stat}}(9)_{\text{sys}}$	0.0352(5)	0.027(21) [78]
	84-83	$-504.4(18)_{\text{stat}}(10)_{\text{sys}}$						
50	13-10	209(2)	$211.1(17)_{\text{stat}}(36)_{\text{sys}}$	207.5(7)		$0.392(16)_{\text{stat}}(33)_{\text{sys}}$	0.426(6)	
	18-25	212.5(16)						

Spin I	$A(^2S_{1/2})$ (MHz)	μ_{exp} (μ_N)	μ_{free} (μ_N)	μ_{eff} (μ_N)
1/2	$577(11)_{\text{stat}}(1)_{\text{sys}}$	$0.326(19)_{\text{stat}}(2)_{\text{sys}}$	2.34	1.75
3/2	$288(5)_{\text{stat}}(19)_{\text{sys}}$	$0.488(8)_{\text{stat}}(32)_{\text{sys}}$	0.19	0.71
5/2	$192(5)_{\text{stat}}(19)_{\text{sys}}$	$0.543(8)_{\text{stat}}(32)_{\text{sys}}$	1.90	1.31

TABLE V.3: Hyperfine structure constant and magnetic moments for ^{51}K. The results are shown for three different spin assignments. The theoretical predictions for μ with free g factors and effective g factors are presented in the last two columns.

spins in table V.3. No experimental magnetic moments were known before this work but shell model calculations with the SPDF-U [17] interaction have been performed. The theoretical results calculated for free (bare) g-factors and for effective g-factors are shown in the last two columns. These results are discussed in section 3.

2 The isotope shifts and changes in charge radii

The isotope shift is calculated relative to ^{47}K

$$\delta\nu^{47,A} = \nu_0^A - \nu_0^{47} \tag{V.2}$$

The two centroid frequencies ν_0 are always taken from files which were recorded in a short timespan of each other to avoid influences of changing experimental conditions. If the laser frequency is changed in between two runs (which happens between file no. 71 and file no. 72), the different runs cannot be used to calculate the isotope shift.
The isotope shifts for ^{39}K, ^{42}K and ^{47}K are summarized in table V.2. The errors noted in the first brackets are the statistical errors, the systematic errors are shown in the second round brackets. For ^{39}K and ^{42}K the systematic errors arise due to the uncertainty on the ISCOOL voltage. For ^{50}K on the other hand, the uncertainty is due to the use of a symmetric line profile for an asymmetric spectrum. All calculated mean isotope shifts agree with the previously known values.

From the isotope shift it is possible to derive the change in mean square charge radius $\delta\langle r^2\rangle^{47,A}$

$$\delta\langle r^2\rangle^{47,A} = \frac{\delta\nu^{47,A} - (k_{\text{NMS}} + k_{\text{SMS}})\dfrac{M_A - M_{47}}{M_{47}M_A}}{F_e} \tag{V.3}$$

The electronic field shift constant and specific mass shift are calculated by Mårtensson-Pendrill and colleagues [78] and are found to be $F_e = -110(3)$ MHz fm^{-2} and $k_{\text{SMS}} = -15.4(38)$ GHz u. The normal mass shift constant $k_{\text{NMS}} = m_e\nu_0^{47} = m_e\,(\nu_0^{39} + \delta\nu^{47,39}) = 213554.9822(4)$ MHz u is calculated with the most recent value for the transition frequency $\nu_0^{39} = 389286058.716$ MHz [69] and the isotope shift $\delta\nu^{47,39} = -859.3(7)$ obtained from the analysis of the 2010 data. The calculated mean square charge radii in this work, shown in table V.2, agree with the previously known values.

Note that there is a large error on the mean square charge radii due to the uncertainty on the specific mass shift constant. This error is independent of the experimental details but it is mass

dependent, namely it increases from 0.045 fm^2 for ^{50}K to 0.151 fm^2 for ^{39}K[1] . Because these errors contain no information on the experiment itself and to lighten the notation, they are not included in table V.2.

For clarity, the results for ^{51}K are summarized in a different table V.4 for the three spin assumptions. No experimental values were known before this work. Note that the systematic error on the isotope shift with an assumed 1/2 spin is due to the uncertainty on the correction voltage while the systematic errors for spin 3/2 and 5/2 are due to the uncertainty of the relative intensities.

Spin I	$\delta\nu^{47,51}$ (MHz)	$\delta\langle r^2\rangle^{47,51}$ (fm^2)
1/2	$200.8(45)_{\text{stat}}(7)_{\text{sys}}$	$1.197(41)_{\text{stat}}(9)_{\text{sys}}$
3/2	$267(5)_{\text{stat}}(16)_{\text{sys}}$	$0.60(5)_{\text{stat}}(15)_{\text{sys}}$
5/2	$290(8)_{\text{stat}}(16)_{\text{sys}}$	$0.39(7)_{\text{stat}}(15)_{\text{sys}}$

TABLE V.4: Isotope shifts and changes in charge radii for ^{51}K. The results are shown for three different spin assignments assumed in the fitting procedure.

3 Magnetic moments in the shell model framework

Large scale shell model calculations were briefly introduced in the motivation of this work (section II.1). A good model should be able to predict and reproduce a large number of experimental observables such as spins and energy levels in the region of interest. To achieve this, it is important to choose an appropriate inert core and configuration space in which the valence nucleons can interact. Although a large number of interacting orbitals results in a better prediction, the number is limited due to the exponentially growing computation time [15]. The residual interaction between the valence nucleons has to be adapted to the choice of valence space. The basis inputs are the two-body matrix elements $\langle j_1 j_2|V_{\text{eff}}|j_3 j_4\rangle$ for all possible combinations of orbitals $\{j_1, j_2, j_3, j_4\}$ in the valence space and the single-particle energies. The latter are usually determined experimentally. The two-body matrix elements are calculated from the bare nucleon-nucleon interaction on which empirical corrections are applied.
In the shell model calculations for potassium, $^{16}_{8}$O$_8$ provides a proper inert core. The valence space consists of the full *sd* shell for the protons and the *sd-pf* shell for the neutrons. No excitations between the *sd* and the *pf* shell are allowed and for $N > 20$ the space is reduced to the *pf* shell. The latest interaction on this model space is the SPDF-U interaction by Nowacki [17]. The key isotopes in determining the interaction are isotopes with one particle or hole outside a doubly closed shell, namely ^{39,47}K, ^{41}Ca and ^{35}Si.
The magnetic moments are calculated according to

$$\mu = g_s^\pi s^\pi + g_s^\nu s^\nu + g_l^\pi l^\pi + g_l^\nu l^\nu \tag{V.4}$$

where $s^{\pi,\nu}$ and $l^{\pi,\nu}$ are found theoretically. The g-factors in this expression can originate from the bare nucleon-nucleon interaction (g_{free}) or can be modified for the effective interaction

[1]Because the error on the specific mass constant is multiplied by a factor $(M_A - M_{47})$, the error increase when going away from ^{47}K.

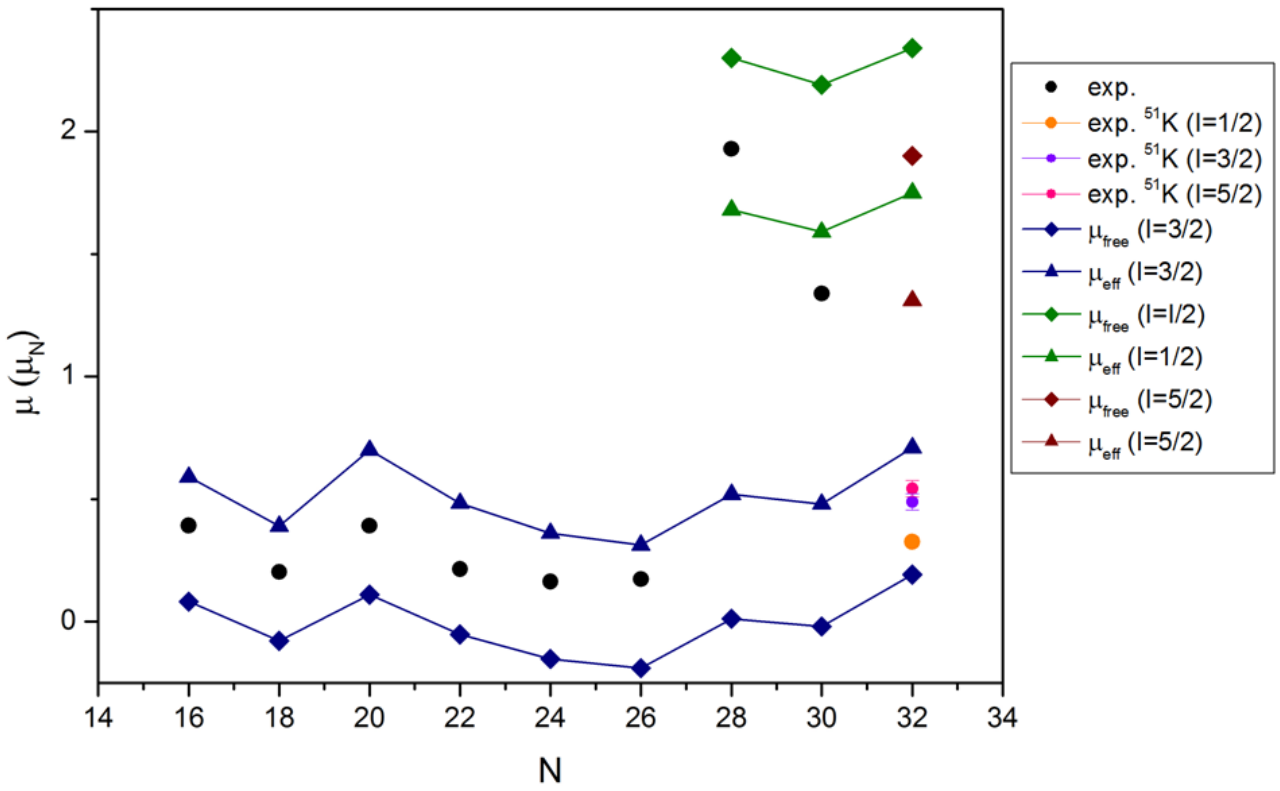

FIG. V.1: The magnetic moments for the odd K isotopes. The experimental values are taken from [79] ($N = 16$), [28] ($N = 28$ & 30), this work ($N = 32$) and [80] (all others). Except for ^{51}K, the error bars are smaller than the circles.

between the nucleons (g_{eff}). The effective g-factors used, are the standard values: $g_{s,\text{eff}} = 0.75 g_{s,\text{free}}$; $g^{\pi}_{l,\text{eff}} = 1.1$ and $g^{\nu}_{l,\text{eff}} = -0.1$.

In fig. V.1 the magnetic moments of the odd K-isotopes are shown. The experimental values are indicated with a full circle, the theoretical values are indicated with a diamond (μ_{free}) and a triangle (μ_{eff}). The calculated magnetic moments depend on the spin of the isotope, therefore allowing for a test of the assumed spin. The odd-potassium isotopes with $N \leq 26$ ($^{35-45}$K) have a $I = 3/2$ ground-state spin. The trend in the experimental magnetic moments agrees with the trend in predicted moments for this spin assumption. The next isotope (^{47}K) has a $I = 1/2$ ground-state spin and the measured magnetic moment is consistent with the calculated moment for a I=1/2 state at $N = 28$.
The observed offset of the calculated moments with respect to the measured moments is largely constant and suggests that the g-factors used in the calculations are not perfect for the K-isotopes. However, the trend along the isotope chain is reproduced accurately with the exception of ^{49}K. This is discussed in section 3.1.

The calculated occupation numbers for the $\pi s_{1/2}$ and $\pi d_{3/2}$ orbitals are shown in fig. V.2. Because there can be maximal 4 protons in the $\pi d_{3/2}$ orbit, an occupation number of around 3 indicates one proton-hole. Similarly, an occupation number of around 1 in the $\pi s_{1/2}$ orbital corresponds to a hole since the maximal occupation is 2. It is clear that up to ^{45}K ($N = 26$), the ground-state wavefunction is dominated by a hole in $\pi d_{3/2}$ while for ^{47}K ($N = 28$), there is a hole in $\pi s_{1/2}$. The results for ^{49}K and ^{51}K are discussed in the next paragraphs.

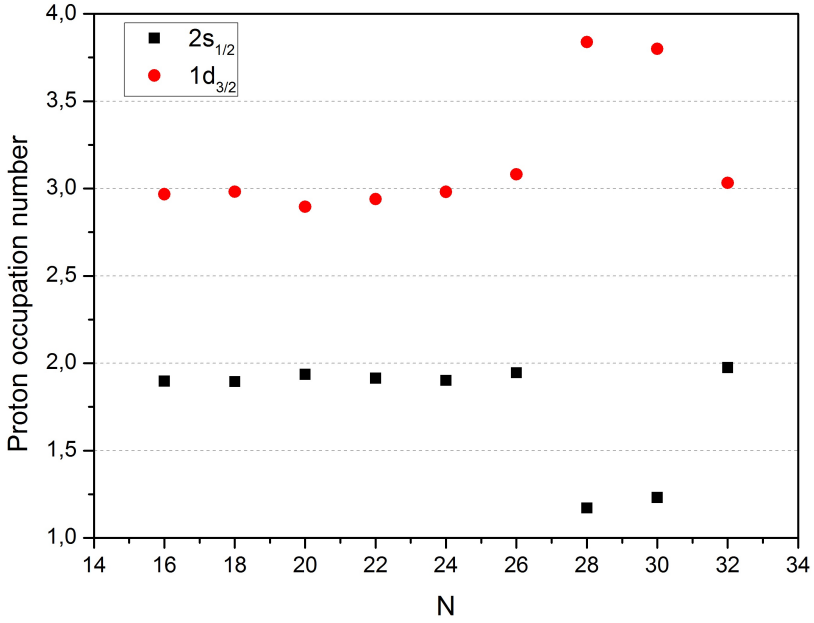

FIG. V.2: The occupation number of the $\pi s_{1/2}$ and $\pi d_{3/2}$ orbital as calculated in the shell model calculations.

3.1 The magnetic moment of ^{49}K

The spin of ^{49}K ($N = 30$) could be determined in the experiment of 2010. Similar as for $N = 28$, the spin is assigned to be $I = 1/2$ based on the fact that only 3 resonances are observed in the hyperfine spectrum [28]. This confirms the tentative assignment made based on a deep-inelastic scattering experiment [31]. The energy difference between the ground-state $E(1/2^+)$ and the first excited state $E(3/2^+)$ decreases from 359 keV for ^{47}K to 92 keV for ^{49}K [31]. Although, this near-degeneracy of the two states is predicted in shell model calculations [17] as can be seen in fig. II.4, the predicted ground-state spin is reversed.
Contrary to the isotopes with $N \leq 28$, the experimental magnetic moment at $N = 30$ ($\mu(^{49}\mathrm{K}) = 1.3388(8)\mu_N$ [28]) shows a deviation from the theoretically predicted trend in magnetic moment. This is implies that the calculated ground-state configuration (shown in fig. V.2) does not correspond to the correct configuration and additional mixing has to be taken into account. To estimate the contribution of mixing, it is in a first approximation assumed that there are two major contributions to the wavefunction

$$\left|^{49}\mathrm{K}, I = 1/2^+\right\rangle = a\left|(\pi s_{1/2}^{-1})_{1/2^+}\right\rangle + b\left|(\pi d_{3/2}^{-1})_{3/2^+} \otimes (\nu p_{3/2}^{2})_{2^+}\right\rangle \tag{V.5}$$

where $a^2 + b^2 = 1$. The magnetic moment for $|I = 1/2, M = 1/2\rangle$ is defined by eq. III.16

$$\begin{aligned}\mu(^{49}\mathrm{K}) = {} & a^2\left\langle(\pi s_{1/2}^{-1})_{1/2^+}\right|\hat{\mu}_z\left|(\pi s_{1/2}^{-1})_{1/2^+}\right\rangle \\ & + b^2\left\langle(\pi d_{3/2}^{-1})_{3/2^+} \otimes (\nu p_{3/2}^{2})_{2^+}\right|\hat{\mu}_z\left|(\pi d_{3/2}^{-1})_{3/2^+} \otimes (\nu p_{3/2}^{2})_{2^+}\right\rangle \\ & + 2ab\left\langle(\pi s_{1/2}^{-1})_{1/2^+}\right|\hat{\mu}_z\left|(\pi d_{3/2}^{-1})_{3/2^+} \otimes (\nu p_{3/2}^{2})_{2^+}\right\rangle\end{aligned} \tag{V.6}$$

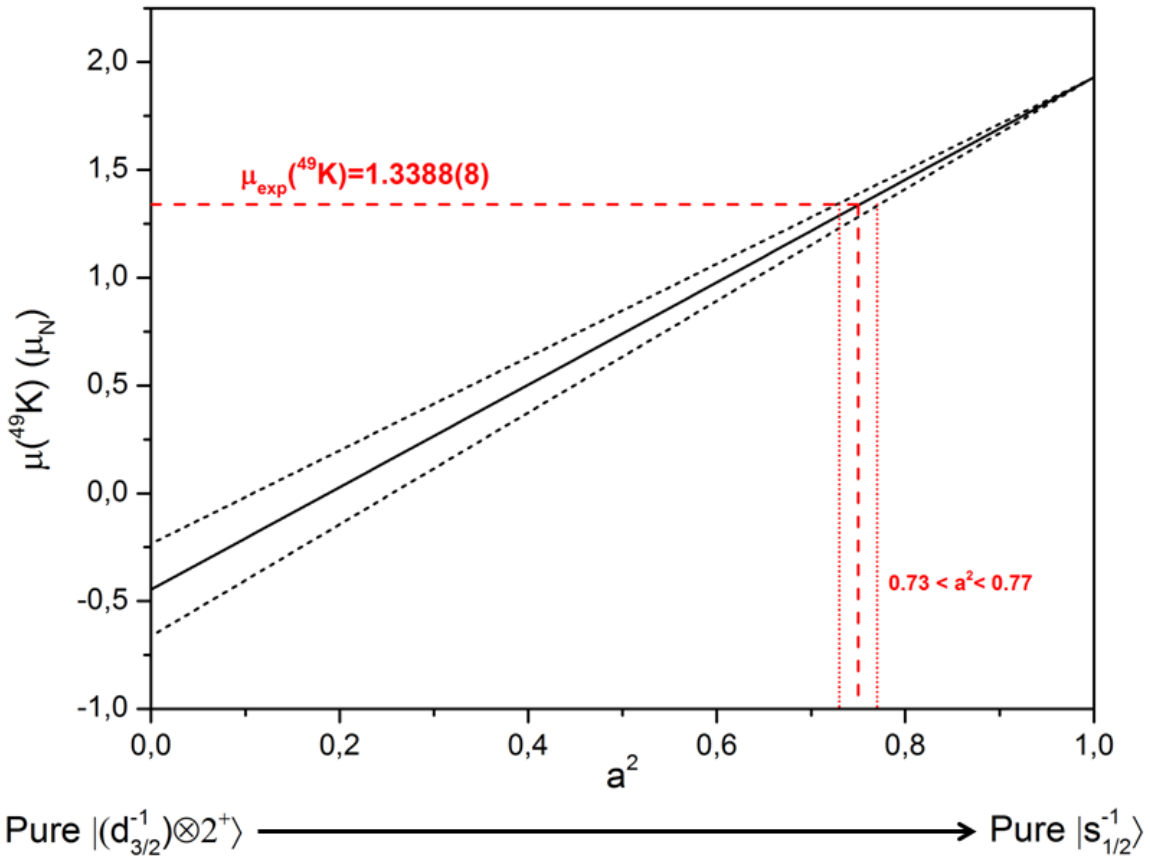

FIG. V.3: The magnetic moment given by expression V.7 in function of the value of a^2. The a^2-value which corresponds to the experimentally obtained moment of ^{49}K is indicated in red.

This complicated expression can, after some calculation (shown in appendix C), be reduced to

$$\mu(^{49}\mathrm{K}) = a^2\mu(\pi s_{1/2}^{-1}) + (1-a^2)\left[-\frac{1}{3}\mu(\pi d_{3/2}^{-1}) + \frac{1}{2}\mu\left((\nu p_{3/2}^2)_{2^+}\right)\right] \tag{V.7}$$

To be able to estimate the amount of mixing, we need reliable values for the magnetic moments in this expression.
Since the ground-state of ^{39}K is a pure $\pi d_{3/2}^{-1}$ state, its magnetic moment $\mu(^{39}\mathrm{K}) = 0.3924(10)\mu_N$ is a good estimate for $\mu(\pi d_{3/2}^{-1})$. Similarly, $\mu(^{47}\mathrm{K}) = 1.92924(11)\mu_N$ can be used to evaluate $\mu(\pi s_{1/2}^{-1})$ because of the strong $\pi s_{1/2}^{-1}$ single-particle nature of the ground-state of ^{47}K.
To obtain experimental input for $\mu\left((\nu p_{3/2}^2)_{2^+}\right)$, it is remarked that the magnetic moments of a state which consists of two unpaired nucleons in an orbital j which couple to a spin I, can be written as [50]

$$\mu((j^2)_I) = Ig(j) \tag{V.8}$$

Therefore, the neutron contribution to the magnetic moment can be written in function of the g-factor of the $\nu p_{3/2}$ orbital

$$\mu((\nu p_{3/2}^2)_{2^+}) = 2g(\nu p_{3/2}) \tag{V.9}$$

This g-factor can be deduced from the magnetic moments of states which result from one particle or hole in the $\nu p_{3/2}$ orbital, i.e. the $I = 3/2^-$ states of the $N = 29$ and $N = 31$

isotones. Experimentally, the moment is known for $^{53}_{24}Cr_{29}$ ($\mu(^{53}Cr) = -0.47454(3)\mu_N$), $^{57}_{26}Fe_{31}$ ($\mu(^{57}Fe) = -0.1549(2)\mu_N$) and $^{57}_{28}Ni_{29}$ ($\mu(^{57}Ni) = -0.7975(14)\mu_N$) [80]. It is however not known to which extend these magnetic moments are influenced by the configuration of the protons. In April 2012, the hyperfine spectra of the neutron-rich calcium isotopes were measured [81]. Because calcium has a closed proton shell, the analysis of the Ca-data will result in a more precise determination of the g-factor.

With all this information, it is possible to estimate the contribution of $\left|(\pi d^{-1}_{3/2})_{3/2^+} \otimes (\nu p^2_{3/2})_{2^+}\right\rangle$ and $\left|(\pi s^{-1}_{1/2})_{1/2^+}\right\rangle$ to the ground-state of ^{49}K. As illustrated in fig. V.3, the a^2-value corresponding to the experimentally obtained magnetic moment of ^{49}K is found to lie between 0.73 and 0.77, depending on the choice of neutron magnetic moment. Considering the large discrepancy between the measured moment and the predicted magnetic moment, this result shows less additional mixing than expected. This effect still needs to be examined further. Potential improvements could use a more complicated wave function and include a better value of $g(\nu p_{3/2})$.

3.2 The magnetic moment of ^{51}K

The experimentally found magnetic moment for ^{51}K ($N = 32$) is shown in fig. V.1 for the different spin assumptions ($I = 1/2$ in orange, $I = 3/2$ in violet and $I = 5/2$ in pink). The experimental moment for $I = 3/2$ is consistent with the theoretical predictions for this spin assignment while for spin 1/2 and 5/2 a clear discrepancy is observed. This is a good indication that the ground-state spin of ^{51}K is indeed $I = 3/2$, as predicted theoretically and experimentally [32, 33].
Furthermore, the experimental moment fits the general trend observed for the odd $I = 3/2$ isotopes ($^{35-45}$K) and corresponds to a ground-state dominated by a hole in $\pi d_{3/2}$ as can be seen on fig. V.2.

4 Mean square charge radii and magic numbers

Isotopes in the calcium region are influenced by the proton shell closure at $Z = 20$ and the neutron shell closures at $N = 20, 28$. The isotopic behavior of the mean square (ms) charge radii for Ar up to Cr ($18 \leq Z \leq 34$) is shown in fig. V.4a. Around $Z = 20$, experimental data on the ms charge radii of isotopes with less than 20 neutrons exist for Ar, K and Ca. For isotopes with more than 28 neutrons, the information is scarce as well with charge radii studied for ^{50}Ca, ^{53,54}Cr and since our recent potassium experiments, also for $^{48-51}$K.

The effect of shell gaps on ms charge radii is manifested by a characteristic change in slope at the magic neutron numbers. The difference in ms charge radius between two neighboring isotopes flattens out just below and shows a steep increase just above a shell closure, as is universally observed for $N = 28, 50, 82$ and 126 (see fig. V.4b and V.4c). However, in the calcium region this behavior is not observed for the well-known magic neutron number $N = 20$. Indeed, the ms charge radii vary smoothly across the shell gap which can be seen on fig. V.4a.

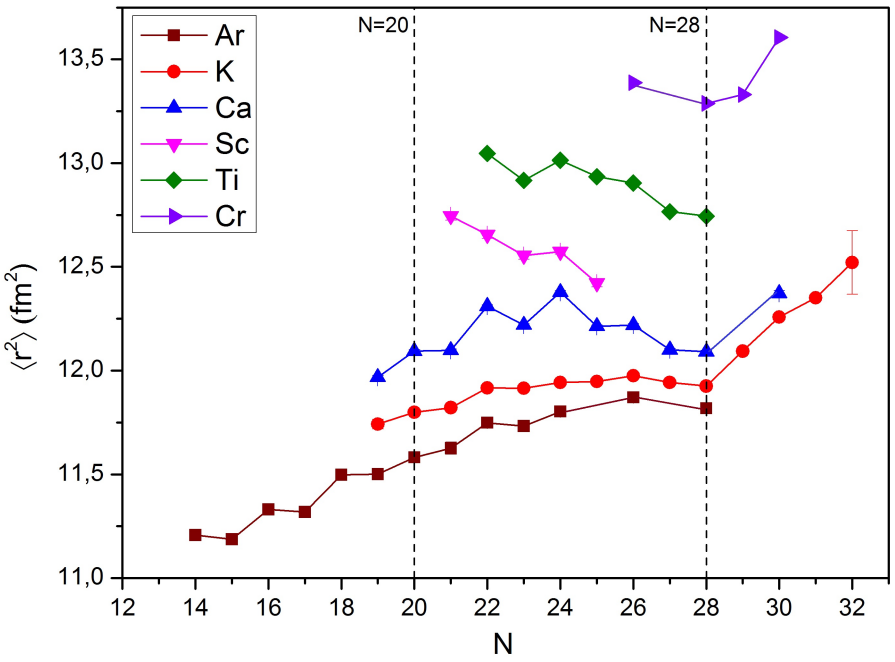

(a)

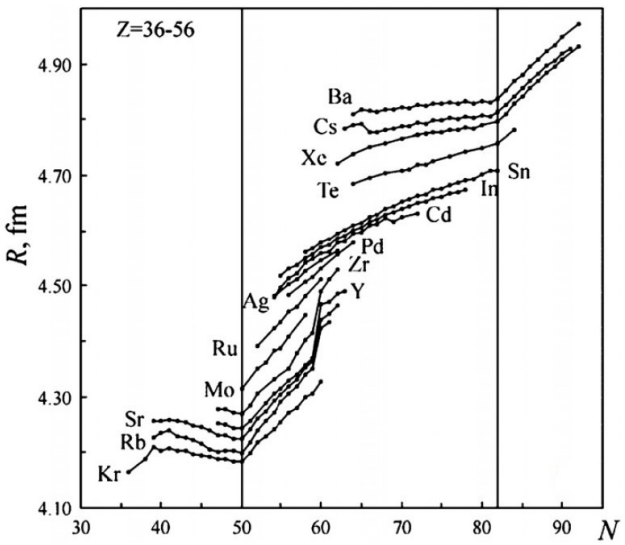

(b)

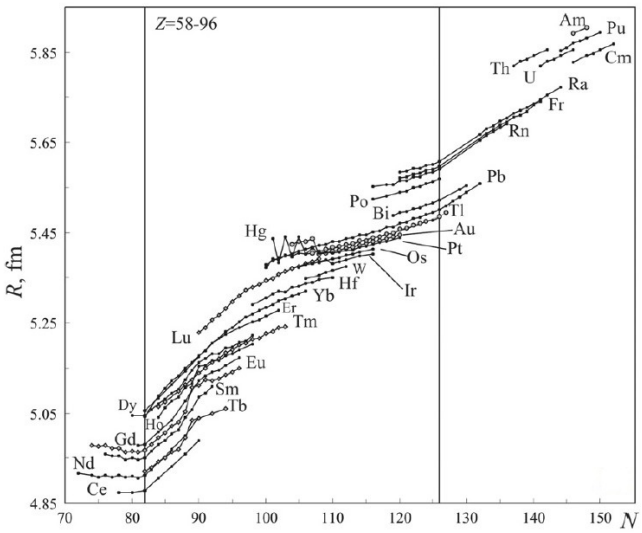

(c)

FIG. V.4: (a) The isotopic behavior of the mean square charge radii in the calcium region. The experimental results are taken from [82] and complemented with the data from [28, 83] and this work. (b, c) The root mean square charge radius $R = \langle r^2 \rangle^{1/2}$ for the isotopes in the vicinity of $N = 50, 82$ and 126. Graphs taken from [84].

This phenomenon is discussed in [45, 83, 85].

According to a paper by Klein and coworkers [45], the change in slope at a normal shell closure can microscopically be explained by core polarization effects. When valence nucleons are added to the core, the system's energy can be minimized by maximizing the overlap between the proton and the neutron wavefunctions. Since the proton-neutron interaction is attractive, a bigger overlap reduces the energy. Because the valence nucleons move on larger orbits than the core nucleons, the overlap is increased by pulling out the protons from the core. Additionally,

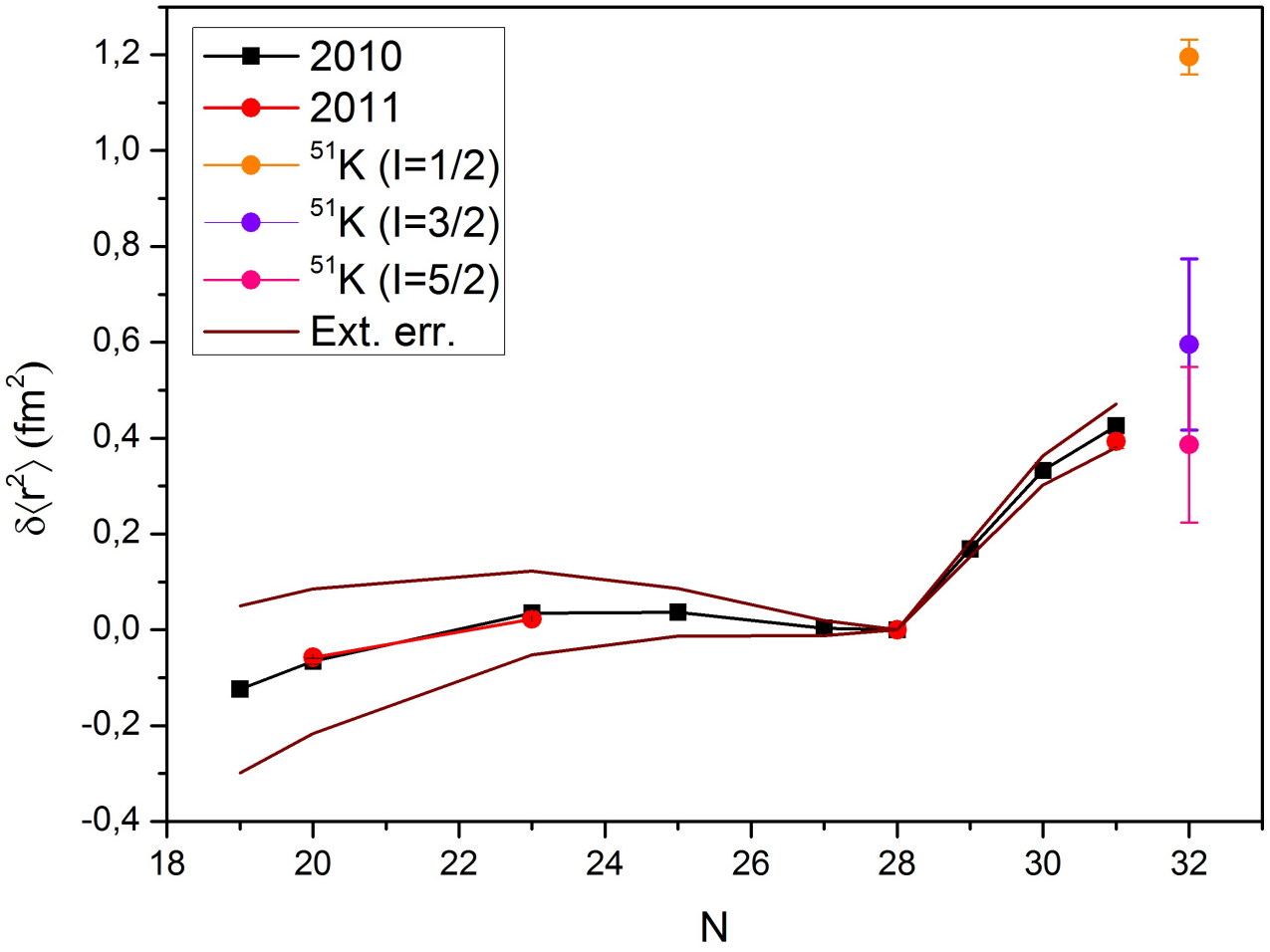

FIG. V.5: The changes in mean square charge radii for the neutron-rich potassium isotopes. The experimental values are taken from the 2010 run [28] and from this work. The experimental error bars are is most cases smaller than the bullets.

the distribution of protons is modified when neutrons are added to an orbit which has a radial node inside the nucleus. Because of the saturation property of the nuclear density, this interior node causes an expansion of the nuclear distribution in order to keep the density constant. For example, between $N = 20$ and $N = 28$ the neutrons occupy the $\nu f_{7/2}$ orbit, for which the density is located at the nuclear surface. When more than 28 neutrons are added, the $\nu p_{3/2}$ orbit which has a node inside the nuclear volume, starts to get filled. This results in an increased charge radius which is immediately evident on fig. V.4a. Apart from these two monopole core polarization mechanisms, also quadrupole core polarization has to be considered for a correct description of mean square charge radii. This second-order effect is taken into account by including a semi-empirical correction to the shape, represented by the mean square quadrupole deformation parameter $\langle\beta^2\rangle$.

It has been argumented [45] that the cancellation of the monopole and quadrupole core polarization is responsible for the absence of a visible shell effect at $N = 20$. However, why this effect is exactly observed for $N = 20$ and not for the other magic numbers, remains an open question.

The remainder of the discussion is focussed on the ms charge radii of the neutron-rich potassium isotopes, enlarged in fig. V.5. The data of 2010 (indicated in black) and 2011 (indicated in red) experiment are combined to obtain an overview over a large part of the isotopic chain. The full brown lines represent the error due to the uncertainty on the specific mass shift constant. As discussed in the previous paragraph, the magic nature of $N = 28$ is clearly visible by the flattening towards and the steep increase in ms charge radii after this neutron number. On the other hand, the ms charge radii vary smoothly when crossing the $N = 20$ shell gap.

For ^{51}K, the ms charge radii obtained for the three spin assignments are shown in orange ($I = 1/2$), violet ($I = 3/2$) and pink ($I = 5/2$). The $\delta\langle r^2\rangle^{47,51}$ value obtained for $I = 1/2$ would indicate a highly unrealistic change in ms charge radius while the results for $I = 3/2$ and $I = 5/2$ could be both consistent with the observed trend. This firmly excludes a $I = 1/2$ ground-state spin and taken into account the χ^2 analysis and the clear information from the magnetic moments, it can be concluded that the ground-state spin for ^{51}K is $I = 3/2$. This is in agreement with the theoretical predictions and with the observations in β-decay experiments [32, 33].

The differences in mean square charge radii beyond $N = 28$ show a flattening towards ^{50}K ($N = 31$). Considering the large error bars at ^{51}K, it is however impossible to draw a conclusion on the magic character of $N = 32$. A rise of the mean square radius would be possible, indicating that no shell closure is present. The possibility of a shell gap at $N = 34$ then has to be considered. Nevertheless, the lower limit of the error bar does not exclude a flattening or even a decrease in nuclear charge radius.
It is clear that the magicity of $N = 32$ for isotopes lighter than calcium still has to be investigated further. In order to see whether the shell closure persists, the error bar on the mean square charge radius of ^{51}K should be reduced. Furthermore, other observables sensitive to the magic nature of nuclei need to measured in the future.

Chapter VI

Conclusion

The ground-state spins, magnetic moments and mean square charge radii of the neutron-rich potassium isotopes ($Z = 19$) were studied via bunched-beam collinear laser spectroscopy at the COLLAPS beam-line in ISOLDE, CERN. For this purpose, a new light detection system has been designed and installed at the beam line, thereby improving the detection efficiency by more than a factor of 10. In a first experiment in 2010, the hyperfine spectra of $^{48-50}$K were successfully measured but a severe beam-contamination at mass 51 inhibited the measurement of ^{51}K. Therefore, the experiment was repeated in 2011 with an additional frequency filter in front of the photomultiplier tubes. This enabled the measurement of the hyperfine spectrum of ^{51}K. In this master thesis, the data obtained in the 2011 experiment are analyzed. The main goal of this analysis was to extract the ground-state properties of ^{51}K ($N = 32$). The magnetic moment ($\mu^{51} = 0.488(33)\ \mu_N$) and difference in mean square charge radius ($\delta\langle r^2\rangle^{47,51} = 0.60(19)$ fm^2) of ^{51}K were determined for the first time. However, the precision on these values is an order of magnitude worse than obtained for the other potassium isotopes in this experiment. The spin of the ground-state ^{51}K could be confirmed to be $I = 3/2$. These results are discussed in the framework of the evolution of shell structure in the calcium region.

For the odd potassium isotopes with $N \leq 28$, the energy difference between the $3/2^+$ ground-state (dominated by a hole in $\pi 1d_{3/2}$) and the first excited $1/2^+$ level (dominated by a hole in $\pi 2s_{1/2}$) is known to decrease when the neutron $\nu 1f_{7/2}$ orbit is filled from $N = 20$ to $N = 28$. At ^{47}K ($N = 28$), a negative energy difference indicates an inversion of the ground-state spin. This behavior is explained by a modification of the single-particle energies of the $\pi 1d_{3/2}$ and $\pi 2s_{1/2}$ proton orbits due to the tensor part of the proton-neutron interaction. This modification of single-particle energies is generally observed in isotopes with exotic proton-to-neutron ratios and causes interesting phenomena such as the inversion of ground-state spins and the (dis)appearance of magic numbers.
Before the experimental campaign on the potassium isotopes, it was not clear whether the inversion of the ground-state spin persisted beyond $N = 28$. With the results obtained in the two potassium experiments, the situation is clarified. In 2010, the ground-state spin of ^{49}K could be determined to be $I = 1/2$, indicating an inverted spin at $N = 30$. With the results on ^{51}K obtained in this work, the picture can be further complemented. Indeed, a $I = 3/2$ spin assignment for ^{51}K ($N = 32$) demonstrates the return to a normal ground-state spin.
Furthermore, information about the proton and neutron configuration can be obtained by

comparing the measured magnetic moments and the shell model calculations performed with the SPDF-U interaction. The ground-state of ^{49}K was found to be not purely characterized by a hole in $\pi s_{1/2}$ and mixing with other states has to be taken into account. On the other hand, the ground-state of ^{51}K was determined to be very single-particle like, dominated by a proton-hole in the $\pi d_{3/2}$ orbit.

Another interesting feature in the calcium region is the appearance of a new magic number at $N = 32$. This is firmly established for Cr ($Z = 24$), Ti ($Z = 22$) and Ca ($Z = 20$) for which an increased $E(2_1^+)$ value and a reduced $B(E2)$ transition probability is observed. So far, a possible shell closure at $N = 32$ is not yet investigated for isotopes with less than 20 protons. In the mean square charge radii of an isotopic chain, magic neutron numbers manifest themselves by a characteristic change in slope at a shell gap. The change in mean square charge radii relative to a reference isotope can be deduced from the isotope shift. In the potassium experiments, these isotope shifts are measured up to the suggested $N = 32$ magic number. Unfortunately, the large error bar on the mean square charge radius of $^{51}K_{32}$ does not allow for any definitive statement regarding the magic nature of $N = 32$ in the potassium isotopes. Further investigation concerning this subject is still ongoing.

Aiming at a reduction of the error bars on the magnetic moments and ms charge radii of ^{51}K, a new experiment was performed at the beginning of June 2012. Without proton-sharing and with an increased measuring time, a fully resolved hyperfine spectrum was obtained. Analysis of the data will be performed in the coming months.

Using bunched-beam collinear laser spectroscopy, it was possible to measure the hyperfine spectrum of ^{51}K for the first time. The ground-state spin, magnetic moment and mean square charge radius of ^{51}K could be determined. Since these properties are very sensitive to the nuclear structure, the evolution of single-particle energies around the $Z = 20$ shell closure could be studied.

Appendix A Hyperfine spectra

$^{39}\mathbf{K}$

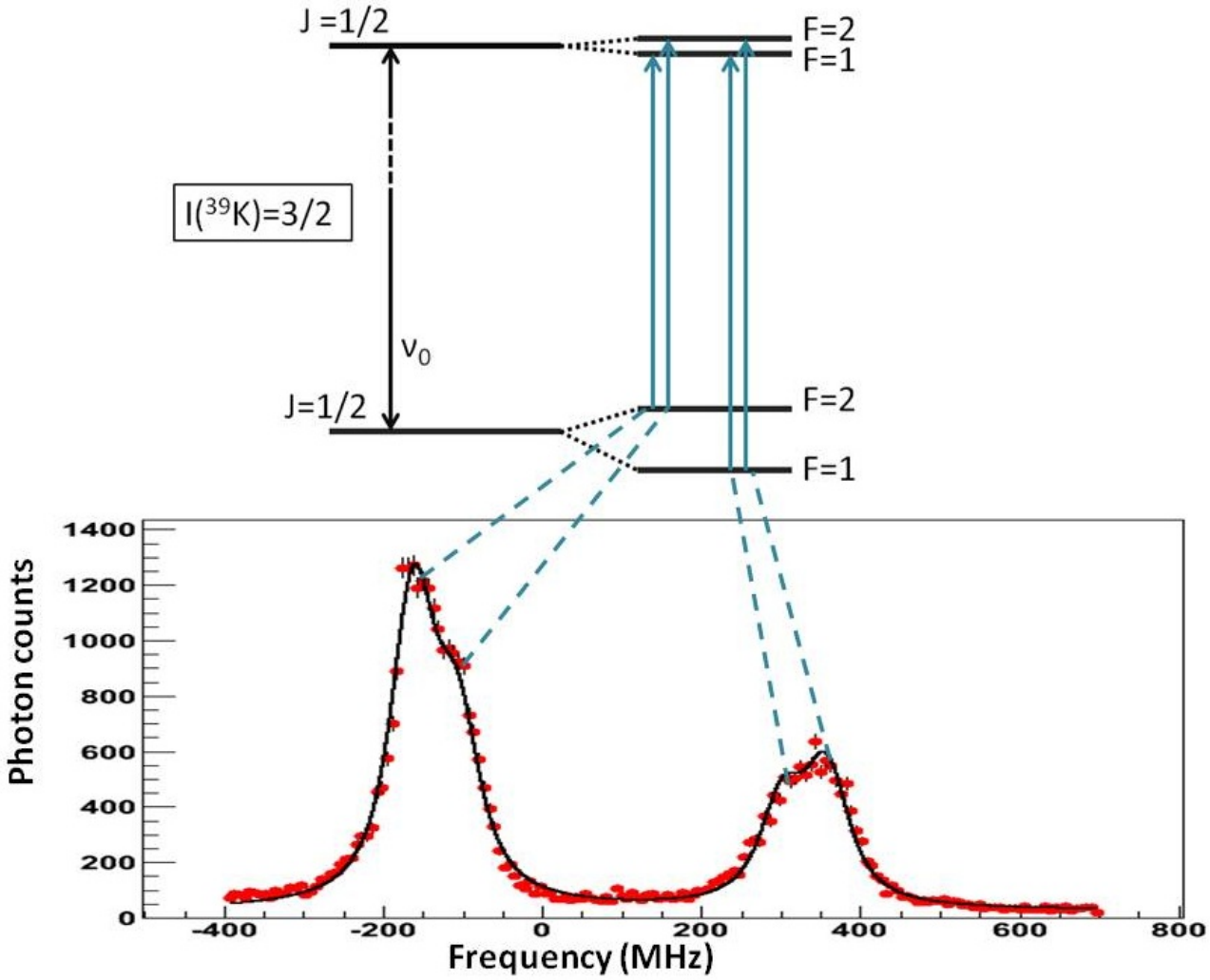

^{42}K

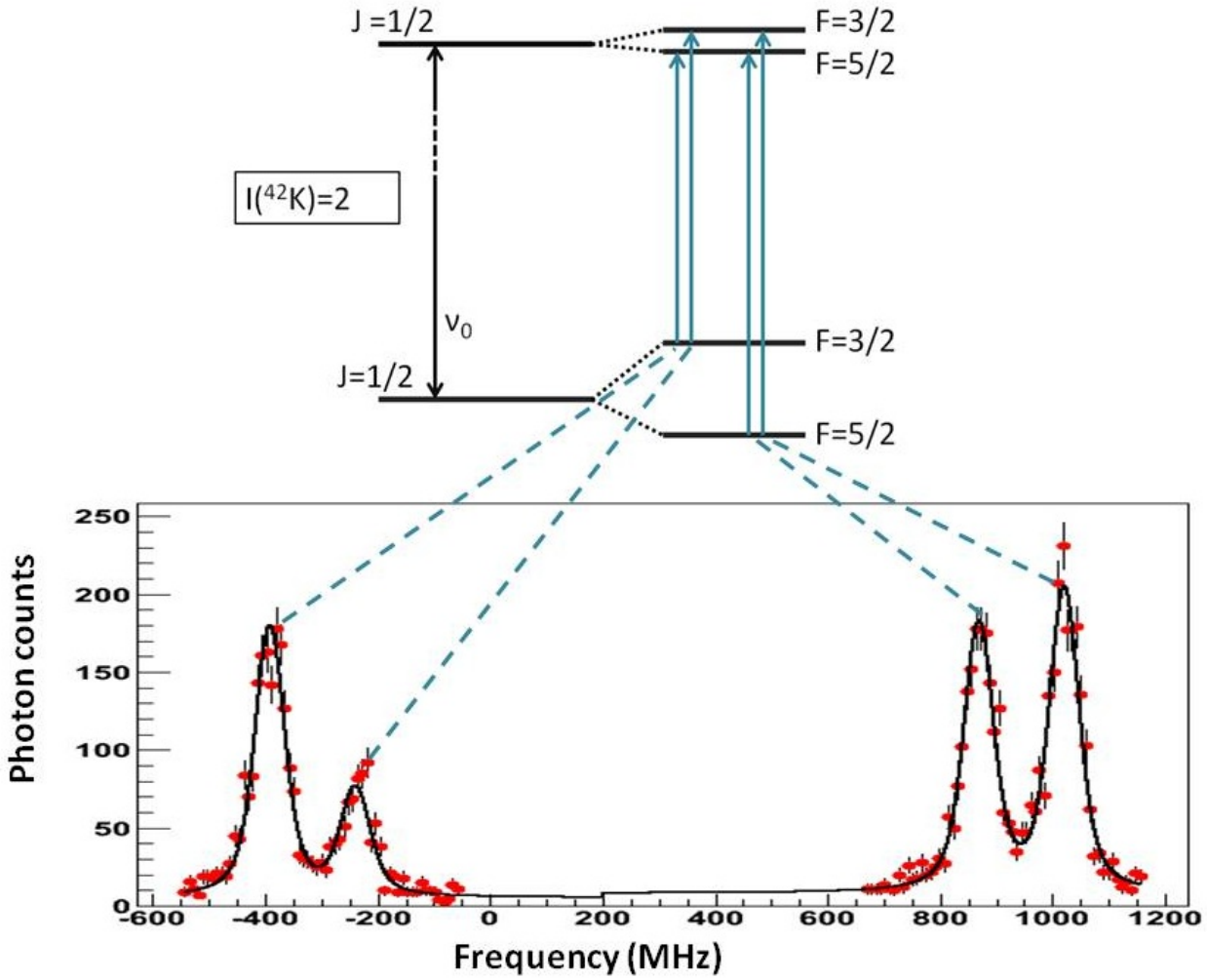

^{47}K

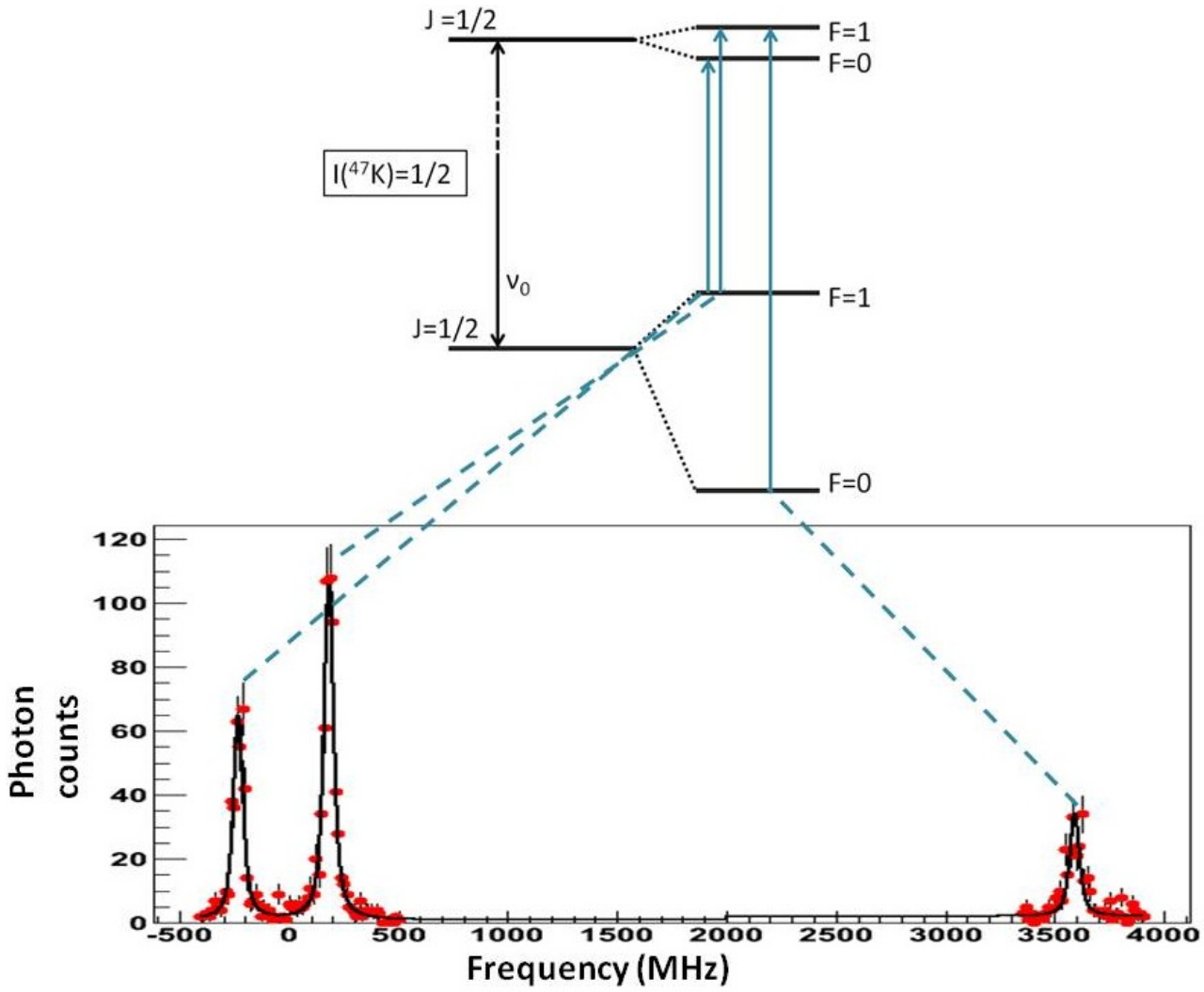

Appendix B A-parameters for ^{42}K and ^{47}K

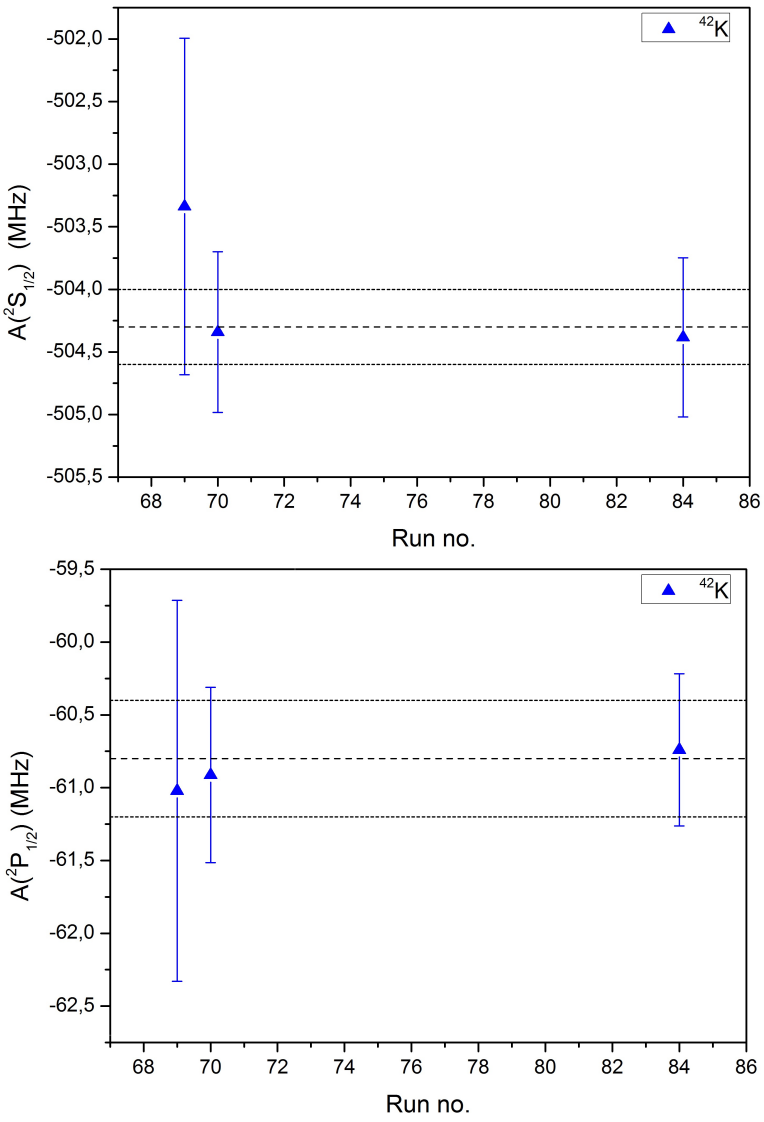

FIG. B.1: The experimental found $A(^2S_{1/2})$ (up) and $A(^2P_{1/2})$ (down) for each hyperfine spectrum of ^{42}K recorded. The dashed horizontal lines indicate the mean values with their error bars, respectively -504.3(3) MHz and -60.8(4) MHz.

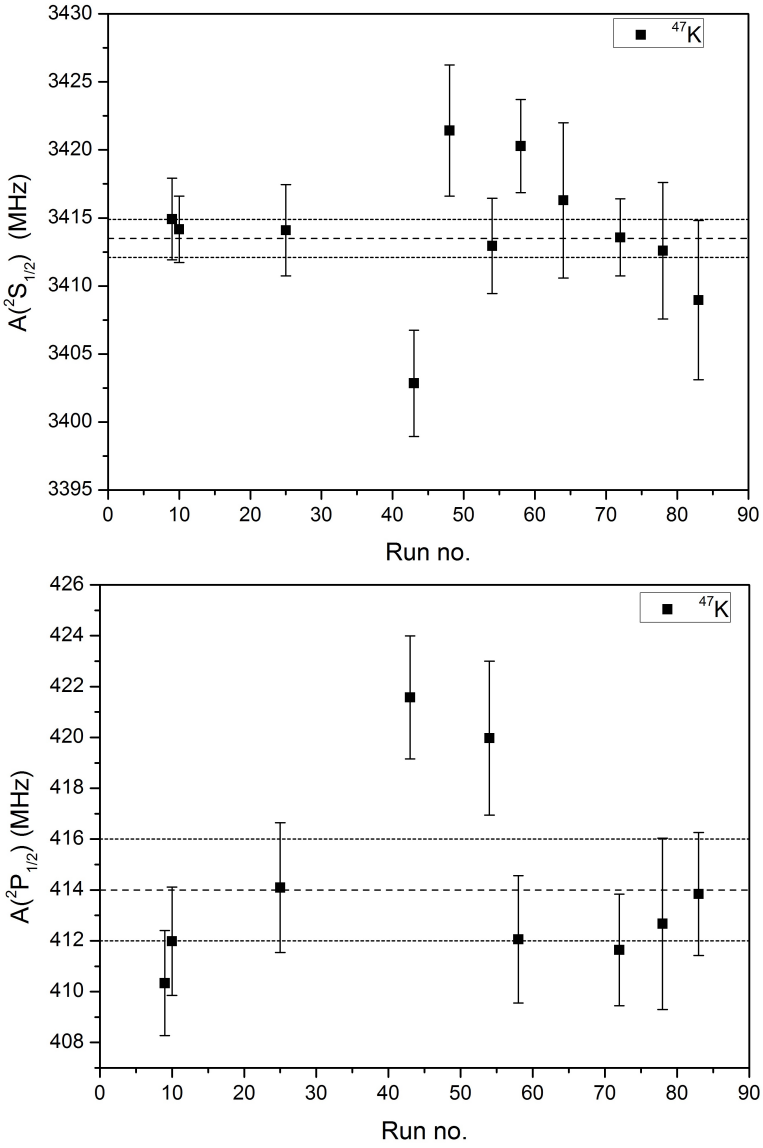

FIG. B.2: The experimental found $A(^2S_{1/2})$ (up) and $A(^2P_{1/2})$ (down) for each hyperfine spectrum of ^{47}K recorded. The dashed horizontal lines indicate the mean values with their error bars, respectively 3413.5(14) MHz and 414(2) MHz.

Appendix C The mixed ground-state of ^{49}K

The ground-state of ^{49}K with spin $I = 1/2$ is mixed. In a first approximation, we assume that there are two major contributions to the wavefunction

$$\begin{aligned} |^{49}\mathrm{K}, I = 1/2^+\rangle &= a\left|(\pi s^{-1}_{1/2})_{1/2^+}\right\rangle + b\left|(\pi d^{-1}_{3/2})_{3/2^+} \otimes (\nu p^2_{3/2})_{2^+}\right\rangle \\ &= a|1/2\rangle + b|(3/2,2);1/2\rangle \end{aligned}$$

with the condition that $a^2 + b^2 = 1$. The magnetic dipole operator is a tensor of rank 1 and thus $\hat{\mu}_z = \hat{\mu}^1_0$. The experimental magnetic moment can according to eq. III.16 be written as

$$\mu(I) = \langle IM = I|\hat{\mu}^1_0|IM = I\rangle \tag{C.1}$$

For the ground-state of ^{49}K this means that

$$\begin{aligned} \mu(^{49}\mathrm{K}) = a^2&\langle 1/2|\hat{\mu}^1_0|1/2\rangle \\ &+ b^2\langle (3/2,2);1/2|\hat{\mu}^1_0|(3/2,2);1/2\rangle \\ &+ 2ab\langle 1/2|\hat{\mu}^1_0|(3/2,2);1/2\rangle \end{aligned} \tag{C.2}$$

We will look at this long expression term by term and show that we can reduce it to a much simpler form.

- $\underline{\langle \mathbf{1/2}|\hat{\boldsymbol{\mu}}^{\mathbf{1}}_{\mathbf{0}}|\mathbf{1/2}\rangle}$

  This term is just the single-particle moment of a pure $\pi 2s^{-1}_{1/2}$ state.

- $\underline{\langle \mathbf{(3/2,2);1/2}|\hat{\boldsymbol{\mu}}^{\mathbf{1}}_{\mathbf{0}}|\mathbf{(3/2,2);1/2}\rangle}$

  Due to the additivity rule [49], the magnetic moment can be decomposed in a proton and a neutron part

  $$\hat{\mu}^1_0 = \hat{\mu}^1_0(\pi) + \hat{\mu}^1_0(\nu) \tag{C.3}$$

  Therefore, the magnetic moment of a state with spin I, described by a configuration consisting of protons coupled to spin I_π and neutrons coupled to spin I_ν can be written as

  $$\mu(I) = \langle (I_\pi, I_\nu); IM = I|\hat{\mu}^1_0(\pi)|(I_\pi, I_\nu); IM = I\rangle + \langle (I_\pi, I_\nu); IM = I|\hat{\mu}^1_0(\nu)|(I_\pi, I_\nu); IM = I\rangle \tag{C.4}$$

This expression can be decomposed in single-particle moments by the use of the Wigner-Eckhart (W.E.) theorem and the tensor reduction rules (RR) [50]. We illustrate this for protons, the case for neutron is very similar

$$\begin{aligned}
\mu(\pi) = &\ \langle (I_\pi, I_\nu); IM = I|\hat{\mu}^1_0(\pi)|(I_\pi, I_\nu); IM = I\rangle \\
&\overset{\text{W.E.}}{=} \begin{pmatrix} I & 1 & I \\ -I & 0 & I \end{pmatrix} \langle (I_\pi, I_\nu); I||\hat{\mu}^1_0(\pi)||(I_\pi, I_\nu); I\rangle \\
&\overset{\text{RR}}{=} (-1)^{I_\pi+I_\nu+I+1}(2I+1) \begin{pmatrix} I & 1 & I \\ -I & 0 & I \end{pmatrix} \begin{Bmatrix} I & I_\pi & I_\nu \\ I_\pi & I & 1 \end{Bmatrix} \delta_{I_\nu,I_\nu} \langle I_\pi||\hat{\mu}^1_0(\pi)||I_\pi\rangle \\
&\overset{\text{W.E.}}{=} (-1)^{I_\pi+I_\nu+I+1}(2I+1) \frac{\begin{pmatrix} I & 1 & I \\ -I & 0 & I \end{pmatrix}}{\begin{pmatrix} I_\pi & 1 & I_\pi \\ -I_\pi & 0 & I_\pi \end{pmatrix}} \begin{Bmatrix} I & I_\pi & I_\nu \\ I_\pi & I & 1 \end{Bmatrix} \langle I_\pi\ M_\pi = I_\pi|\hat{\mu}^1_0(\pi)|I_\pi\ M_\pi = I_\pi\rangle
\end{aligned}$$

Here $\langle (I_\pi, I_\nu); I||\hat{\mu}^1_0(\pi)||(I_\pi, I_\nu); I\rangle$ is the reduced matrix element which is independent form the spin projection M. The symbols between round brackets are called the Wigner $3j$ symbols, the symbols in curly brackets are the Wigner $6j$ symbols. These arise when angular momenta are coupled in quantum mechanics and are related to the Clebsch-Gordan coefficients. The total expression for protons and neutrons becomes

$$\begin{aligned}
\mu(I) = &(-1)^{I_\pi+I_\nu+I+1}(2I+1) \begin{pmatrix} I & 1 & I \\ -I & 0 & I \end{pmatrix} \\
&\times \left[\begin{Bmatrix} I & I_\pi & I_\nu \\ I_\pi & I & 1 \end{Bmatrix} \frac{\mu(I_\pi)}{\begin{pmatrix} I_\pi & 1 & I_\pi \\ -I_\pi & 0 & I_\pi \end{pmatrix}} + \begin{Bmatrix} I_\pi & I_\nu & I \\ 1 & I & I_\nu \end{Bmatrix} \frac{\mu(I_\nu)}{\begin{pmatrix} I_\nu & 1 & I_\nu \\ -I_\nu & 0 & I_\nu \end{pmatrix}} \right]
\end{aligned}$$

In the specific case we are dealing with, we get

$$\mu(1/2) = -\frac{1}{3}\mu(\pi 3/2) + \frac{1}{2}\mu(\nu 2^+)$$

- **Cross-term**
  The last matrixelement can be decomposed in the same way as we did for the b^2-term. However, the tensor reduction rule will in this case lead to two delta functions, δ_{I_ν,I'_ν} in the proton term and δ_{I_π,I'_π} in the neutron term. Considering $I_\pi = 1/2, I'_\pi = 3/2, I_\nu = 0$ and $I'_\nu = 2$, the delta functions are zero which results in the vanishing of the cross term.

Combining the two remaining terms, the long expression is reduced to

$$\mu(^{49}\text{K}) = a^2\mu(1/2) + (1-a^2)\left[-\frac{1}{3}\mu(3/2) + \frac{1}{2}\mu(2^+)\right]$$

Bibliography

[1] R.V. F. Janssens, *Unexpected doubly magic nucleus*, Nature 459, 1069-1070, (2009)

[2] W. Schwerdtfeger et al., *Shape coexistence near neutron number $N = 20$: first identification of the $E0$ decay from the deformed first excited $J\pi = 0^+$ state in ^{30}Mg*, Phys. Rev. Let. 103, 012501, (2009)

[3] P. Doornenbal et al., *Spectroscopy of ^{32}Ne and the "Island of Inversion"*, Phys. Rev. Let. 103, 032501, (2009)

[4] R. Kanungo, *Structure of ^{33}Mg sheds new light on the $N = 20$ island of inversion*, Phys. Let. B 685, 235-257, (2010)

[5] O. Sorlin et al., *Decay properties of exotic $N \simeq 28$ S and Cl nuclei and the $^{48}Ca/^{46}Ca$ abundance ratio*, Phys. Rev. C 47, 2941-2953, (1993)

[6] O. Sorlin et al., *Beta-Decay Studies of Far From Stability Nuclei near $N = 28$*, Nucl. Phys. A583, 763-768, (2008)

[7] S. Grévy et al., *Beta-decay half-lives at the $N = 28$ shell closure*, Phys. Let. B 594, 252-259, (2004)

[8] O. Sorlin and M.-G. Porquet, *Nuclear magic numbers: New features far from stability*, Progress in Part. and Nucl. Phys. 61, 602-673, (2008)

[9] R. Krücken, *Introduction ot shell structure in exotic nuclei*, Cont. Phys. 52, 101-120, (2011)

[10] T. Otsuka et al., *Magic numbers in exotic nuclei and spin-isospin properties of NN interaction*, Phys. Rev. Let. 87, 082502, (2001)

[11] T. Otsuka et al., *Evolution of nuclear shells due to the tensor force*, Phys. Rev. Let. 95, 232502, (2005)

[12] T. Otsuka, T. Matsuo and D. Abe, *Mean field with tensor force and shell structure of exotic nuclei*, Phys. Rev. Let. 97, 162501, (2006)

[13] M. Bender, P.-H. Heenen and P.-G. Reinhard, *Self-consistent mean-field models for nuclear structure*, Rev. of Mod. Phys. 75, (2003)

[14] J.R. Stone and P.-G. Reinhard, *The Skyrme interaction in finite nuclei and nuclear matter*, Progress in Part. and Nucl. Phys 58, 587-657, (2007)

[15] B. A. Brown, *The Nuclear Shell Model Towards the Drip Lines*, Progress in Part. and Nucl. Phys. 47, 517, (2001)

[16] H. Grawe, *Shell Model from a Practitioner Point of View*, Lect. Notes Phys. 651, 33-75, (2004)

[17] F. Nowacki and A. Poves, *New effective interaction for* $0\hbar\omega$ *shell-model calculations in the* $sd-pf$ *valence space*, Phys. Rev. C. 79, 014310, (2009)

[18] S. Nummela et al., *Spectroscopy of* $^{34,35}Si$ *by* β *decay: sd-fp shell gap and single-particle states* Phys. Rev. C 63, 044316, (2001)

[19] J. Retamosa et al., *Shell model study of the neutron-rich nuclei around* $N = 28$, Phys. Rev. C 55, 1266, (1997)

[20] F. Touchard et al., *Isotope shifts and hyperfine structure of* $^{38-47}K$ *by laser spectroscopy*, Physics Letters, Volume 108B, number 3, (1982)

[21] P. Doll, G.J. Wagner, K.T. Knöpfle, *The quasihole aspect of hole strength distributions in odd potassium and calcium isotopes*, Nucl. Phys. A 263, 210-236, (1976)

[22] S.M. Banks et al., *The* $^{48}Ca(d,^3He)^{47}K$ *reaction at 80 MeV*, Nucl. Phys. A 437, 381-396, (1985)

[23] B. Singh and J.A. Cameron, Nucl. Data Sheets 107, 225, (2006)

[24] J.A. Cameron and B. Singh, Nucl. Data Sheets 94, 429, (2001)

[25] J.A. Cameron and B. Singh, Nucl. Data Sheets 92, 783, (2001)

[26] T.W. Burrows, Nucl. Data Sheets 109, 171, (2008)

[27] T.W. Burrows, Nucl. Data Sheets 108, 923 (2007)

[28] J. Papuga, *Results from the 2010 potassium experiment* Private communication Februari 2012

[29] M. Grasso et al., *Evolution of the proton sd states in neutron-rich Ca isotopes*, Phys. Rev. C 76, 044319, (2007)

[30] L.C. Carraz et al., *The* ^{49}K *beta decay*, Phys. Let. 109B, 6, (1982)

[31] R. Broda et al., *Proton-hole state in the* $N = 30$ *neutron-rich isotope* ^{49}K, Phys. Rev. C 82, 034319, (2010)

[32] F. Perrot et al., β*-decay studies of neutron-rich K isotopes*, Phys. Rev. C 74, 014313, (2006)

[33] B. Fornal et al., *Yrast structure of the neutron-rich* $N = 31$ *isotones* ^{51}Ca *and* ^{52}Sc Phys. Rev. C 77, 014304, (2008)

[34] A. Huck et al., *Beta decay of new isotopes* ^{52}K, ^{52}Ca *and* ^{52}Sc*; a test of the shell model far from stability*, Phys. Rev. C 31, 2226-2237, (1985)

[35] R.V. F. Janssens et al., *Structure of ^{52,54}Ti and shell-closures in neutron-rich nuclei above ^{48}Ca*, Phys. Let. B 546, 55-62, (2002)

[36] J.J. Prisciandaro et al., *New evidence for a subshell gap at $N = 32$*, Phys. Let. B 510, 17-23, (2001)

[37] D.C. Dinca, *Reduced transition probabilities to the first 2^+ state in ^{52,54,56}Ti and development of shell closures at $N = 32, 34$*, Phys. Rev. C 71, 041302(R), (2005)

[38] A. Bürger et al., *Relativistic Coulomb excitation of neutron-rich ^{54,56,58}Cr: On the pathway of magicity from $N = 40$ to $N = 32$*, Phys. Let. B 622, 29-34, (2005)

[39] S.N. Liddick et al., *Development of shell closures at $N = 32, 34$: β decay of neutron-rich Sc isotopes*, Phys. Rev. C, 064303, (2004)

[40] M. Homna et al., *Effective interaction for pf-shell nuclei*, Phys. Rev. C 65, 061301(R), (2002)

[41] M. Homna et al., *Shell-model description of neutron-rich pf-shell nuclei with a new effective interaction GXPF1*, Eur. Phys. J. A 25, 499, (2005)

[42] P. Maierbeck et al., *Structure of ^{55}Ti from relativistic one-neutron knockout*, Phys. Let. B 675, 22-27, (2009)

[43] W.H. King, *Isotope Shifts in Atomic Spectra*, Plenum Press, (1984)

[44] E.C. Seltzer, *K X-ray isotope shifts*, Physical Review A 188, (1969)

[45] A. Klein et al., *Moments and mean square charge radii of short-lived argon isotopes*, Nucl. Phys. A 607, 1-22, (2008)

[46] D. Griffiths, *Introduction to electrodynamics*, Prentice Hall, (1998)

[47] K. Krane, *Introductory Nuclear Physics*, Wiley, (1988)

[48] B. Castel and I.S. Towner, *Modern Theories of Nuclear Moments*, Clarendon Press, (1990)

[49] G. Neyens, *Exotic nuclei: Properties and interactions- Part B*, Lecture notes, K.U. Leuven, (2011-2012)

[50] K. Heyde, *The Nuclear Shell Model*, Springer-Verlag, (1990)

[51] J. Papuga *Laser spectroscopy of neutron-deficient odd-mass Cu isotope*, Predoctoral Thesis, Instituut voor Kern- en Stralingsfysica, K.U. Leuven, (2011)

[52] P.C. Magnane and H.H. Stroke, *Isotope Shift between^{209}Bi and 6.3-day ^{206}B*, J. Opt. Soc. Am. 59 7, (1969)

[53] E. B. Mané, *High resolution laser spectroscopy of radioactive isotopes using a RFQ cooler-buncher at Cern-ISOLDE*, PhD thesis, University of Manchester, (2009)

[54] J. R. Persson, *Table of hyperfine anomaly in atomic systems*, arXiv:1110.5991v1

[55] B.H. Bransden and C.J. Joachain, *Physics of atoms and molecules*, Prentice Hall, (1986)

[56] H. Kopfermann, *Nuclear Moments*, Academic Press Inc., (1958)

[57] R. Neugart and G. Neyens, *Nuclear moments*, Lect. Notes Phys. 700, 135-189, (2006)

[58] X. Huang and Y. Yung, *A Common Misunderstanding about the Voigt Line Profile*, Journal of the Atmospheric Sciences 61, (2004)

[59] M.L. Bissell et al., *IS484: Ground-state properties of K-isotopes from laser and β-NMR spectroscopy*, Proposal to the INTC committee, CERN, (2009)

[60] M.L. Bissell et al., *IS484: Ground-state properties of K-isotopes from laser and β-NMR spectroscopy*, Addendum to the INTC committe, CERN, (2011)

[61] P. Baumann et al., *Meson-exchange enhancement in first-forbidden β-transitions: The case of ^{50}K and ^{38}Ca*, Phys. Rev. C58, 1970, (1998)

[62] H.L. Crawford et al., *β-decay studies of neutron-rich nuclei near ^{52}Ca*, Acta Physica Polonica B 40, (2009)

[63] Chart of nuclides, National Nuclear Data Center, Brookhaven National Laboratory, `http://www.nndc.bnl.gov/`

[64] G. Audi and M. Wang, Private Communication April 2011

[65] The ISOLDE facility website, `http://isolde.web.cern.ch/isolde/`

[66] E. B. Mané, *An ion cooler-buncher for high-sensitivity collinear laser spectroscopy at ISOLDE*, Eur. Phys. J. A 42, 503-507, (2009)

[67] C. Geppert et al., *Report on the ISOLDE Voltage Calibration Campaign 2009*, Private communication February 2011

[68] A. Lapierre et al., *Penning-trap mass measurements of the neutron-rich K and Ca isotopes: Resurgence of the $N = 28$ shell strength*, Phys. Rev. C85, 024317, (2012)

[69] Falke et al., *Transition frequencies of D lines of ^{39}K, ^{40}K, and ^{41}K measured with a femtosecond laser frequency comb*, Phys. Rev. A. 74, 032503, (2006)

[70] R. J. Barlow, *Statistics: A Guide to the Use of Statistical Methods in the Physical Sciences*, Wiley, (1989)

[71] C. von Platen et al., *Spin exchange polarization and hfs anomaly measurement of β-active ^{37}K* , Z. Phys., 244(1), 44-69, (1971)

[72] J.T. Eisinger, B. Bederson and B.T. Feld, *The Magnetic Moment of $40K$ and the Hyperfine Structure Anomaly of the Potassium Isotopes*, Phys. Rev., 86(1), 73-81, (1952)

[73] A. Beckmann, K.D. Boklen and D. Elke, *Precision Measurements of the Nuclear Magnetic Dipole Moments of ^{6}Li, ^{7}Li, ^{23}Na, ^{39}K and ^{41}K*, Z. Phys., 270(3), 173-186, (1974)

[74] Y.W. Chan, V.W. Cohen and H.B. Silsbee, *Hyperfine Structure and Nuclear Magnetic Moment of ^{41}K*, Phys. Rev., 184(4), (1969)

[75] N. Bendali et al., *Na^+-Na charge exchange processes studied by collinear laser spectroscopy*, J. Phys. B: At. Mol. Phys 19, 233-238, (1986)

[76] K. Kreim, *A quadrupole voigt lineshape*, Private communication, May 2012

[77] V.W. Cohen, *Error in reported measurements of nuclear magnetic-moments of ^{24}Na and ^{42}K*, Bull. Am. Phys. Soc. 18 (4), (1973)

[78] A. M Mårtensson-Pendrill et al., *Reanalysis of the isotope shift and nuclear charge radii in radioactive potassium isotopes*, J. Phys. B.: At. Mol. Opt. Phys. 23, 1749-1761, (1990)

[79] T. J. Mertzimekis et al., *Ground state magnetic dipole moment of ^{35}K*, Phys. Rev. C 73, 024318, (2006)

[80] N.J. Stone, *Table of nuclear magnetic dipole and electric quadrupole moments*, Atomic Data and Nuclear Data Tables 90, (2005)

[81] M.L. Bissell et al., *Spins, Moments and Charge Radii Beyond ^{48}Ca* Proposal to the INTC committee, CERN, (2011)

[82] Skobeltsyn Institute of Nuclear Physics, *Database of the Lomonosov Moscow State University*, `http://cdfe.sinp.msu.ru/services/radchart/radmain.html`

[83] M. Avoulea et al., *Nuclear charge radii and electromagnetic moments of radioactive scandium isotopes and isomers*, J. Phys. G: Nucl. Part. Phys. 38, 025104, (2011)

[84] I. Angeli et al., *N and Z dependence of nuclear charge radii*, J. Phys. G: Nucl. Part. Phys. 36, 085102, (2009)

[85] K. Blaum et al., *Nuclear moments and charge radii of argon isotopes between the neutron-shell closures $N = 20$ and $N = 28$*, Nuclear Physics A 799, 30-45, (2008)